

**Confinement induced assembly of anisotropic
particles: patchy colloids and water molecules**

**Opsluitingsgeïnduceerde assemblage van anisotrope
deeltjes: gefragmenteerde colloïden en
watermoleculen**

Sobrino Fernández Mario



Dissertation submitted to attain the degree of
doctor of Science at the University of Antwerp

Proefschrift voorgelegd tot het behalen van de graad van
doctor in de Wetenschappen aan de Universiteit Antwerpen

2016

Supervisors: Prof. Dr. *F. M. Peeters*

Dr. *V. R. Misko*

Dr. *M. Neek-Amal*

Abstract

In this thesis, we focus on questions concerning the effect of confinement on the ability of individual constituents to form large scale aggregates. The research is divided into two parts. In the first one, the structural and dynamical properties of patchy colloids interacting with an external confinement potential is explored. The second part is devoted to the formation of ice monolayers when water is confined between two graphene layers with a separation of a few angstrom. Each part is relatively independent of the other, and can be read separately.

Firstly, we will present basic knowledge about colloidal systems. These consist of mesoscopic particles that in many ways can be regarded as large atoms, although they can be studied using physics with less consideration of their chemical signatures at the microscopic level. Over the last few years, tremendous progress has been made in diversifying synthetic strategies for the preparation of these particles, and a wide range of different colloids are now available with tailorable size, shape and interaction potential. Attention is given to the properties and preparation techniques of a special class of colloids, Janus particles, that are characterized as having a different chemical composition on their two hemispheres.

Then, we present the computational methodology which will be relevant for the calculations done in this thesis. All calculations were performed using the molecular dynamics (MD) program LAMMPS, from Sandia National Laboratories. In MD, the motion of objects under the influence of classical forces is simulated, showing a dynamical evolution of the system.

For the patchy colloids, we use a two-dimensional model of Janus discs consisting of a hydrophobic and charged semicircle. When placed in a solution, the hydrophobic sides will attract towards one another while the charged sides will give rise to repulsive forces. Using the interplay of these

competing interactions, the morphology of these particles is studied when placed in a channel-like environment that is modelled by a one dimensional harmonic confinement potential. The interest in this system is first of all due to the fact that it could serve as a simple model for membrane formation. A variety of ordered membranes are found consisting of single and multiple chain configurations with different particle orientations which we will summarize in a phase diagram.

Next, the two dimensional model of Janus discs is generalised to three-dimensional Janus spheres. The interplay of the competing interactions between two hemispheres results in a self-assembly of helical superstructures whose helicity can be controlled by altering the pH concentration of the solution in which the spheres are placed. For example, the system can be prepared so that the colloids form modified Boerdijk-Coxeter (B-C) helices, an assembly of regular tetrahedra in a twisted fashion with the colloids placed on the vertices.

In the second part the thesis deals with the formation of ice monolayers between hydrophobic plates. When water is confined in hydrophobic pores, the hydrogen-bond network is forced to terminate at these surfaces. As a result, the entire hydrogen-bond network is frustrated, causing its properties to be altered. In a recent experiment, a high-resolution TEM microscopy image was reported of water locked between two graphene sheets. Their observation showed that such nanoconfined water forms a cubic ice crystal structure, a discovery that was later disputed by other experimentalists. Using the reactive bond order potential ReaxFF, a bond order dependent potential that provides an accurate description of chemical bonds and their reactions, the formation of ice crystals between graphene layers is explored. External parameters were chosen in order to replicate the experimental setup. We find that nonpolar flat layers of ice can nucleate between the graphene layers with a crystal structure having a unit cell consisting of a square-rhombic tiling. Subsequent square-ice layers are found to be shifted in-plane over a fraction of the lattice constant.

Lastly, we consider the effect of an external electric field on a monolayer of confined ice. We find that an electric field alters the in-plane order of the hydrogen bonds, resulting in a reorganisation of the crystal to a polarised state. Reversing the electric field does not restore the system to the non-polar initial state, instead a residual dipole moment remains in the system.

Abstract

In deze thesis richten we ons op vragen met betrekking tot de invloed van opsluitingspotentialen op het vermogen van afzonderlijke bestanddelen om zich samen te klonteren in grotere aggregaten. Het onderzoek van dit werk werd onderverdeeld in twee delen. In het eerste deel werden de structurele en dynamische eigenschappen van anisotrope colloïdale deeltjes bestudeerd onder invloed van een externe quasi-1-dimensionale opsluitingspotentiaal (Q1D). Het tweede deel van de thesis is gewijd aan de vorming van ijs monolagen wanneer water wordt opgesloten tussen twee lagen grafeen met een scheiding van een paar angström. De twee delen zijn afzonderlijk van elkaar en kunnen apart gelezen worden.

Allereerst wordt er een voordracht gemaakt over de basis concepten van colloïdale systemen. Deze bestaan uit mesoscopische deeltjes die op veel manieren kunnen worden beschouwd als grote atomen, hoewel ze kunnen bestudeerd worden door een natuurkunde met minder aandacht op hun specifieke moleculaire structuur. In de afgelopen jaren heeft men een enorme vooruitgang geboekt in de diversificatie van synthetische strategieën voor de bereiding van deze deeltjes, en een breed scala van verschillende colloïden zijn nu verkrijgbaar met een aanpasbare grootte, vorm, en interactie potentiaal. Extra aandacht wordt gegeven aan de eigenschappen en bereidingstechnieken van een speciale klasse van colloïden, Janus deeltjes, die worden gekenmerkt door de verschillende chemische samenstelling op hun twee hemisferen.

In het volgende deel worden de computationele methoden die relevant zijn voor de uitgevoerde berekeningen in dit proefschrift voorgesteld. Deze berekeningen werden uitgevoerd met behulp van het moleculaire dynamica (MD) programma LAMMPS, uitgegeven door Sandia National Laboratories.

Met behulp van MD wordt de beweging van voorwerpen onder invloed van klassieke krachten gesimuleerd en kan er zo een dynamische evolutie van het systeem worden weergegeven.

Voor de anisotrope colloïdale deeltjes gebruiken we een tweedimensionaal model van Janus schijven bestaande uit een hydrofobe en een geladen halve cirkel. Wanneer deze geplaatst worden in een oplossing, zullen de hydrofobe zijdes aangetrokken worden aan elkaar, terwijl de geladen zijanten zich van elkaar afstoten. De morfologie van deze deeltjes wordt onderzocht in een kanaal-achtige omgeving, gemodelleerd door een harmonische opsluitingspotentialiaal. De belangstelling voor dit systeem is voornamelijk door het feit dat het zich kan dienen als een eenvoudig model voor membraanvorming. Een verscheidenheid aan gestructureerde membraan configuraties kan worden gevonden, bestaande uit enkele en meervoudige ketens, die worden samengevat in een fase diagram.

Verder wordt het tweedimensionaal model van Janus schijven veralgemeend naar driedimensionale Janus sferen. Het samenspel van concurrerende interacties tussen de sferen resulteert in de zelfassemblage tot schroeflijnvormige superstructuren waarvan de helicititeit geregeld kan worden door het veranderen van de pH concentratie van de oplossing. Zo kan het systeem worden bereid zodat de colloïden zich vormen naar een Boerdijk-Coxeter (B-C) helix.

Het tweede deel van het proefschrift behandelt de vorming van ijs monolagen tussen twee hydrofobe platen. Wanneer water wordt opgesloten in hydrofobe poriën, worden de waterstofbruggen gedwongen om te eindigen bij deze oppervlakken. Hierdoor wordt het gehele waterstofbindingsnetwerk gefrustreerd en kunnen de eigenschappen van de volledige structuur wijzigen. In een recent experiment werd gemeld dat water tussen twee grafeen lagen zich vormt tot een kubische kristalstructuur, een ontdekking die later werd betwist door andere experimentatoren. Met behulp van een reactieve bond order potentialiaal (ReaxFF) wordt de vorming van ijs tussen grafeenlagen onderzocht. Externe parameters werden gekozen om de experimentele opstelling te repliceren. We vinden dat een niet-polair vlak van ijs zich kan vormen tussen de grafeenlagen met eenheidscel bestaande uit een opeenvolging van vierkante en ruitvormige tegels. Opeenvolgende lagen blijken zich te verschuiven in het vlak over een fractie van de roosterconstante.

Tenslotte beschouwen we de invloed van een extern elektrisch veld op een monolaag ijs. We vinden dat een elektrisch veld de opeenvolging van de waterstofbruggen wijzigt waardoor er een reorganisatie van het kristal plaatsvindt naar een gepolariseerde toestand. Na het omkeren van het elektrisch veld kan het systeem zich niet meer herstellen naar de oorspronkelijke niet-polare toestand en blijft er zich een residueel dipoolmoment bevinden in het systeem.

Contents

List of figures	xiii
List of tables	xix
Nomenclature	xxi
I Introduction	1
1 General introduction	3
1 Competing interactions	5
1.1 Self-assembly	5
1.2 Janus particles	5
1.3 Preparation techniques	8
1.3.1 Self-assembly of block copolymers	8
1.3.2 Masking	8
1.3.3 Phase separation	10
1.4 Properties of Janus particles	11
2 Graphene and graphene-like materials	13
3 Organization of the thesis	15
2 Molecular dynamic simulations	17

1	Schematic overview of MD simulations	19
2	Integration schemes	21
3	Velocity Verlet algorithm	23
3.1	Symplecticity of the velocity Verlet algorithm	23
3.1.1	Hamilton's equations	23
3.1.2	Symplecticity of numerical integrators	25
3.2	Shadow theorem	27
4	Colloidal interaction potentials	31
4.1	Hard-sphere potential	31
4.2	Hydrophobic attraction	31
4.3	Derjaguin-Landau-Verwey-Overbeek (DLVO) potential	32
4.4	Light as an external potential for colloidal particles	35
4.4.1	Scattering force	35
4.4.2	Gradient force	35
4.5	Creation of quasi-1D periodic potentials	36
5	Molecular mechanics and reactive force fields	40
6	LAMMPS	43
6.1	Neighbour lists	44
6.2	Periodic Boundary Conditions	45
6.3	Thermostatting	45
6.4	Barostatting	47
6.5	Nosé-Hoover	48

II Self-assembly of Janus particles 49

3	Self-assembly of Janus particles confined in a channel	51
1	Introduction	53
2	Janus particle dynamics	55
3	Simulation technique and parametrization	58
4	Numerical results	61
4.1	Correlation functions	63
4.2	Phase diagram	65
5	Discussion and conclusions	67

4	Self-assembly of Janus particles into helices with tunable pitch	69
1	Introduction	71
2	Model and simulation technique	74
3	Numerical results	76
3.1	Morphologies	76
3.2	Tunable pitch	78
3.3	Boerdijk-Coxeter helix	78
4	Discussion and conclusions	82
III	Flat ice between graphene layers	85
5	AA-stacked bilayer square ice between graphene layers?	87
1	Introduction	89
1.1	Structure of ice	89
1.1.1	Small isolated clusters	91
1.1.2	Water clusters on a graphite sheet	93
1.2	Water under extreme confinement	96
1.2.1	Water inside carbon nanotubes	96
1.2.2	Water confined in slit nanopores	98
2	Square ice in graphene nanocapillaries?	99
3	Methodology	101
4	Confined ice	103
4.1	Monolayer of ice	103
4.2	Bilayer square ice	106
4.3	Trilayer ice	109
5	Discussion and conclusions	110
6	Electric field induced structural changes of water confined between two graphene layers	113
1	Introduction	115
2	Method and model	117
3	Results	118
3.1	Square-rhombic lattice for 2D-ice confined between two hydrophobic layers when $E=0$	118

3.2	Rhombic-rhombic lattice for confined 2D-ice when $E \neq 0$	120
3.3	Electric hysteresis of confined 2D-ice	120
3.4	Energetic considerations	122
4	Discussion and conclusions	124

IV Appendices 125

Appendix A Formal deviation of the Velocity Verlet algorithm 127

1	Discretisation of the Liouville operator	127
2	Shadow Hamiltonian	132
3	Lie product formula	133

References 135

Concluding remarks and outlook 155

Curriculum Vitae 158

List of figures

1.1	Representative examples of recently synthesized anisotropic colloids classified in rows by anisotropy type and in size from left to right.	6
1.2	Fluorescence image of a colloidal Kagome lattice.	7
1.3	Different types of Janus particles.	8
1.4	Schematic diagram illustrating the three main strategies for preparing Janus nanoparticles	9
1.5	Masking techniques as they are being used in synthesising Janus particles.	10
1.6	Biphasic electrified jetting using side-by-side dual capillaries. (lhs) Schematic diagram of the experimental setup, (rhs) fluorescence microscopy image of the biphasic Janus particle.	11
1.7	Electric actuation of bicoloured Janus particles.	12
1.8	Carbon nanostructures exhibiting different dimensionalities.	14
1.9	Structure models of 2D, 1D, and 0D boron nitride nanostructures similar to those of carbon	15
2.1	Schematic of a molecular dynamics algorithm.	19
2.2	Divergence of trajectories in MD.	22
2.3	Phase space of the shadow Hamiltonian $\tilde{\mathcal{H}}$ corresponding to a harmonic oscillator for the velocity Verlet scheme.	28
2.4	Numeric solutions of the harmonic oscillator Hamiltonian using the Velocity Verlet scheme.	29

2.5	Ratio of the numerically calculated energy to the Hamiltonian of the classical system for a harmonic oscillator.	30
2.6	Typical schematic of the hydrophobic attraction present between non-polar surfaces.	32
2.7	Schematic illustration of the electrical double-layer formed around a negatively charged colloid.	34
2.8	(lhs) A spherical crystal formed by self-assembled colloidal beads on a liquid droplet with a diameter of 60 μm . (rhs) An optical wall is created using laser tweezers confining a small number of particles to build an isolated system.	37
2.9	Optical-tweezer assembly of a 3D colloid crystal.	38
2.10	Schematic of an experimental arrangement used to generate a quasi-1D periodic potential.	39
2.11	Quasi-1D periodic potential created by two interfering laser beams (lhs) and experimentally measured fringe pattern (rhs).	39
2.12	Schematic representation of four key contributions to a molecular mechanics force field: bond stretching, angle bending, torsion, and non-bonded interactions.	40
2.13	Torsional potential for the example of a single bond between two sp^3 carbon atoms and a double bond between two sp^2 carbon atoms.	41
2.14	Example of the bond order dependence on the interaction distance for different covalent bonds.	43
2.15	Illustration of the different approaches to constructing neighbour lists: all pairs, cell subdivisions and neighbour lists.	44
2.16	Implementation of periodic boundary conditions in 2D.	46
3.1	(A) Upper panel: position of colloidal particles at an oil–water interface for different contact angles Lower panel: corresponding positioning of particles at a curved interface. (B) Emulsion stabilization by colloidal particles. (C) Stabilization or sedimentation of emulsions affected by a change in pH value or salt concentration. (D) Low (a) and high magnification (b and c) scanning electron microscopy (SEM) images of a cluster of colloids.	54
3.2	Example of a rigid Janus dendrimer with carboxylic acids on one side and tert-butyl groups on the other side.	56
3.3	Configuration of two Janus discs.	57
3.4	Janus potential indicated by red saturation for the repulsive DLVO potential, and blue colouration for the attractive hydrophobic effect.	58

3.5	Region of permitted tilt angles between two charged hemispheres plotted as a function of the logarithmic concentration of monovalent salt.	59
3.6	Different configurations of adjoining Janus particles in a solution using the parametrisation outlined in Sec. 3.	61
3.7	Different particle morphologies of Janus particles in a quasi-one-dimensional parabolic confinement potential found with molecular dynamics simulations, depending on the packing fraction η and the strength of the transverse trap potential $K\sigma$	62
3.8	Correlation functions g_{000} and g_{110} for characteristic morphologies at $T = 10^{-1}, 10^0, 10^1, 10^2, 10^3$, and 10^4	64
3.9	Progression of local pair correlation parameters Γ_{000} and Γ_{110} for reference structures and intermediate states.	66
3.10	Phase diagram of the different structures formed by Janus discs in a harmonic trap for various values of the packing fraction and confinement strength.	68
4.1	TEM images of nanobelts assembled from a peptide amphiphile composed of a polar negatively charged peptide and a hydrophilic valine face.	71
4.2	Schematic illustrations of actions of a PA leading toward bacterial membrane permeation and disruption.	72
4.3	Scanning electron microscopy (SEM) images of the disruption of the cell membrane of <i>E. coli</i> (a-b) and <i>S. aureus</i> (c-d).	73
4.4	PA assembly when used as a carrier for therapeutic cell delivery.	74
4.5	(A) By increasing the salt concentration of the solution, larger particle clusters are formed. (B) Fluorescence images illustrating the comparison between a small chiral cluster at low salt concentration and a longer helical cluster. (C) Fluorescence image illustrating the stability of worm-like structures at high volume fraction	74
4.6	Network of reaction pathways at low salt concentration, all of which were experimentally observed.	76
4.7	Basal area of different elongated superstructures at increasing packing fraction.	77
4.8	Different helical structures while varying the electrostatic interaction range.	79
4.9	(a) Helical superstructure consisting of two intertwined spirals and (b) corresponding straight complex.	79
4.10	Helical superstructure consisting of: (a) four intertwined spirals and (b) corresponding straight complex.	80
4.11	Top view of a Boerdijk-Coxeter Helix.	80

4.12	Free energy per particle as a function of half the opening angle of the hydrophobic patch.	81
4.13	Illustration of a BC helix found in simulations alongside a reconstruction of the underlying tetrahelix structure.	81
4.14	BC helices as characterized by the sequence given by Eq. (4.2).	82
5.1	Phase diagram of water as a log-lin chart with pressure from 1 Pa to 1 TPa and temperature from 0 K to 650 K.	89
5.2	Ice I_h structure consisting of the formation four hydrogen bonds for each water molecule in the crystal.	90
5.3	Six possible orientations of an H_2O molecule at a given site in the lattice.	91
5.4	Visualisation of the experimentally-identified structures of a water dimer (top), trimer (middle) and tetramer (bottom).	92
5.5	Schematic illustration of an adsorbed hydrogen atom near a conductor interacting with its image charges.	93
5.6	H_2O -graphene interaction energy as a function of substrate-adsorbate distance as obtained with different computational methods.	94
5.7	Optimized geometry of a monomer adsorbed on a graphite sheet.	94
5.8	Pathway for diffusion of a water monomer on the graphite surface.	95
5.9	Optimized geometries of water clusters $(H_2O)_n$ adsorbed on a graphite sheet.	96
5.10	Relaxed structures of ice inside carbon nanotubes.	97
5.11	(a) Transverse distribution of the density of oxygen atoms for different plate separations H . Lateral and transverse views of (b) a water mono-layer, (c) ice mono-layer and (d) a water bilayer.	98
5.12	(lhs) Low magnification TEM image of a reference sample in which water was trapped in large bubbles with a diameter of ~ 100 nm. (rhs) Part of the water pocket at higher magnification.	99
5.13	(a) Isolated crystallite with a varying number of layers. (b-c) Simulated TEM images for monolayer, bilayer, and trilayer ice with AA and AB stacking, respectively.	100
5.14	Typical temperature evolution of water during the annealing phase.	102
5.15	Side (a) and top (b) view of the relaxed monolayer of ice between two graphene layers.	104
5.16	The (a) radial distribution function for O-O distances and (c) the local dipoles of the individual water molecules.	105

5.17	(lhs) A polar lattice of monolayer ice confined between two graphene layers which is about 10 meV/atom higher energy than the non-polar structure. (rhs) The corresponding local dipoles.	106
5.18	Side (lhs) and top (rhs) view of a relaxed ice monolayer between two h-BN layers. . .	107
5.19	Relaxed bilayer ice between two graphene layers are shown in (a) side and (c) top view. In (b) the corresponding radial distribution function for O-O distances is shown.	108
5.20	Multi-layer ice confined between graphene layers.	110
6.1	In-plane diffusion coefficient of water at 300 K as a function of the external electric field (E) at two inter-plate distances.	116
6.2	Side (a) and top (b) view of a relaxed square-rhombic monolayer of ice between two graphene layers, and the flat rhombic-rhombic monolayer (c) when an external electric field is applied.	117
6.3	Hysteresis curve of the net polarisation of water confined between two graphene layers separated by $h=6.5\text{\AA}$	118
6.4	Local dipoles in a monolayer of water confined between two graphene layers for (a) a non-polarised state, and (b) at the saturation polarisation.	119
6.5	Hysteresis loop of the polarization of an ice monolayer confined between two graphene sheets for different frequencies of the applied electric field.	121
6.6	Potential (a) and van der Waals (b) energy as function of applied electric field for different frequencies of the electric field.	123

List of tables

1.1	Classification of the colloidal domain as a function of the phase of the colloidal particles and the dispersed medium. Both substances can be in a gas, liquid, or solid-like state.	4
3.1	Parameters for the pair potentials that were defined in Eqs. (3.3-3.4).	61
5.1	Parameters for the LJ potential between the h-BN layers and oxygen atoms.	106
5.2	Different energy contributions (per atom, and for each hydrogen bond) and lattice parameters of the minimized energy configurations for mono (g.ice.g and g.ice.g (polar)), bilayer (g.ice.ice.g) and trilayer (g.ice.ice.ice.g) water confined between two graphene layers.	109
6.1	Characteristic hysteresis parameters for different frequencies: Coercive field (E_c), remnant polarization (P_r), and saturation polarization (P_s).	122

Nomenclature

Acronyms / Abbreviations

1D One-Dimensional

2D Two-Dimensional

3D Three-Dimensional

AFM Atomic-force microscopy

CNT Carbon nanotube

DFT Density functional theory

DLVO Derjaguin-Landau-Verwey-Overbeek

h-BN Hexagonal boron nitride

JP Janus particle

LAMMPS Large-scale Atomic/Molecular Massively Parallel Simulator

LHS Left-hand side

LJ Lennard-Jones

MD Molecular dynamics

MOON Modulated optical nano-particle

PA Peptide amphiphile

PS polystyrene

Q1D Quasi-One-Dimensional

ReaxFF Reactive Force Field

RHS Right-hand side

SPP Self-propelled particle

TEM Transmission electron microscopy

vdW van der Waals

Part I

Introduction

CHAPTER 1

General introduction

For decades, colloidal particles have been important research objects belonging to the domain of soft matter [1]. Soft matter physics is regarded as a subfield of condensed matter physics comprising of a broad class of materials of which the predominant physical behaviour occurs at an energy scale which is comparable with room temperature thermal energy. Examples of these systems include, but are not limited to, colloids, polymers, complex fluids, liquid crystals and granular materials. Their behaviour arises in ways that generally cannot be predicted directly from their atomic molecular constituents, which is in stark contrast to materials belonging in hard condensed matter physics. Accordingly, systems belonging to this field are studied using physics with less consideration of their chemical signatures at the microscopic level.

A colloid suspension is defined as a mixture of insoluble particles that are suspended in a continuous medium. The separate dispersed substance is what is called a colloid. The minimum size of a colloidal particle is set by the requirement that its interaction with the solvent is taken into account in an averaged way, i.e. that many solvent molecules are supposed to interact simultaneously with the surface of a single colloidal particle. Its Brownian motion is then characterized through macroscopic quantities related to the fluid (such as its viscosity and temperature). Additionally, its maximum size is set by the requirement that the colloidal particle behaves as a large molecule, showing vivid thermal motion. Thermal motion is only relevant when the displacements are a sizeable fraction of the dimension of the particle during typical experimental time-scales. Similar to molecules, colloidal particles can undergo electrostatic, van der Waals, steric repulsive, and dipolar interaction

4 | General introduction

forces. Unlike their molecular counterparts, most colloids are large enough so that their positions and motions can be measured precisely using optical methods: they are found with a diameter in the range of several nanometers to a few micrometers. As such, these particles are easily visible in an optical microscope, although at smaller size ranges ($r < 250$ nm) an ultramicroscope or electron microscope may be required. A classification scheme can be thought out depending on the phase of the colloid and the dispersed medium, which is given in Table 1.1. Both substances can be gas, liquid, or solid-like. The present thesis will mainly focus on the study of colloidal suspensions, i.e. solid particles in a liquid.

Medium	Dispersed phase		
	Gas	Liquid	Solid
Gas		Liquid aerosol <i>fog, spray</i>	Solid aerosol <i>smoke, ice cloud</i>
Liquid	Foam <i>cream</i>	Emulsion <i>pickering emulsion</i>	Sol <i>blood, ink</i>
solid	Solid Foam <i>aerogel</i>	Suspension <i>hydrogel</i>	Solid sol <i>cranberry glass</i>

Table 1.1 Classification of the colloidal domain as a function of the phase of the colloidal particles and the dispersed medium. Both substances can be in a gas, liquid, or solid-like state.

Inorganic colloidal particles of sizes < 10 nm can manifest quantized energy structures. Colloids that exhibit such quantization are often called Q-particles. In these particles, there are approximately as many molecules on the surface as in their interior, making the nature of the surface largely responsible for its electronic properties [2]. Semiconductor nanoparticles are often referred to as quantum dots (QDs) or artificial atoms which can be placed in ordered arrays, representing a new class of materials [3], often referred to as artificial solids. An extended array of colloidal particles of sizes > 100 nm can strongly diffract light, with wavelengths compared to particle sizes, forming photonic band gaps. This array freezes light within itself if the light is generated inside the array, and inhibits the propagation of light through the structure at certain frequencies [4].

1 Competing interactions

Colloids can be regarded as large atoms with tailorable size, shape, and interaction potentials. Anisotropic particles are a class of colloids that have attracted significant attention in recent years due to their novel morphologies and diverse potential applications. Because of their shape and/or chemical composition these colloidal particles possess energetic interactions that not only depend on their separation but also on their orientation. Anisotropy can be implemented in different ways. In Fig. 1.1 a compilation is made of different types of anisotropic particles that can be designed at varying length scales. In general, they can be divided into three categories according to their imbalance in chemical composition, surface chemistry, or particle morphology. Each is a possible building block that can be incorporated into superlattice assemblies and hierarchical structures. The addition of shape and interaction anisotropy enhances the complexity of possible assemblies to motifs potentially as complex as those seen in a molecular crystal.

1.1 Self-assembly

Self-assembly is the biological "bottom-up" manufacturing technique to design the spatial and temporal arrangement of molecules at different levels of hierarchy [8]. In this process, a disordered system of components form an organized pattern as a consequence of local interactions among the components themselves, with little or no external direction. The ability to program the individual constituents of large scale clusters, so that they can reconfigure and restructure on demand, is one of the ultimate goals of this technique. For example, in [19] a realization of a self-assembled Kagome lattice is given using colloids with two attractive hydrophobic poles and a charged patch along the equator (schematically shown in Fig. 1.2(a)). The Kagome lattice was chosen as a target colloidal crystal, for which the triblock spheres were specifically designed. After being placed in a solution, and over-night sedimentation, ordering is switched on at will by adding salt to the solution, which screens the electrostatic repulsion between colloids and allows for short-range hydrophobic attractions to come into play. The successful completing of the ordering process into a periodic lattice requires the energy landscape of the system to be smooth enough to allow for kinetically favoured intermediates to transform to the most thermodynamically favoured product where the contact between the hydrophobic poles is maximized.

1.2 Janus particles

P. G. de Gennes raised the concept of Janus particles (JPs) in his Nobel Prize address entitled Soft Matter in 1991 [20]. He borrowed the name *Janus* from the Roman god of beginning and endings,

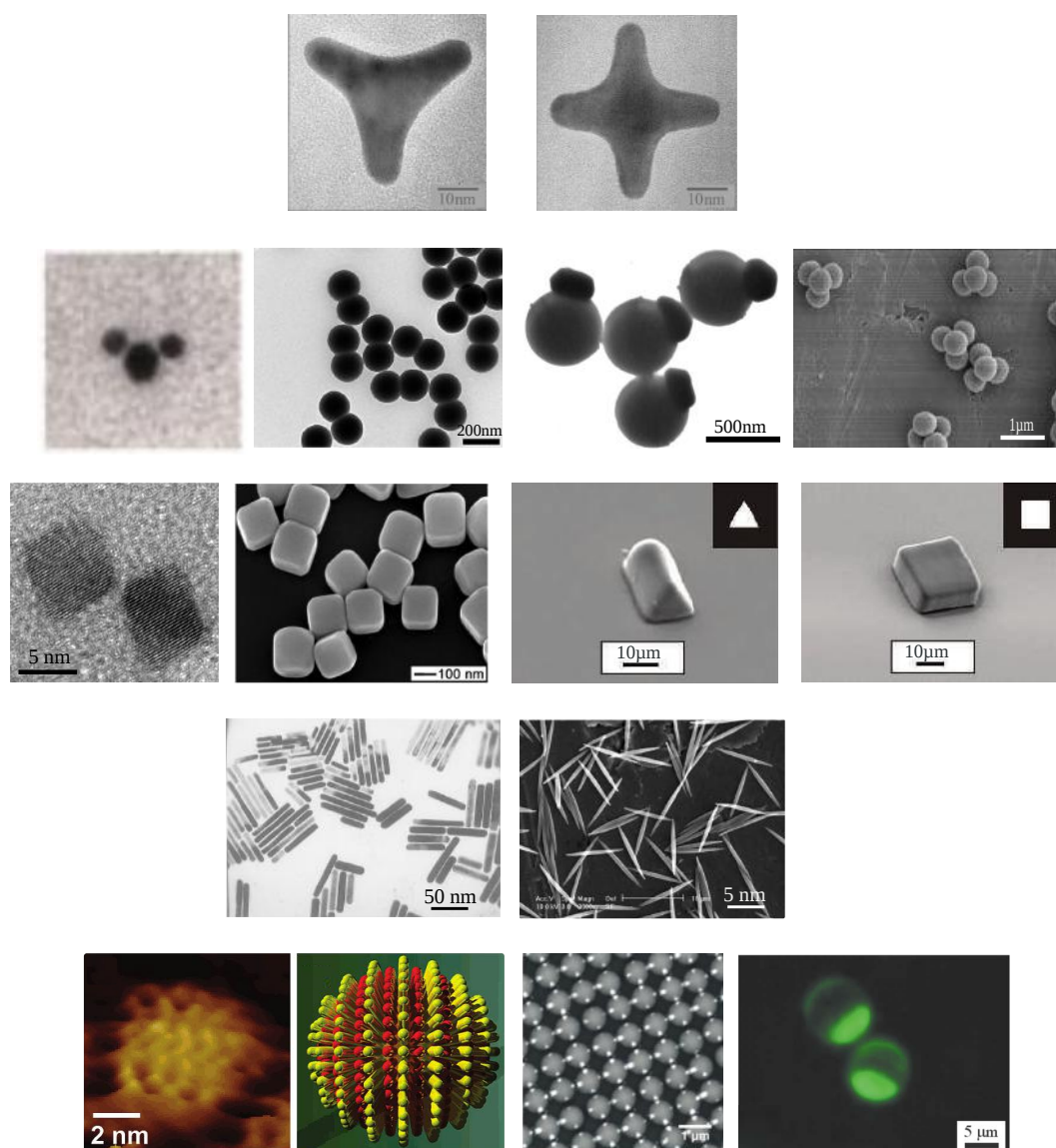


Figure 1.1 Representative examples of recently synthesized anisotropic colloids classified in rows by anisotropy type and in size from left to right. From left to right, top to bottom: branched particles such as a regular gold tripod and tetrapod [5]. Second row: DNA-link gold nanocrystal [6] (the small (large) nanocrystals are 5 nm (10 nm)), silica dumb-bells [7], asymmetric dimers [8] and fused clusters [9] form colloidal molecules. Examples of faceted polyhedra such as PbSe [10] and silver [11] cubes as well as triangular polymer prisms [12] are shown in the third row. Below, rods and ellipsoids of different chemical composition (gold [13] and polymer latex [14]) are shown. The final row depicts examples of patterned particles including striped spheres [15], patchy spheres [16], and Janus spheres [17].

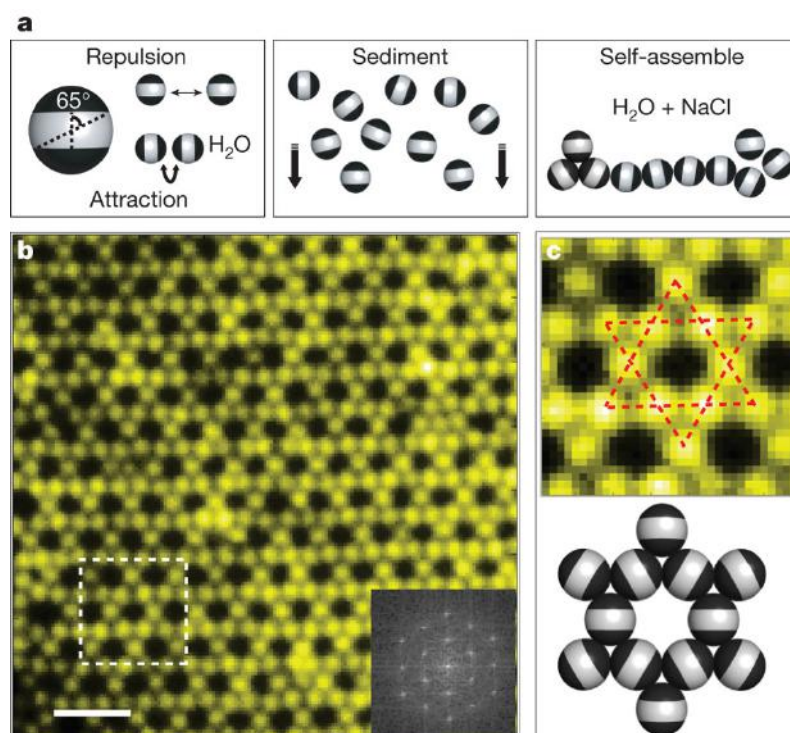


Figure 1.2 (a) Triblock spheres with hydrophobic poles (indicated in black) with an opening angle of 65° and charged along the equator (white), are sedimented in deionized water. Then NaCl is added in order to screen the electrostatic repulsion between neighbouring spheres, allowing for the self-assembly of a Kagome lattice by short-range hydrophobic attraction. In (b) a fluorescence image of a colloidal Kagome lattice and its fast Fourier transform image is shown. The scale bar is $4\ \mu\text{m}$. The top panel in (c) shows an enlarged view of the dashed white rectangle in (b) whereas the bottom panel shows a schematic illustration of particle orientations (adapted from Ref. [19]).

who is usually depicted as having two faces, to describe a special class of colloidal particles with different chemical compositions on each hemisphere. His ideas were mostly neglected in subsequent years, where most of the research on colloids focused on homogeneous particles [21]. In recent years however, the development of chemical synthetic methods in combination with advancements in computational power and imaging techniques has enabled this field to grow substantially. Figure 1.3 summarizes particle architectures that have been attained so far. Different types of compartmentalisation can be created, one that occurs throughout the full particle (core-compartmentalized), just on the surface (surface-compartmentalized) using different surface modifiers, or a combination of these two.

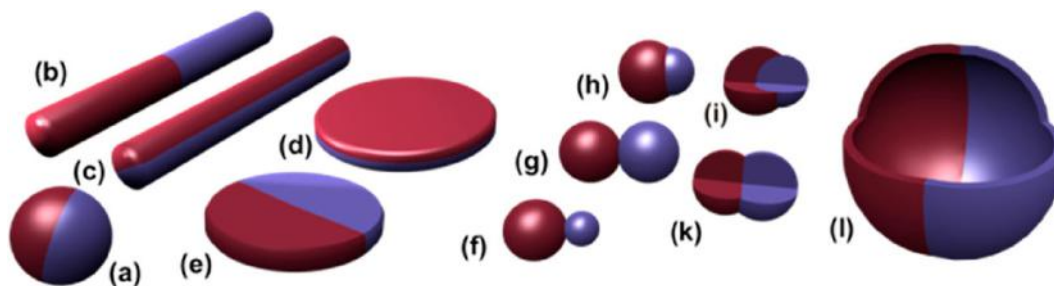


Figure 1.3 Different types of Janus particles: (a) spherical, (b-c) two types of cylindrical, and (d-e) disc-shaped JPs. (f-k) depicts various kinds of dumb-bell shaped JPs and lastly a Janus capsule is shown in (l) (adapted from Ref. [22]).

1.3 Preparation techniques

Tremendous progress has been made in diverse synthetic strategies for the preparation of Janus particles. The aim of these strategies is to include diverse functionalities of the hemispheres, at best with a high particle yield while attaining monodispersity. Precision engineering on the smaller side of the length scale (< 100 nm) has proven to be the most challenging. This is not only due to the increasingly complicated and limited strategies in obtaining these structures, but also because experimental proof of actually obtaining well-defined Janus particles is more difficult to deliver.

When designing mesoscopic Janus particles, a multitude of experimental techniques are available. They can roughly be divided into three main categories, visualised in Fig. 1.4, depending on the route followed in their preparation.

1.3.1 Self-assembly of block copolymers

The first group comprises Janus particles that are obtained via the self-assembly of block copolymers, which historically is the first technique that was used to prepare Janus nanoparticles. The self-assembly of block copolymers is a flexible strategy, in the sense that it can be applied to many different polymer types. It benefits from the use of living free-radical polymerization methods, which permits the preparation of block copolymers with a well defined structure and composition [23].

1.3.2 Masking

A large number of recipes make use of different versions of the masking technique, which is the most intuitive route to site-specific functionalised Janus particles. The asymmetric fictionalization is achieved by exposing only one hemisphere of a colloid to an environment where a reaction is carried out, while the remaining part of the surface is temporarily masked. In Fig. 1.5 a schematic represen-

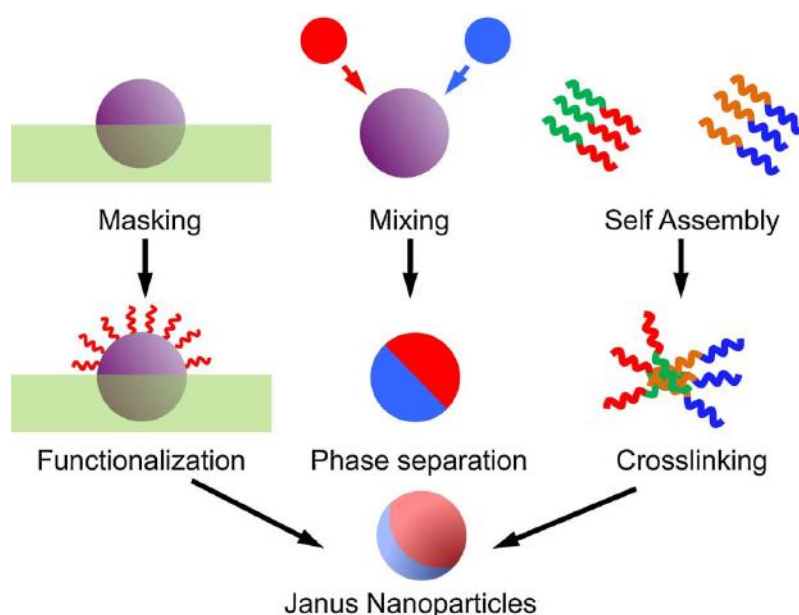


Figure 1.4 Schematic diagram illustrating the three main strategies for preparing Janus nanoparticles: masking, phase separation, and self-assembly (adapted from Ref. [24]).

tation is made of four strategies that allow to top-selectively modify the surface of colloids using masking techniques. This masking is usually achieved by either depositing them on a solid surface (Fig. 1.5(a-b-c)), or by trapping the colloids in an interface between two fluid phases (Fig. 1.5(d)). The advantage of these techniques is that it is applicable to virtually any type of material, while offering the possibility to modify the surfaces with a variety of functional groups.

The oldest masking technique consisted of partially masking precursor particles with a film (Fig. 1.5(a)). Amphiphilic glass microspheres of 40-50 μm were first obtained by depositing precursor beads on a solid substrate covered by a cellulose varnish film [25] which partially protected the particles. The unprotected hemispheres were treated with octadecyltrichlorosilane making them partially hydrophobic. In order to avoid the tedious masking and unmasking steps, the surface modification of a single hemisphere can be achieved in reactive directional fluxes. Here, the second hemisphere is supposed to be left untreated because it is sheltered by the particle itself (see Fig. 1.5(b)). The third method to topselectively alter the surface of particles is derived from microcontact printing technique, which is illustrated in Fig. 1.5(c). The preparation technique usually involves depositing a film on a elastomer stamp, after which the stamp is pressed against the surface the colloids. It is assumed that only the surface of the contact area of the particles with the stamp will be modified. The last masking route consists of arranging precursor particles along the interface between two media

(Fig. 1.5(d)). Reacting molecules are dissolved in the first medium, whereas the second medium remains inert.

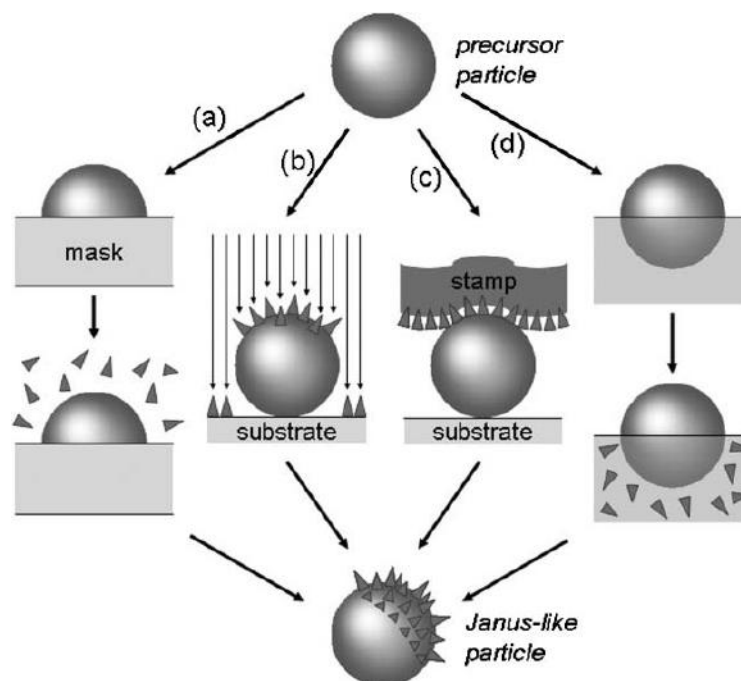


Figure 1.5 Masking techniques as used in synthesising Janus particles. (a) masking/unmasking of a colloid absorbed on a surface, (b) reactive directional fluxes or fields, (c) microcontact printing and (d) techniques based on liquid interfaces and partial contact with a reactive medium (adapted from Ref. [26]).

1.3.3 Phase separation

The masking techniques we described above allow for the preparation of well-defined Janus particles with respect to their morphology and surface functionalities. The main drawback of these strategies is that only a low amount of particles can be produced in each batch. The third category of preparation techniques can be used to rapidly produce large batches of anisotropic nanoparticles. Its downside is that there is a large variation in particle size and in the surface area of the two functionalised patches. The technique relies on the phase separation of two or more incompatible components in a mixture. For example, Roh et al. [27] showed how biphasic Janus particles can be prepared through electrodynamic jetting of two liquid solutions of immiscible polymers. A schematic diagram of the experimental setup is given at the lhs of Fig. 1.6. Two syringes are loaded with a specific jetting solution (indicated in red/green) and are connected to a dual-channel syringe tip with an inner

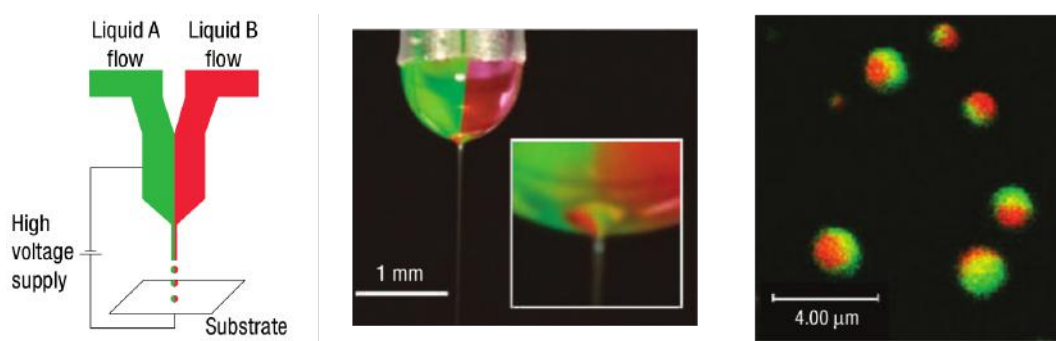


Figure 1.6 Biphasic electrified jetting using side-by-side dual capillaries (lhs) Schematic diagram of the experimental setup; the liquid experiences an electrical field that is formed between the tip of the liquid and the counter-electrode (collecting substrate). The centre figure depicts the experimental setup where in the inset a detailed image of the ejection point is shown. On the rhs, a fluorescence microscopy image of the biphasic JPs is given (adapted from Ref. [27]).

diameter of 0.26 mm. The tip of the needle can be seen in the top of the centre figure of Fig. 1.6. When exposed to an electric potential between the needle tip and the collection substrate, the shape of the drop at the edge of the needle starts to deform from the shape caused by surface tension alone.

Once the electric potential exerts a similar amount of force on the droplet as the surface tension does (which is reported to be in the 5 – 15 kV range), a cone shape starts to form near the bottom edge of the droplet (shown in Fig. 1.6) which ejects a jet of liquid. The jet contains microdroplets with a smaller diameter than this of the original droplet, and are collected at the anode. On the rhs of Fig. 1.6 a fluorescence microscopy image of the produced JPs is shown. The majority of the particles have a diameter 0.1 – 0.5 μm with outliers up to 3 μm .

1.4 Properties of Janus particles

Janus colloids possess unique characteristics related to their anisotropic structure, which can be manifested as amphiphilic, optical, magnetic, or as catalytic properties. Amphiphilic Janus particles are composed of a hydrophilic (polar) and a lipophilic (apolar) surface, making them the colloidal equivalent of a detergent. When placed in a solvent, these particles can self-assemble into membranes, mimicking the organisation of amphiphilic phospholipids into cell membranes. The relation between colloidal amphiphiles and their molecular counterparts will be further explored in Chapter 3.

The use of inorganic Janus particles which possess optical or magnetic properties is applicable in various potential applications, particularly in the biomedical domain. Modulated optical nanoparticles (MOONs) are fluorescent JPs that resemble the Moon: one hemisphere emits a bright fluorescent

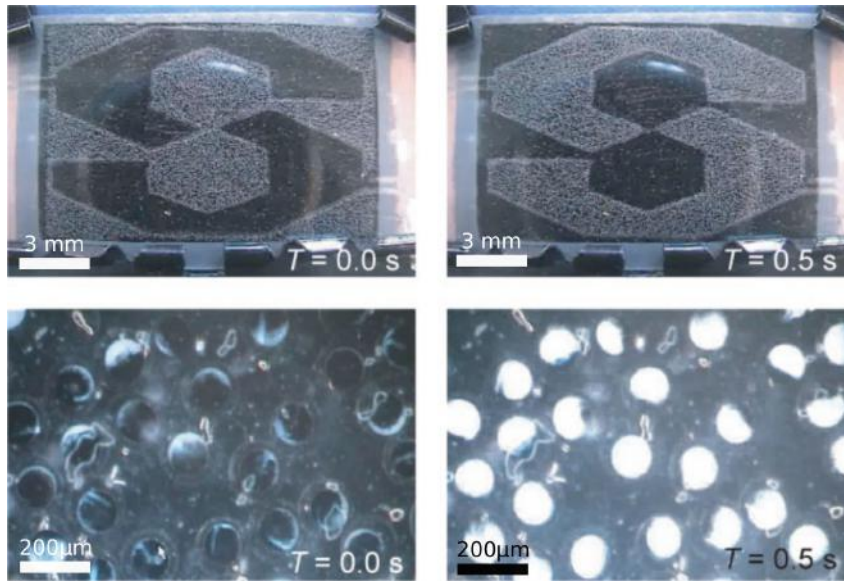


Figure 1.7 Electric actuation of bicoloured Janus particles. In the top row, a colour switch test was performed using a voltage of 100 V between the 0.4 mm gap between the two electrode panels at a switching frequency of 1 Hz. The dimensions of the display panel are 40 mm×40 mm. In the bottom row, a magnified view is given of the constituent JPs using an optical microscope (adapted from Ref. [30]).

signal, while an opaque metal darkens the other hemisphere. The Brownian motion of these particles causes them to tumble and blink erratically as they rotate literally through the phases of the moon [28]. Because of the size dependent Brownian motion, the signature frequency of the fluorescent fluctuations provides an unique mechanism for their identification. They can be used as tracer particles for microrheological measurements of size and time scales that are difficult to study with other methods. Indicator dyes can be added to the tracer particles, that react to local chemical concentrations. To give an example, in [29] MOONs with one side of the surface containing specific ligands (anti-HER-2-antibodies) were used to detect the targeting of these antibodies to cancer cells.

Furthermore, the use of Janus particles with asymmetric optical and magnetic properties allows for the remote control of the movement of these particles under the effect of an external field. In Fig. 1.7 an example is given of an electronic display composed of bicoloured Janus particles that can be used to fabricate high resolution displays, e.g. having more than > 300 pixels per centimetre (PPCM) [30]. Janus spheres of $20 - 30 \mu m$ were coated with inorganic pigments (carbon black and titanium oxide) dispersed in two hemispheres, giving the surfaces of these engineered spheres an

asymmetric charge distribution. In the presence of an external electric field, these spheres turn to orient their black hemisphere to the negatively charged terminal and vice versa.

The anisotropy of Janus particles can also be exploited to create self-propelled particles (SPP) in a chemical solution. SSPs are defined as autonomous agents that convert energy from the environment into directed or persistent motion. An interesting biological example of self-propelled particles are motor proteins such as Kinesin. Kinesins can move along microtubule filaments in the cytoplasm while carrying cellular cargo. They "walk" along the microtubules, by the hydrolysis of ATP at each step, powering the motion of their next step. The fabrication of synthetic self-propelled particles has been a challenge, especially in controlling the motion of these motors. Various strategies have been proposed to fabricate them [31], owing to an increased interest in the application of autonomous motors in medicine delivery, fluid mixing, or for on-chip particle transport. With the use of field gradients such as concentration, temperature, or electric field, colloids can be transported using interfacial forces [32]. The field gradient couples with the surface properties of the particle, which results in a net self-propulsion. A particle can be driven by an asymmetric distribution of reaction products on its surface, a process which is called self-diffusiophoresis. The autonomous motion of Janus particles was studied in [33]. Polystyrene microspheres with a diameter of $1.2\ \mu\text{m}$ were half-coated with a thin layer of platinum on one side of the spheres. When placed in a hydrogen peroxide solution, the platinum acts as a catalyst in the reduction of the "fuel" of hydrogen peroxide to oxygen and water. This induces non-equilibrium distributions and local gradients of gaseous products, which is responsible for the propulsion of the particles. The propulsion can be accelerated by increasing the hydrogen peroxide concentration of the solution. An enhancement of the velocity over the purely Brownian value was measured by a factor of nearly 30.

2 Graphene and graphene-like materials

The goal of this thesis is to study the effects of confinement on two types of matter, the first one being the colloidal Janus particles which were described above, and the second one being the well known liquid water. In this molecular system, the effects of confinement on the structural properties of ice are studied by pouring water in graphene nanocapillaries, i.e. two graphite monolayers with a separation of a few Å.

Carbon is a unique and versatile element in the sense that it can form different architectures at nanoscale. While graphite and diamond are well known examples of crystalline structures consisting of carbon atoms, over the last years, different carbon allotropes have been synthesized spanning all spatial dimensions. In Fig. 1.8 a collection of carbon allotropes are illustrated arranged by

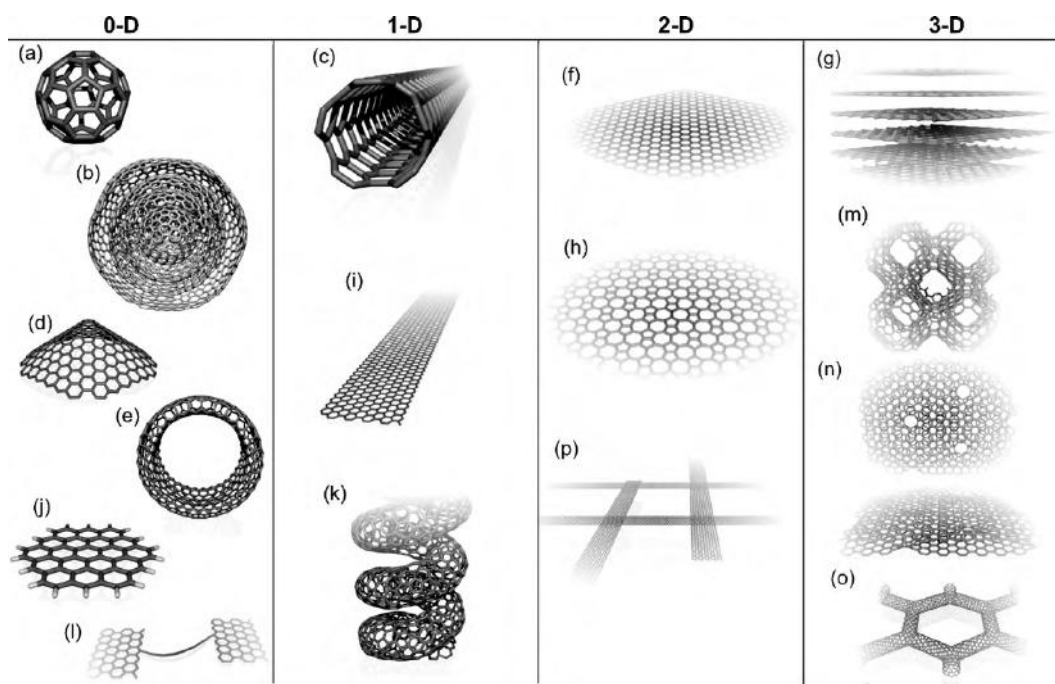


Figure 1.8 Carbon nanostructures exhibiting different dimensionalities: (a) buckminsterfullerene (so-called bucky-balls), (b) nested fullerenes or graphitic onions, (c) carbon nanotube, (d) nanocones or nanohorns, (e) nanotoroids, (f) graphene, (g) graphite, (h) Haeckelite surface, (i) graphene nanoribbons, (j) graphene clusters, (k) helicoidal carbon nanotube, (l) short carbon chains, (m) 3D Schwarzite crystals, (n) carbon nanofoams (interconnected graphene surfaces with channels), (o) 3D nanotube networks and (p) nanoribbon 2D networks (adapted from Ref. [34]).

their dimensionality. Fig. 1.8(f) depicts the famous honeycomb lattice of a graphite monolayer, i.e. graphene.

Since its experimental isolation in 2004 using the famous Scotch tape method to peel off carbon layer-by-layer from graphite [35], the two dimensional allotrope of carbon has generated an enormous amount of interest. Its many extraordinary properties have been explored, such as electronic spectrum [36], and transport properties [37], high Young's modulus [38] and excellent thermal conductivity [39].

With the discovery of the extraordinary properties of graphene, other possible candidates for two dimensional compounds have gained an increasing amount of attention. A variety of layered crystals with covalent in-plane bonds and van der Waals inter-plane interactions exist that could potentially be exfoliated into 2D materials. One of these materials that will be used later on is hexagonal boron nitride (h-BN) which is composed of alternating boron and nitrogen atoms in a honeycomb lattice

similar to this of graphene (see Fig. 1.9). Shortly after the discovery of graphene, free-standing

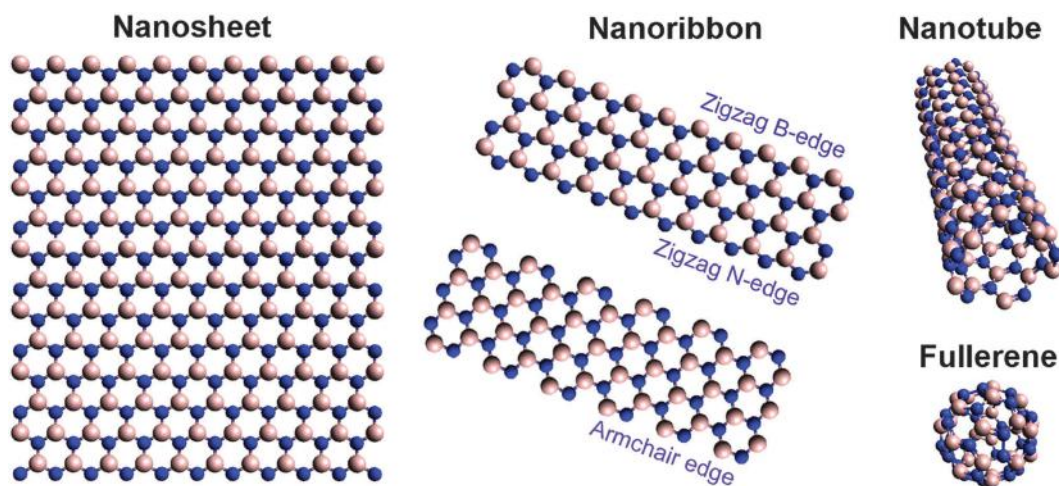


Figure 1.9 Structure models of 2D, 1D, and 0D boron nitride nanostructures similar to those of carbon. Alternating boron (nitrogen) atoms are indicated by blue (white) spheres (adapted from Ref. [40]).

h-BN was exfoliated from a BN crystal [41]. In Chapters 5 and 6 these monolayers will be used in order to confine water in a two-dimensional arrangement. For a detailed description of production methods and applications of these monolayers, the reader is recommended to read the review article by Novoselov et. al [42].

3 Organization of the thesis

The thesis is organized as follows:

Chapter 2 presents an introduction into the computation methodology which will be relevant for the performed calculations in this thesis. In particular, the inner workings of molecular dynamics simulations will be examined.

In Chapter 3 a two-dimensional model of Janus discs consisting of a hydrophobic and charged semicircle is investigated. The morphology of these particles, when confined in a channel-like environment, is studied. These Janus particles are shown to assemble into layered membranes, mimicking their biological counterparts.

In subsequent Chapter 4 the system of Janus discs that was introduced in the previous chapter will be expanded to three-dimensional Janus spheres. The interplay of the competing interactions

between the hydrophobic (attractive) hemispheres and the charged (repulsive) ones is exploited to assemble helical superstructures whose helicity can be controlled by altering the pH concentration of the solution.

Recently, it was found experimentally that confined water exists as a quasi two dimensional layer with different properties than those of bulk water. A square ice lattice was proclaimed to be discovered, and later disputed by several other authors. Chapter 5 is devoted to large scale molecular dynamics simulations of water confined in graphene nanocapillaries with a separation of a few angstroms.

In Chapter 6 a monolayer ice confined between two graphene layers is exposed to an external electric field, parallel to the channel. The ice monolayer is found to be polarized, resulting in ferroelectricity and electrical hysteresis.

CHAPTER 2

Molecular dynamic simulations

Molecular dynamics (MD) is a computational technique in which the motion of objects under the influence of physical forces is simulated, showing a dynamical evolution of the system [43]. It is widely used to simulate molecular systems consisting of a vast number of particles, which properties are impossible to determine analytically. Although MD is a useful technique to circumvent this problem, it has its own disadvantages: simulations need to be performed using an approximate Hamiltonian, which does not necessarily produce the same physics.

It is important to mention beforehand that we will only consider *classical* MD: processes that are governed by quantum physics are only taken into account in a mean-field manner. This is done by the parametrisation of a *force field*, which is the collective term for a functional form and parameter set that define the interaction potential between atoms. This parametrisation can be quite extensive: it consists of data particularizing the charge of atoms, van der Waals parameters, polarizability, bond lengths, bond angles, etc. The parameters can be derived from experimental work, quantum mechanical calculations, or other computational models (e.g. DFT [44]). Different force fields are available, most of which are designed for specific purposes [45–47]. In this thesis mainly one force field was used, i.e. ReaxFF [48], for which we will describe the parametrisation with more detail in Section 5.

Molecular dynamics has its basis in the deterministic properties of our world, and can be seen as a modern day equivalent to Laplace’s demon [49]:

We may regard the present state of the universe as the effect of its past and the cause of its future. An intellect that, at a given instant, could comprehend all the forces that set nature in motion, and all positions of all items of which nature is composed, if this intellect were also vast enough to submit these data to analysis, it would embrace in a single formula the movements of the greatest bodies of the universe and those of the lightest atoms. For such an intellect nothing would be uncertain and the future, like the past, would be open to its eyes.

MD is the particular realisation of this idea, namely that the dynamics of an arbitrary system could be calculable if the initial conditions and interacting forces are known. Applying this methodology to the complexity of an actual physical system, reality must be replaced with a model. If this model results in the same observations as in reality, the system is considered to be determined. As Lord Kelvin observed in one of his Baltimore lectures in 1884 [50]:

It seems to me that the test of "Do we or not understand a particular subject in physics?" is, "Can we make a mechanical model of it?"

MD is a methodology that clearly predates the invention of the computer, and indeed not many years after the introduction of digital computers the first MD steps were taken [51–53].

The theory for systems in equilibrium, statistical mechanics, has had a substantial rate of success in the conceptual point of view. Quantitative results however are scarce, and once out of equilibrium the theory has little to say. It is mainly due to MD simulations that progress is possible in the analysis of the dynamical and equilibrium properties of physical systems. Notwithstanding Laplace's statement of scientific determinism, we can still identify systems which are unpredictable (in the deterministic sense). We can classify these systems into two categories. The first classification consists of systems of which the objects interact non-linearly. For these systems, the equations of motion generally can not be solved analytically. The second classification consists of systems that are incalculable simply because of the large number of inputs needed, are needed with an unrealistic high precision, or because the algorithm is unstable for intermediate calculations.

This section will give an introduction to the basic principles and equations on which the MD method relies. Most of the content of this chapter is heavily influenced by the works of J.M. Haile's *Molecular dynamics simulation: elementary methods* [54] which focuses on the fundamental properties of M.D. simulations and D.C. Rapaport's *The Art of Molecular Dynamics simulation* [43], which is filled with computational techniques and practical examples of MD systems. Other noteworthy reference works can be found in the reference list [55–57]. Special attention will be given to methods which are important for the understanding of this thesis.

1 Schematic overview of MD simulations

Before exploring the inner workings of MD, a simplified description will be given of the standard molecular dynamics algorithm. An overview of the basic components of an MD simulation is shown in Fig. 2.1.

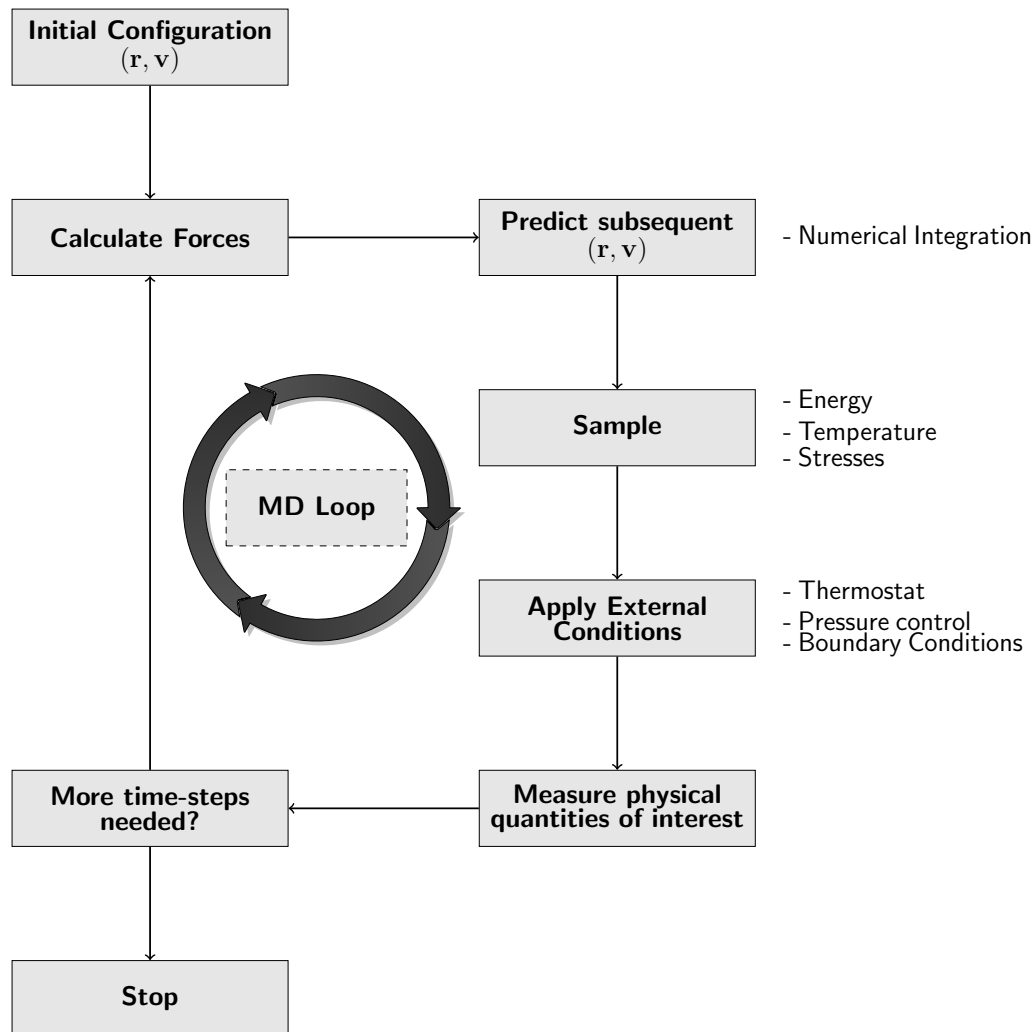


Figure 2.1 Schematic of a molecular dynamics algorithm. In order to study the physical movement of N molecules placed at initial positions $(\mathbf{r}, \mathbf{v}) = \{(\mathbf{r}_i, \mathbf{v}_i); i = 1, \dots, N\}$, Newton's equations of motion are solved numerically at each iteration of the MD loop.

In this technique, the classical equations of motion are solved for N particles, with mass m , that interact through a prescribed potential:

$$m\ddot{\mathbf{r}}_i(t) = \mathbf{F}_i(t), \quad i = \{1 \dots N\}, \quad (2.1)$$

where the force on particle i at time t , $\mathbf{F}_i(t)$, depends on the positions of the other particles in the system. The potential used is usually taken as pairwise additive; three-body and higher order-interactions need to be integrated in an *effective* pair potential V :

$$\mathbf{F}_i(t) = -\nabla_i \sum_{j=1}^N \sum_{j>i}^N V(\mathbf{r}_{ij}(t)), \quad (2.2)$$

where $\mathbf{r}_{ij}(t) = \mathbf{r}_i(t) - \mathbf{r}_j(t)$.

In Chapters 5 & 6, interactions between water molecules were studied. In order to accurately study the formation and breaking of bonds, an accurate pairwise description of molecules needs to be used. In Section 5 the implementation of these more extensive properties in the context of pair potentials will be discussed in detail.

The initial configuration for the simulations that were performed in this thesis, is composed to represent a system in thermal equilibrium. Therefore, apart from assigning a certain amount of static properties (such as mass or charge) to each object in the system, the objects must be initialized at a certain temperature. This is achieved by assigning the initial velocities randomly from a Maxwell-Boltzmann distribution at the desired initial temperature T :

$$f(v) = \left(\frac{m}{2\pi k_B T} \right)^{\frac{3}{2}} 4\pi v^2 e^{-\frac{mv^2}{2k_B T}} \quad (2.3)$$

where m is the mass and k_B is the Boltzmann's constant. When suspensions are considered, the Brownian motion of the suspended particles needs to be taken into account. To model the randomized motion of a particle which is subjected to collisions with molecules in the fluid, the concept of a random walk is typically used. A stochastic force $\xi(t)$ is added to Eq. (2.1) that gives the effect of a background noise due to the fluid on the Brownian particle. The amount of noise that is added to the motion of the suspended particle is given by a Gaussian distribution with mean $\mu = 0$ and variance $c^2 = 2Dt$, where D is the macroscopic diffusion constant given by:

$$D = \frac{k_B T}{6\pi\eta\sigma}, \quad (2.4)$$

with k_B Boltzmann's constant, T the temperature, η the viscosity of the liquid and σ the radius of the suspended particle [58].

During the actual MD loop, a careful balance must be held between the conservation of energy on the one hand, and the desire to have the system at thermal equilibrium at a certain temperature. Internally, this is handled by the *thermostat* of the system. The essential workings of the used thermostats will be discussed in section 6.3.

During the course of a single simulation, a huge amount of data is generated at each time-step: positions, velocities, forces, energies, temperatures, and so on. With this information, quantities of physical interest can be computed. For example, the average kinetic energy of a system with N particles during a simulation of length Δs equals

$$\langle E_{kin} \rangle_{\Delta s} = \frac{1}{\Delta s} \int_0^{\Delta s} \left[\sum_{i=1}^N \frac{1}{2} m_i v_i^2(t) \right] dt. \quad (2.5)$$

If the simulation in the above example was done for the system in thermodynamic equilibrium, one might expect above averaged quantity to be a representation of the general behaviour of the system in equilibrium. A formal version of this statement is given by the *ergodic hypothesis* which states that in the limit of $\Delta s \rightarrow \infty$ the time average that appears in expressions such as Eq. (2.5) can be considered as an ensemble average [59].

2 Integration schemes

The equations of motion in Eq. (2.1) must be integrated numerically to find the proper positions at the next time-step of the MD loop. When choosing the proper integration method there are several points to be taken into consideration. A short-list of preferable features could be summarized as follows:

- (a) It should be fast and memory efficient.
- (b) It should duplicate classical trajectories as closely as possible.
- (c) It should satisfy energy & momentum conservation laws, and be time-reversible.
- (d) It should be simple in form and easy to program.

Not all these points are of importance when working in a MD framework. Compared with the time-consuming force calculation, the speed of the time-integration scheme is not crucial. The algorithm discussed below has been chosen with criterion (b) in mind, but it is unreasonable to expect that the approximate solution will follow the classical trajectory over many hundreds of iterations. Depending on the interaction potentials used, a small perturbation associated with finite precision arithmetic can cause the generated trajectory to diverge from the classical path in a few 100 time-steps [60, 61]. This effect is illustrated in Fig. 2.2, where the position of a single molecule in a system of particles (interacting through a Lennard-Jones potential) is displaced in a random direction from

its reference position at $t = 0$ by a fraction of the particle diameter σ ($10^{-4} \sigma$ (green) and $10^{-6} \sigma$ (orange) respectively). In all other aspects, the runs are identical and correspond with the same total energy. The trajectories however are not, and diverge exponentially.

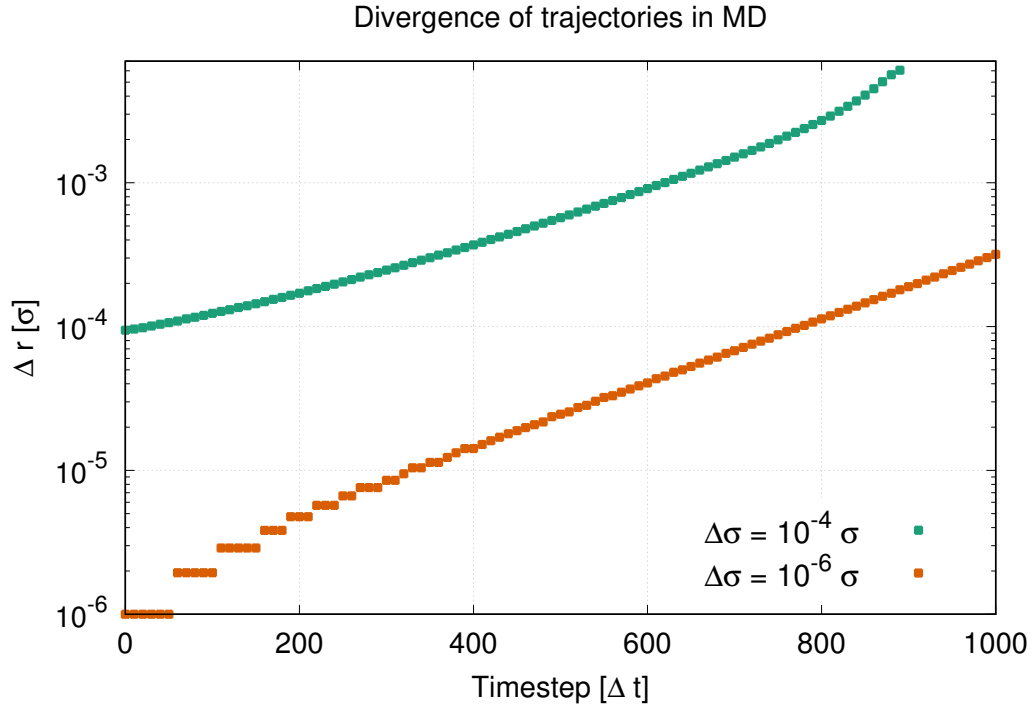


Figure 2.2 Divergence of trajectories in MD. The curves indicate the separation distance Δr between perturbed and reference trajectories in units of particle diameter σ of a single particle in a system of atoms interacting through a LJ potential.

Fortunately, we do not need to generate classical paths over a multitude of time-steps. We want to use this method to generate states that lie in the same ensemble. The path of each individual particle can deviate from its classical path as long as the particle trajectory lays on the appropriate constant energy hyper-surface in phase space. A good numerical integrator allows for an acceptable conservation of energy (and momentum) for a large time-step used during the integration. In general, the size of one time-step depends on the type of system that is studied and should be chosen according to the shape of the potential energy landscape and characteristic particle velocities. Shorter time-steps should be used at high temperatures, for light molecules, and for rapidly fluctuating potentials [62].

3 Velocity Verlet algorithm

The most commonly used method for integrating equations of motion was initially adopted by Verlet [63] and is attributed to Störmer [64] although there is evidence that this method was already known by Newton and was used in his *Principia* [65] in 1687 to prove Kepler's second law [66]. By far the simplest way to derive this numerical integration scheme is by performing a Taylor expansion about time t of the coordinate of a particle $\mathbf{r}(t)$

$$\mathbf{r}_i(t + \Delta t) = \mathbf{r}_i(t) + \mathbf{v}_i(t)\Delta t + \frac{\mathbf{F}_i(t)}{2m}\Delta t^2 + \mathcal{O}(\Delta t^3), \quad (2.6)$$

where the velocities are updated using

$$\mathbf{v}_i(t + \Delta t) = \mathbf{v}_i(t) + \frac{\Delta t}{2m} [F(x(t)) + F(x(t + \Delta t))], \quad (2.7)$$

which is subjected to errors of the order of Δt^2 . The combination of Eqs. (2.6) and (2.7) is what is known as the velocity Verlet algorithm. The use of this algorithm over another time integration scheme seems to be ad hoc, especially when looking at the exponential growth of small perturbations in single particle trajectories as shown in Fig. 2.2. In Appx. A a formal derivation is given in which the velocity Verlet algorithm is recovered from the classical propagator, by using the Trotter theorem to find approximate solutions. Using this formalism, it is possible to show that for a finite time-step Δt , the classical Hamiltonian will be distorted by a factor $\mathcal{O}(\Delta t^3)$ for which the velocity Verlet algorithm is a symplectic, unitary, time-reversible propagation scheme that preserves important symmetries of classical mechanics. And lastly, it can be shown that in the limit of $\Delta t \rightarrow 0$, classical mechanics can be recovered. In this chapter however, a pragmatic approach is followed. We will show the most significant property, namely that the Verlet algorithm is an *symplectic* integrator, which conserves the phase space of a slightly perturbed Hamiltonian.

3.1 Symplecticity of the velocity Verlet algorithm

3.1.1 Hamilton's equations

A property of Hamilton's equations is the so-called symplectic structure of the equations of motion. Recall that the Hamiltonian of a classical system is simply the total energy of the system expressed as a function of positions and momenta:

$$\mathcal{H}(\mathbf{r}_1, \dots, \mathbf{r}_N, \mathbf{p}_1, \dots, \mathbf{p}_N) = \sum_{i=1}^N \frac{\mathbf{p}_i^2}{2m_i} + U(\mathbf{r}_1, \dots, \mathbf{r}_N). \quad (2.8)$$

Given the Hamiltonian of a system, the equations of motion can be obtained according to

$$\frac{\partial \mathbf{r}_i}{\partial t} = \frac{\partial \mathcal{H}}{\partial \mathbf{p}_i} \qquad \frac{\partial \mathbf{p}_i}{\partial t} = -\frac{\partial \mathcal{H}}{\partial \mathbf{r}_i}, \quad (2.9)$$

which are known as *Hamilton's equation of motion*, and are a completely equivalent form of Newton's second law of motion. Simply evaluating the derivatives for \mathcal{H} yields:

$$\begin{aligned} \dot{\mathbf{r}}_i &= \frac{\partial \mathcal{H}}{\partial \mathbf{p}_i} = \frac{\mathbf{p}_i}{m_i} \\ \dot{\mathbf{p}}_i &= -\frac{\partial \mathcal{H}}{\partial \mathbf{r}_i} = -\frac{\partial U}{\partial \mathbf{r}_i} = \mathbf{F}_i(\mathbf{r}), \end{aligned} \quad (2.10)$$

which results in

$$\dot{\mathbf{p}}_i = m_i \ddot{\mathbf{r}}_i = \mathbf{F}_i(\mathbf{r}) \quad (2.11)$$

Hamilton's equations are known to conserve the total Hamiltonian. In order to see this, the time derivative $d\mathcal{H}/dt$ is computed using the chain rule in generalized coordinates $(\mathbf{r}, \mathbf{p}) = (r_1, \dots, r_{3N}, p_1, \dots, p_{3N})$:

$$\begin{aligned} \frac{d\mathcal{H}}{dt} &= \sum_{\alpha=1}^{3N} \left[\frac{\partial \mathcal{H}}{\partial r_{\alpha}} \dot{r}_{\alpha} + \frac{\partial \mathcal{H}}{\partial p_{\alpha}} \dot{p}_{\alpha} \right] \\ &= \sum_{\alpha=1}^{3N} \left[\frac{\partial \mathcal{H}}{\partial r_{\alpha}} \frac{\partial \mathcal{H}}{\partial p_{\alpha}} - \frac{\partial \mathcal{H}}{\partial p_{\alpha}} \frac{\partial \mathcal{H}}{\partial r_{\alpha}} \right] \\ &= 0 \end{aligned} \quad (2.12)$$

The final property of Hamilton's equations that will be commented upon is the symplectic structure of the equations of motion. These equations of motion characterize the unique evolution of the coordinates and momenta of a classical system. They specify a trajectory in phase space as

$$x_t = (r_1(t), \dots, r_{3N}(t), p_1(t), \dots, p_{3N}(t)), \quad (2.13)$$

for which the energy is conserved. The Hamilton's equations can be written directly in terms of the phase space vector as

$$\dot{x} = \eta(x), \quad (2.14)$$

since

$$x = (r_1, \dots, r_{3N}, p_1, \dots, p_{3N}), \quad (2.15)$$

$\eta(x)$ must be of the form:

$$\eta(x) = \left(\frac{\partial \mathcal{H}}{\partial p_1}, \dots, \frac{\partial \mathcal{H}}{\partial p_{3N}}, -\frac{\partial \mathcal{H}}{\partial r_1}, \dots, -\frac{\partial \mathcal{H}}{\partial r_{3N}} \right). \quad (2.16)$$

Using this notation the Hamilton's equations can be written in the following way:

$$\dot{x} = M \frac{\partial \mathcal{H}}{\partial x}, \quad (2.17)$$

where M is a matrix of the form:

$$\begin{pmatrix} O & I \\ -I & O \end{pmatrix} \quad (2.18)$$

where O and I are respectively $3N \times 3N$ zero and identity matrices. Dynamical systems that can be expressed in the form of Eq. (2.17) are said to have a symplectic structure. If we consider the Hamiltonian to define a region in phase space that connects a range of positions and momenta to a certain energy, the symplectic structure defines the form of the cotangent bundle of this region which gives the time-evolution of the system. It takes a particular simple form, it essentially expresses the minus sign in Hamilton's equations.

Because the solution of Hamilton's equation is unique for each initial condition, x after a time t will be uniquely defined by the initial phase space vector x_0 , i.e. $x_t = x_t(x_0)$. This means that the time-evolution can be seen as a unique variable transformation on the phase space from an initial phase space coordinate x_0 to a new set x_t . The Jacobian of this transformation is defined by:

$$J_{kl} = \frac{\partial x_t^k}{\partial x_0^l}, \quad (2.19)$$

and satisfies following condition:

$$M = J^T M J \quad (2.20)$$

Transformations that satisfy Eq. (2.20) are said to be symplectic, which means they keep the form of the evolution of the phase space vector as given by Hamilton's equations.

3.1.2 Symplecticity of numerical integrators

Numerical integrators do not exactly solve the equations of motion, they rather give a prediction as to where the phase space vector will move to after a time-step Δt . We will show that the velocity Verlet algorithm (that was introduced in Eqs. (2.6, 2.7)) is symplectic, by considering the Jacobian matrix of the coordinate transformation of a particle in a one dimensional system. The velocity Verlet scheme for this system is equal to:

$$\begin{aligned} x(\Delta t) &= x(0) + \Delta t \frac{p(0)}{m} + \frac{\Delta t^2}{2m} F(x(0)) \\ p(\Delta t) &= p(0) + \frac{\Delta t}{2} [F(x(0)) + F(x(\Delta t))], \end{aligned} \quad (2.21)$$

for which the following Jacobian corresponds to:

$$J = \begin{pmatrix} J_{11} & J_{12} \\ J_{21} & J_{22} \end{pmatrix} \quad (2.22)$$

with

$$\begin{aligned} J_{11} &= \frac{\partial x(\Delta t)}{\partial x(0)} = 1 + \frac{\Delta t^2}{2m} F'(x(0)), \\ J_{12} &= \frac{\partial x(\Delta t)}{\partial p(0)} = \frac{\Delta t}{m}, \\ J_{21} &= \frac{\partial p(\Delta t)}{\partial x(0)} = \frac{\Delta t}{2} F'(x(0)) + \frac{\Delta t}{2} \left[F' \left(x(0) + \frac{\Delta t}{m} p(0) + \frac{\Delta t^2}{2m} F(x(0)) \right) \left(1 + \frac{\Delta t^2}{2m} F'(x(0)) \right) \right], \\ J_{22} &= \frac{\partial p(\Delta t)}{\partial p(0)} = 1 + \frac{\Delta t^2}{2m} F' \left(x(0) + \frac{\Delta t}{m} p(0) + \frac{\Delta t^2}{2m} F(x(0)) \right). \end{aligned} \quad (2.23)$$

Taking the product $J^T M J$ gives:

$$\begin{pmatrix} 0 & J_{11}J_{22} - J_{21}J_{12} \\ -(J_{11}J_{22} - J_{12}J_{21}) & 0 \end{pmatrix}, \quad (2.24)$$

where

$$\begin{aligned} J_{11}J_{22} - J_{21}J_{12} &= \left[1 + \frac{\Delta t^2}{2m} F'(x(0)) \right] \left[1 + \frac{\Delta t^2}{2m} F' \left(x(0) + \frac{\Delta t}{m} p(0) + \frac{\Delta t^2}{2m} F(x(0)) \right) \right] \\ &\quad - \frac{\Delta t^2}{2m} F'(x(0)) - \frac{\Delta t^2}{2m} F' \left[x(0) + \frac{\Delta t}{m} p(0) + \frac{\Delta t^2}{2m} F(x(0)) \right] \left[1 + \frac{\Delta t^2}{2m} F'(x(0)) \right] \\ &= 1 \end{aligned} \quad (2.25)$$

which shows that the velocity Verlet algorithm is indeed symplectic. Symplectic integrators have as a conserved quantity, a Hamiltonian which is slightly perturbed from the original one, which is often called the *shadow Hamiltonian*.

3.2 Shadow theorem

Although numerical integrators can not precisely conserve the Hamiltonian \mathcal{H} of the system, symplectic integrators have the property that there exists a Hamiltonian $\tilde{\mathcal{H}}(x, \Delta t)$ that is exactly conserved by the integrator, and remains close to the true Hamiltonian. Their closeness is expressed by

$$\lim_{\Delta t \rightarrow 0} \tilde{\mathcal{H}}(x, \Delta t) = \mathcal{H}(x). \quad (2.26)$$

Because this external Hamiltonian stays near ('shadows') the real one, it is referred to as a shadow Hamiltonian [67, 68]. The existence of $\tilde{\mathcal{H}}$ ensures that the error in a symplectic map is bounded, and is the defining property of an integrator for its use in the framework of molecular dynamics. The existence of this Hamiltonian does not mean that its general form can be constructed for any given system. The shadow theorem proves only its existence, but does not give a procedure into actually constructing one [69].

The proof of the existence of $\tilde{\mathcal{H}}$ is given in Appx. A. In this chapter a practical example is given for which the shadow Hamiltonian can be constructed. Consider a one-dimensional harmonic oscillator, given by

$$\mathcal{H} = p^2/2m + kx^2/2, \quad (2.27)$$

for which Hamilton's equations of motion $\dot{x} = p/m$, $\dot{p} = -m\omega^2 x$ are solved by the velocity Verlet algorithm as follows:

$$\begin{aligned} x(\Delta t) &= x(0) + \Delta t \frac{p(0)}{m} - \frac{1}{2} \Delta t^2 m \omega^2 x(0) \\ p(\Delta t) &= p(0) - \frac{m \omega^2 \Delta t}{2} [x(0) + x(\Delta t)]. \end{aligned} \quad (2.28)$$

It can be show that the Hamiltonian

$$\tilde{\mathcal{H}}(x, p; \Delta t) = \frac{p^2}{2m(1 - \omega^2 \Delta t^2/4)} + \frac{1}{2} m \omega^2 x^2, \quad (2.29)$$

is exactly conserved by the algorithm [57]. Eq. (2.29) is an ellipse of which its eccentricity depends on Δt . If $\Delta t = 2/\omega$, $\tilde{\mathcal{H}}$ diverges and for $\Delta t > 2/\omega$ the trajectories are no longer bounded. For any reasonable time-step, the difference between true phase space and that of the Verlet scheme will be almost equivalent. In Fig. 2.3 the phase space of $\tilde{\mathcal{H}}$ is shown for a time-step Δt of (0.1, 0.05, 0.001) for a harmonic oscillator with $m = \frac{1}{2}$ and $\omega = 1.1$ in unitless coordinates.

It is possible to develop new simulation techniques based on the knowledge of $\tilde{\mathcal{H}}$ [70], but in the context of this thesis, the existence of $\tilde{\mathcal{H}}$ is used as a guarantee that the error in the symplectic transformations of the Verlet algorithm is bounded. This means that when a trajectory $\tilde{x}_{n\Delta t}, n =$

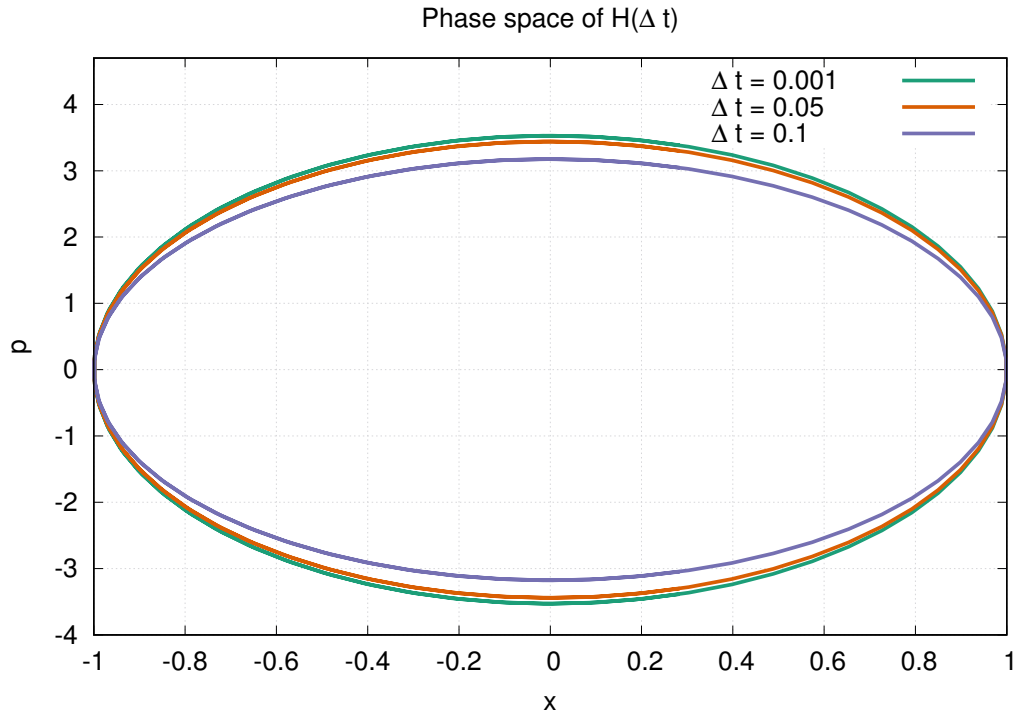


Figure 2.3 Phase space of the shadow Hamiltonian $\tilde{\mathcal{H}}$ corresponding to a harmonic oscillator for the velocity Verlet scheme.

$0, 1, 2, \dots$ is generated by a symplectic integrator, $\mathcal{H}(\tilde{x}_{n\Delta t})$ should not drift away from the true conserved value of $\mathcal{H}(x_t)$ along the exact classical trajectory x_t . This certainly does not mean that $\tilde{x}_{n\Delta t}$ will follow the classical path x_t . The statement that is made is that $\tilde{x}_{n\Delta t}$ will remain on an energy hypersurface that is close to the true constant energy surface.

This subtle, but important difference will be clarified by generating trajectories for the harmonic oscillator system outlined above in Eq. (2.28). In Fig. 2.4(a) the resulting trajectories are given for the values of $\Delta t = 0.001, 0.05, 0.1$ (for which the phase space was shown in Fig. 2.3) for the first few oscillations. In subfigure 2.4(b) the corresponding trajectories in (x, p) space is shown in accordance with Fig. 2.3. It may appear that the number of states dramatically increases at higher values of Δt , but this is not the case. For each time-step, the particle travels linearly from one state to the next. As the duration of the time-step increases, the linear motion starts to deviate further from the classical path which causes the apparent filling on the ellipse. This is shown in the inset of Fig. 2.4(b).

Lastly, the ratio between the energy of the numerically calculated trajectories is compared with the one of the classical path. For the smallest considered time-step there is an excellent agreement

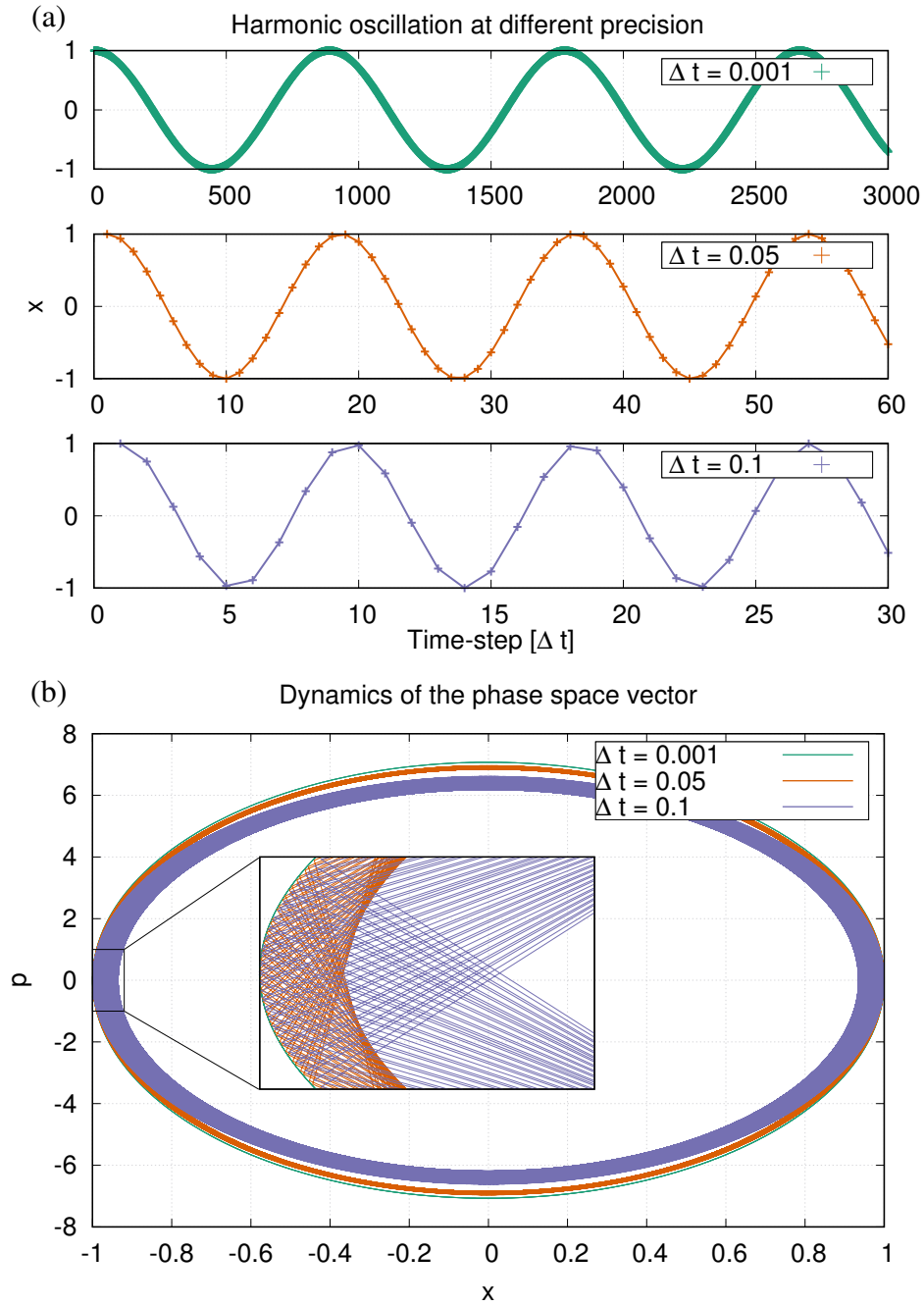


Figure 2.4 Numeric solutions of the harmonic oscillator Hamiltonian using the Velocity Verlet scheme: (a) depicts the oscillatory motion as function of time for the first few oscillations, in (b) the corresponding phase space trajectory is portrayed. The inset shows individual trajectories, which results in the phase space appearing broader than it actually is.

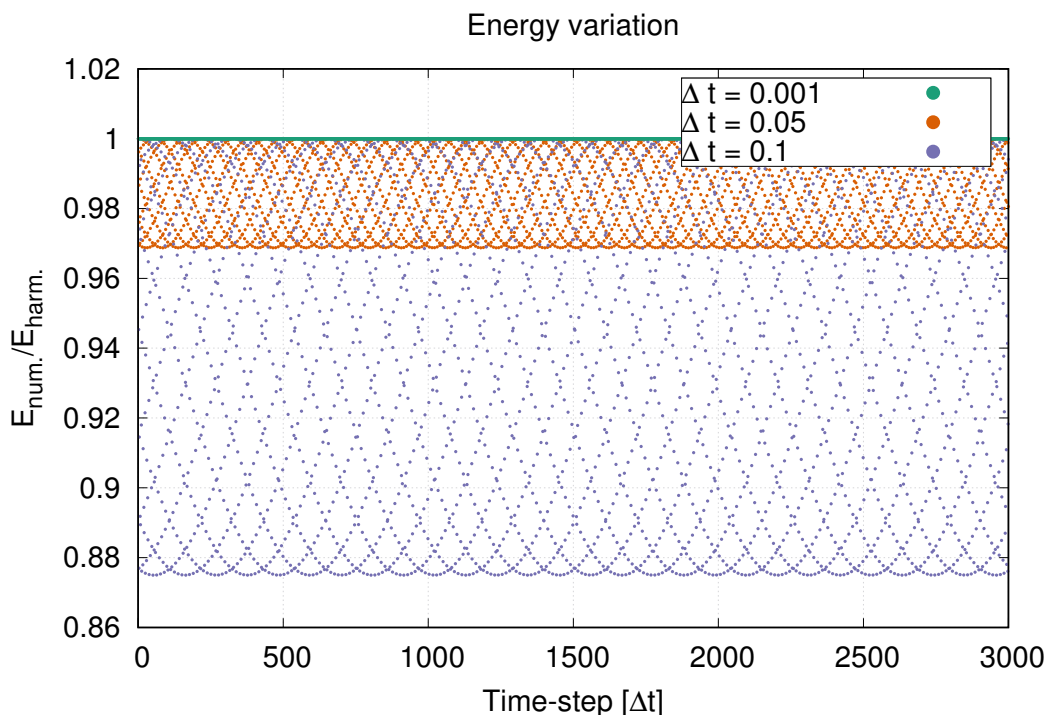


Figure 2.5 Ratio of the numerically calculated energy to the Hamiltonian of the classical system for a harmonic oscillator. For $\Delta t = 0.05, 0.1$ the mean energy is significantly lower.

between the two. For $\Delta t = 0.05$ & 0.1 however, the energy fluctuates around energies that are significantly lower. But more importantly, there is no energy drift present: the energies fluctuate around a fixed value¹.

While there are integrators for which the particle trajectories are more accurate than the Verlet algorithm (for example Runge [72]-Kutta [73] or the class of predictor-corrector methods [74]), these are in general neither symplectic nor time-reversible, which results in significant energy drifts [57]. Many alternatives to the Verlet algorithm exist [71, 75–77], that also conserve phase space while having errors in higher orders of Δt , though they are often complicated to implement and are in generally not worth the complications they bring [78].

¹When performing extremely long simulations, one might expect some energy drift to occur, as small errors arising from finite arithmetic can start to accumulate. In [71] however Toxvaerd et al. showed analytically for a representative system of 2000 LJ particles that energy conservation is not sensitive to round-off errors.

4 Colloidal interaction potentials

Modelling matter is based on a comprehensive description of the constituent particles. MD adopts a classical point of view, typically representing atoms as point masses interacting through pair-potentials that depend on their separation. These effective potentials should not be taken too literally. They are descriptions of the true physical systems and undergo refinements as new comparisons between simulation and experimental observations become available. Whenever the evidence against a particular model becomes overwhelming, a new model must be developed [79].

4.1 Hard-sphere potential

The rigid sphere model is widely used to simulate the harsh repulsion that appears at short range when two particles tend to overlap [80]. The pair potential between two hard-spheres with a radius σ as a function of the inter-particle distance r is given by:

$$\begin{cases} U_{hs}(r) = \infty, & r < 2\sigma \\ U_{hs}(r) = 0, & r > 2\sigma, \end{cases} \quad (2.30)$$

This simple potential captures the impenetrability of hard surfaces, but leads to divergent forces when used in MD simulations. A practical way to implement the hard-sphere characteristic of colloidal particles, is to use an elastic repulsion, given by:

$$\begin{cases} U_{ss}(r) = \varepsilon (2\sigma - r)^n, & r < 2\sigma \\ U_{ss}(r) = 0, & r > 2\sigma, \end{cases} \quad (2.31)$$

which is named the soft-sphere model [81]. The values of the elastic constant ε and the parameter n can be selected to define the 'hardness' of an object, with respect to other forces that are present in the system. The advantage of this potential form is that it is continuously differentiable, in contrast to the hard-sphere potential, and can easily be implemented in a MD system.

4.2 Hydrophobic attraction

The term hydrophobic bond was coined by Kauzmann [82] in 1959 to describe the tendency of non-polar groups of proteins to coagulate in aqueous solutions. The use of the word "bond" was considered inappropriate [83] and further work [84, 85] indicated that hydrophobic bonding should be viewed as the spontaneous tendency of non-polar groups to adhere in water in order to minimize their

contact with water molecules. There is no description of this force as a pairwise additive interaction potential, and different relations have been measured depending on the type of molecules and surfaces studied [86]. Interaction ranges have been reported to be from 100 \AA to values as large as 0.3 \mu m [86].

In Chapters 3-4, colloids comprised of two distinct hemispheres are studied where one of the hemispheres is hydrophobic. As there exists no closed form for the pair-potential, a harmonic potential is often introduced to mimic these hydrophobic bonds:

$$\begin{cases} U_{HP}(r) = -\frac{\kappa}{2}(2\sigma_H - r)^2, & r < 2\sigma_H \\ U_{HP}(r) = 0, & r > 2\sigma_H, \end{cases} \quad (2.32)$$

where σ_H is the radius, and κ the coupling constant of the interaction. A typical illustration of this interaction is depicted in Fig. 2.6 for two Janus particles having a hydrophobic hemisphere. As the density of water molecules near the presence of these non-polar surfaces is lower than on the opposite sides, a pressure gradient squeezes the two colloids together.

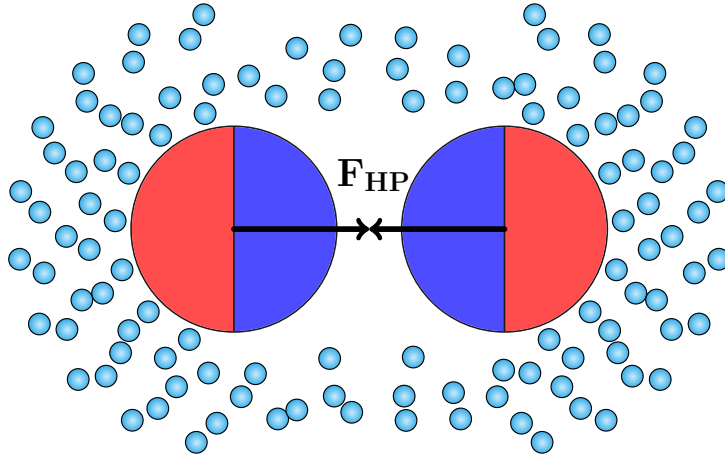


Figure 2.6 Typical schematic of the hydrophobic attraction present between non-polar surfaces. As the density of water molecules is lower near the presence of a hydrophobic surface, a pressure drop between the colloids squeezes them together.

4.3 Derjaguin-Landau-Verwey-Overbeek (DLVO) potential

DLVO theory quantitatively describes the force between charged surfaces interaction through a liquid medium. It combines the effect of the van der Waals attraction and electrostatic repulsion due to the double layers of counter-ions in the suspension. Considering two colloids as big spheres, with radius

σ , separated at a distance r , the van der Waals interaction energy can approximately be written as:

$$U_{vdW}(r) = -\frac{1}{6}A \left[\frac{2\sigma^2}{r^2 - 4\sigma^2} + \frac{2\sigma^2}{r^2} + \ln \left(\frac{r^2 - 4\sigma^2}{\sigma^2} \right) \right], \quad (2.33)$$

which was derived by Hamaker in 1937 [87]. The constant A appearing in Eq. (2.33) is known as the Hamaker's constant. We will use the estimation given by Israelachvili [21], although different approximations to this constant exist [88]:

$$A \propto \frac{(n_1 + n_2)^2 (n_1 - n_2)^2}{(n_1^2 + n_2^2)^{3/2}}, \quad (2.34)$$

where n_1, n_2 are refractive indexes of the colloid and solvent, respectively. For $n_1 = n_2$, the van der Waals interaction can be suppressed. For materials where $n_1 \neq n_2$, the vdW potential (as depicted in Eq. (2.33)) diverges negatively for neighbouring colloids when $r \rightarrow 4\sigma$.

A different effect that plays a role here is the *charge stabilization* of the suspension. Suppose that every colloid has a certain amount of electric charge corresponding to it, which is called the bare charge $Z|e|$, where e stands for the elementary charge. When colloids are in contact with a polar solvent (like water) or have dissociated when in contact with the solvent, there is a concentration of counter ions that is the highest near the solid surface and decreases as the distance from the surface increases. These ions undergo Brownian motion, are subjected to Coulombic forces and form an inhomogeneous cloud around the centre of each colloid, which is called the electrical double-layer. In Fig. 2.7 a schematic illustration is given of the double-layer around a negatively charged colloid: the closest layer of counter-ions form a firmly attached shell around the surface of the colloid; this layer is known as the *Stern* or *Helmholtz layer*. Additional positive ions are still attracted by the negative colloid, but are also repelled by the Stern layer as well as by other positive ions that are approaching the colloid. The resulting dynamics are the cause of the formation of a *diffuse layer* of ions. In this layer, the concentration of positively charged ions gradually decreases with distance, until it reaches equilibrium with the negative ions in the solution. In order to include the bonded counter-ions, the bare charge Z can be re-normalized to a new value, which is called the *effective charge* Z_{eff} , which is smaller than Z . The value of the effective charge will depend on the geometry of the particle, colloidal concentration, and the solvent [89]. The diffusive layer proves itself more difficult to take into account: the charge distribution of a mobile cloud of ions needs to be calculated. This is achieved by combining the Boltzmann equation (in order to find the distribution of ions) with Poisson's equation. The resulting Poisson-Boltzmann equation is a non-linear differential equation that can not be solved directly. DLVO theory was thought out to approximate the resulting force

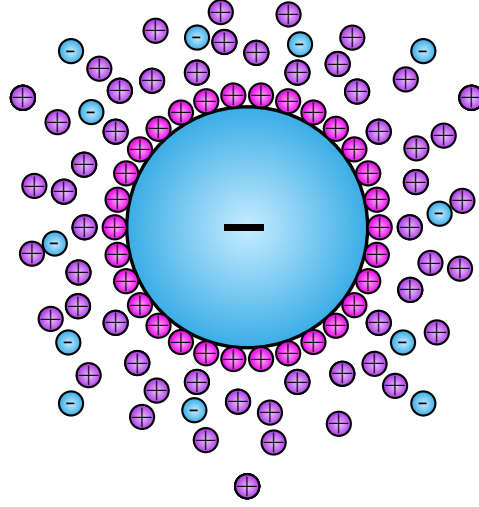


Figure 2.7 Schematic illustration of the electrical double-layer formed around a negatively charged colloid. The inner layer of counter-ions is called the Stern layer, around it a cloud of positive and negative ions form the diffuse layer.

between two charged colloids, combining the van der Waals (vdW) interaction with the electrostatic double layer [90].

The resulting pair interaction potential between two colloids is given by a screened Coulomb potential with additional pre-factors that describe the thickness and effectiveness of the double layer:

$$U(r) = Z_{eff}^2 \lambda_B \left(\frac{\exp(\kappa \sigma)}{1 + \kappa \sigma} \right)^2 \frac{\exp(-\kappa r)}{r}, \quad (2.35)$$

where two parameters appear: λ_B , the Bjerrum length scale, and the Debye-Hückel screening length κ . The Bjerrum length is given by

$$\lambda_B = \frac{e^2}{4\pi\epsilon_0\epsilon_r k_B T}, \quad (2.36)$$

where e again is the elementary charge, ϵ_r is the relative dielectric constant of the solution and ϵ_0 is the vacuum permittivity. It is often described as the separation distance for which the electrostatic interaction between two elementary charges is comparable to the thermal energy $\kappa_B T$.

Whereas the Debye-Hückel screening length κ is related to the thickness of the diffusive layer as κ^{-1} and is given by the relation:

$$\kappa = \sqrt{4\pi\lambda_B n} \quad (2.37)$$

with λ_B the screening length defined above and n the ion-concentration in the suspension.

4.4 Light as an external potential for colloidal particles

In Chap. 3-4 systems of patchy colloids are investigated that are confined to a channel by means of an external potential. Light forces acting on small particles have been studied in great detail [91]. In the following, we will give a brief description of the basic interactions between colloids and external potentials generated by laser light. We will outline the two features which are the most important in our work, namely the so called scattering force F_{scat} , for which the direction of the beam is of importance, and the gradient force F_{grad} , which depends on the shape of the light intensity distribution.

4.4.1 Scattering force

Light pressure of a laser beam exerts a force on a colloidal particle. In absorbing a photon with frequency ν , wavelength λ and phase velocity v_p , an object will experience a force

$$F_{scat} = \frac{\partial p}{\partial t} = \frac{\partial p}{\partial t} = \frac{\partial(h/\lambda)}{\partial t} = \frac{\partial(E_{phot}/v_p)}{\partial t} = P/v_p, \quad (2.38)$$

where P is the power of the photon source. In most cases, photons are rather scattered than absorbed and only transfer a fraction q of their momentum. A pre-factor of $q \approx 0.1$ is mostly assumed [92]. In a typical experiment F_{scat} is calculated to be in the order of a tenth of the particles' own weight for each mW of applied laser power [93].

4.4.2 Gradient force

The gradient force F_{grad} allows a single beam to act as an optical trap. The shape and size of the trap(s) can be modified by altering the shape of the wave bundle. Colloidal particles are dielectric objects and can become polarized by the laser. If we consider the electric field over a particle to be approximately uniform, a dipole moment $\mathbf{p} = \alpha \mathbf{E}$ is induced, where α is the polarizability of the particle given by the Clausius-Mosotti relation [94]:

$$\alpha = n_s^2 \frac{n^2 - 1}{n^2 + 2} \sigma^3, \quad (2.39)$$

where $n = n_c/n_s$ is the ratio between the refractive index of the colloidal particle (n_c) and that of the surrounding solvent n_s , and σ is the particle radius. Having acquired a dipole moment, the particle

experiences a Lorentz force F_L :

$$\begin{aligned} F_L &= (\mathbf{p} \cdot \nabla) \mathbf{E} + \frac{1}{c} \frac{\partial \mathbf{p}}{\partial t} \times \mathbf{B} \\ &= \alpha \left(\nabla \left(\frac{1}{2} E^2 \right) + \frac{1}{c} \frac{\partial}{\partial t} (\mathbf{E} \times \mathbf{B}) \right). \end{aligned} \quad (2.40)$$

The second term in Eq. (2.40) is the scattering force F_{scat} discussed above, and is directed along the propagation direction. The first term is the gradient force

$$F_{grad} = \frac{\alpha}{2} \nabla E^2, \quad (2.41)$$

and expresses that in a non-uniform electric field, a particle moves towards regions of higher (lower) electric field for $n_c > n_s$ ($n_c < n_s$).

The remarkable consequence is that it becomes possible to study the motion of Brownian particles under the influence of light-induced potentials. Ashkin is credited as being the first one to realise this [95], leading ultimately to his invention of *optical tweezers* in 1986 [96]. They are now a widely used tool in different disciplines of physics, biology and chemistry as a method to move, rotate, and trap mesoscopic objects [93, 92, 97]. In figures 2.8-2.9, experimental results are shown where optical tweezers were used to confine colloidal particles in a region, or to move them to precise positions aiding in the formation of colloidal crystals.

4.5 Creation of quasi-1D periodic potentials

A conceptually simple set-up for creating a quasi-1D periodic potential consists of two overlapping expanded laser beams with the same intensity. An example of an experimental set-up is given in Fig. 2.10: two coherent laser beams are created by a beam-splitter and impinges at an angle $\theta/2$ and $-\theta/2$ on the $x-y$ plane of the sample for the two beams respectively. The wave vectors corresponding with the laser beams have the same modulus, $|\mathbf{K}_1| = |\mathbf{K}_2| = \mathbf{K}$, and the same angle ϕ in the y -direction. Because of the crossing angle θ between the two bundles in the x -direction, the x component of the wave vector equals:

$$\begin{aligned} K_{1,x} &= |\mathbf{K}| \sin(\theta/2) \\ K_{2,x} &= |\mathbf{K}| \sin(-\theta/2), \end{aligned} \quad (2.42)$$

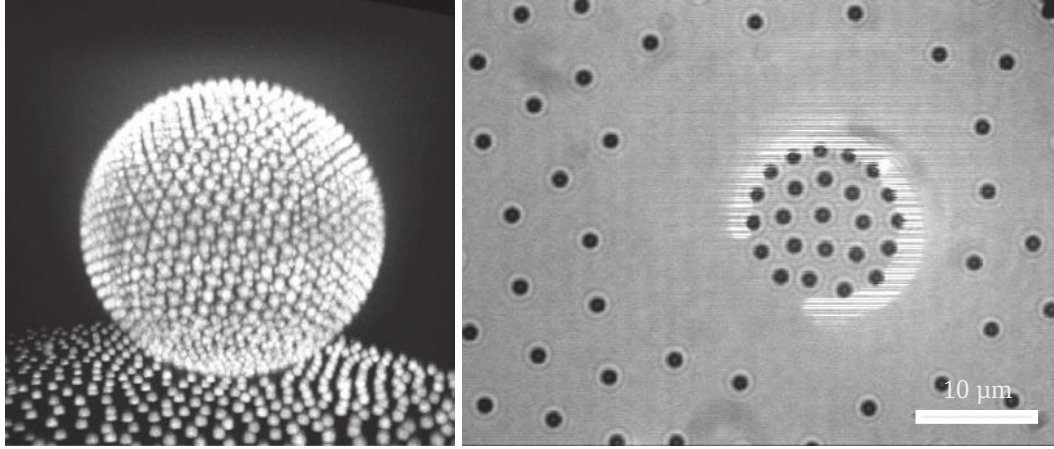


Figure 2.8 (lhs) A spherical crystal formed by self-assembled colloidal beads on a liquid droplet with a diameter of 60 μm images using confocal laser scanning microscopy. The colloids are placed on the droplet using optical tweezers. When a colloid is removed from the ball, the curved crystal self-heals through a collective rearrangement that re-distributed the density (adapted from Ref. [98]). (rhs) Optical microscope image of an optical wall is created using laser tweezers confining a small number of particles to build an isolated system (adapted from Ref. [99]).

The total amplitude of the electric field generated by the two laser beams in the x -direction can be written as

$$\begin{aligned} E(x) &= Ae^{(iK_{1,x}x)} + Ae^{(iK_{2,x}x)} \\ &= 2A \cos(K_{1,x}x), \end{aligned} \quad (2.43)$$

assuming that the beams can be described as planar waves and using $K_{1,x} = -K_{2,x}$ as shown in Eq. (2.42). The potential energy of the scattering (Eq. (2.38) and gradient (Eq. (2.41)) force scale with E , therefore the potential U_{el} in x direction can be written as:

$$U_{el}(x) \propto \cos^2 \left(|\mathbf{K}| \sin\left(\frac{\theta}{2}\right)x \right) \propto 1 + \cos \left(|2\mathbf{K}| \sin\left(\frac{\theta}{2}\right)x \right) \quad (2.44)$$

In Fig 2.11 the landscape of U_{el} is illustrated and compared with the intensity profile of an experimentally measured fringe pattern taken from Ref. [93]. In our analysis the beams were described as planar waves in contrast with the experimental setup, where the laser beams have a Gaussian profile. For a laser beam with a Gaussian profile, an extra term appears in Eq. (2.44):

$$U_{el}(x) \propto 1 + \cos \left(|2\mathbf{K}| \sin\left(\frac{\theta}{2}\right)x \right) e^{-2x^2 \cos^2(\theta/2)/R^2}, \quad (2.45)$$

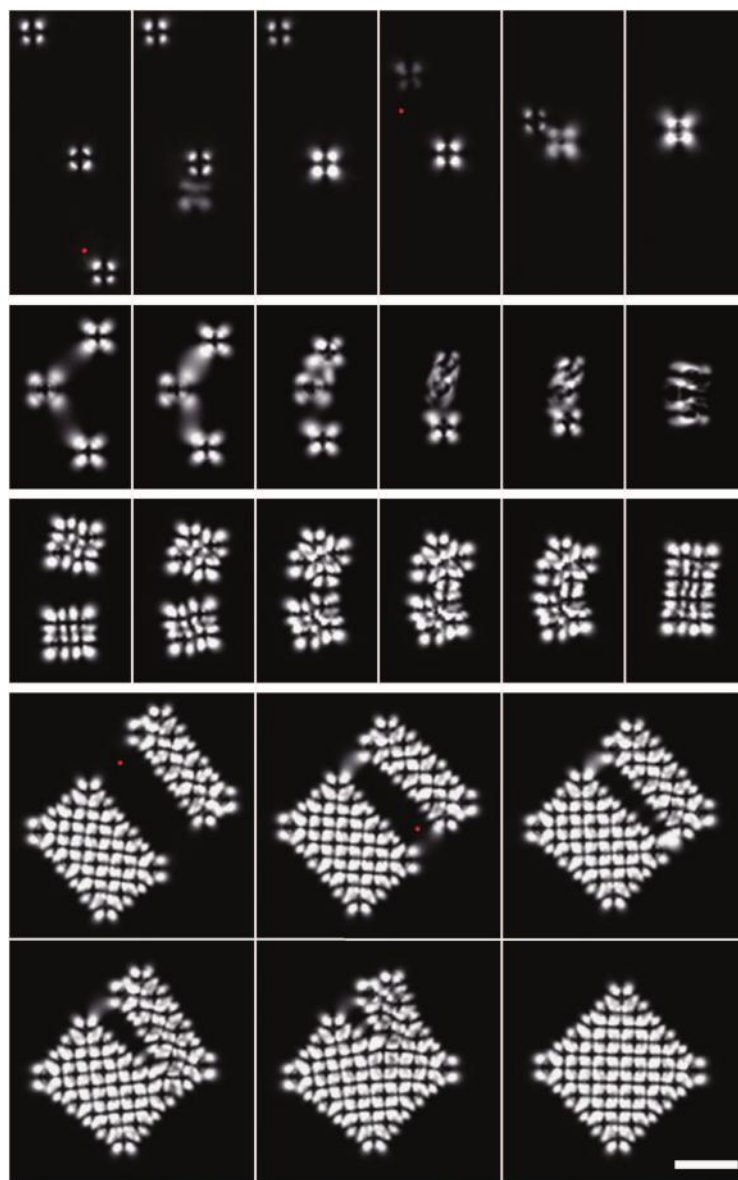


Figure 2.9 Optical-tweezer assembly of a 3D colloid crystal imaged using a fluorescent confocal polarizing microscopy set-up. Colloidal particles of $4\ \mu\text{m}$ thickness appear as bright objects with a dark cross in the centre. In the first row, one particle is brought closer to another until they spontaneously form a chain of two particles in the direction perpendicular to the plane of the image. The pair appears as a single colloid, only larger and brighter. In the subsequent images, chains of particles are brought close to each other until they form the final $6 \times 6 \times 3$ colloidal crystal. The scale is bar $10\ \mu\text{m}$ (adapted from Ref. [100]).

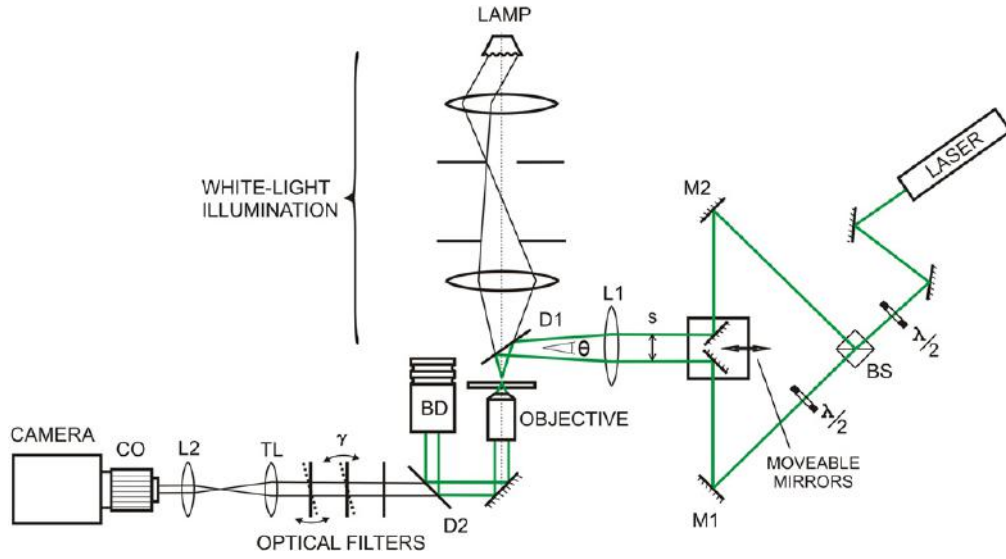


Figure 2.10 Schematic of an experimental arrangement used to generate a quasi-1D periodic potential. Two coherent laser beams are created at the beam-splitter (BS). Two movable mirrors M1 & M2 determine the beam separation at the focusing lens L1, and control the beam crossing angle θ . The LAMP and CAMERA setup are added in order to simultaneously image the sample (adapted from Ref. [93]).

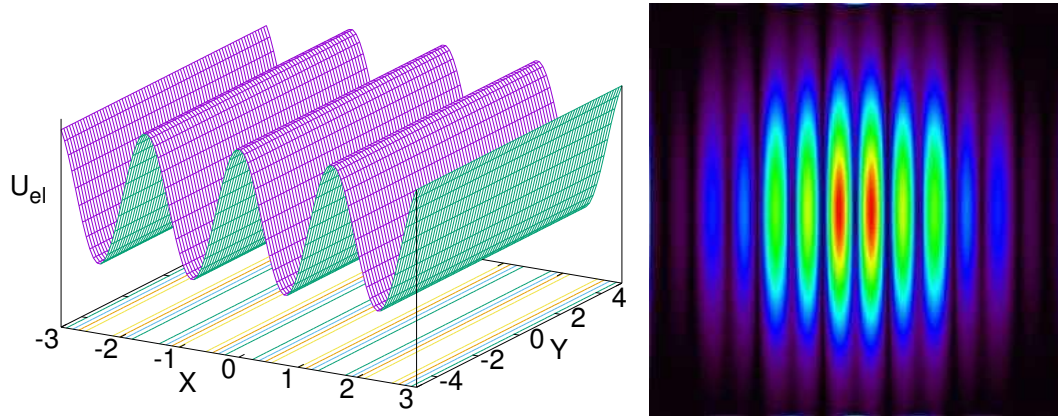


Figure 2.11 Quasi-1D periodic potential created by two interfering laser beams given by Eq. (2.44) (lhs) and experimentally measured fringe pattern [93] using the set-up given in Fig. 2.10 (rhs).

where R is the laser beam radius.

5 Molecular mechanics and reactive force fields

In chapters 5-6, molecular systems that mainly consist of water molecules and graphene layers are studied. In principle there is no reason to abandon the atomic approach that was used here in the previous sections. The chemical bonds that are present in molecular systems are simply inter-atomic potential energy terms [101]. Ideally, we should be able to treat all aspects of chemical bonding, including the reactions which form and break bonds, in a proper quantum mechanical fashion. Dealing with the motion of electrons is outside the scope of MD, and here different computational methods exist [102]. *Force field methods* (also known as molecular mechanics) are used to calculate the energy of a system as a function of the nuclear positions only. Different force field methods are being developed, most of which are designed for specific purposes [103–105]. Many of these force fields can be interpreted in a four-component picture of intra- and intermolecular forces in the system, which are illustrated in Fig. 2.12. The energetic costs associated with the deviation of bonds and

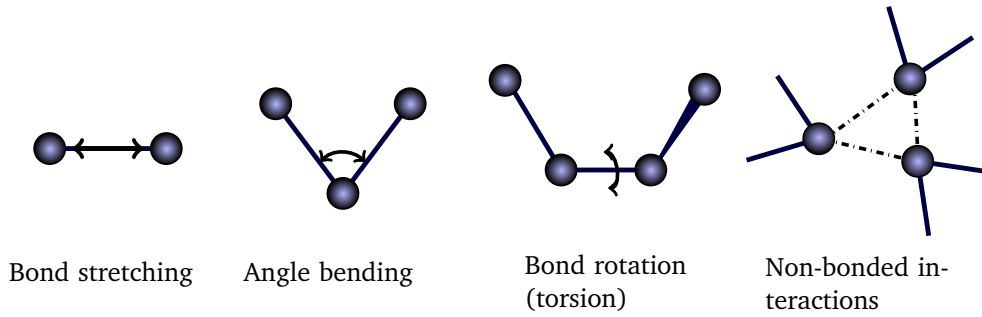


Figure 2.12 Schematic representation of four key contributions to a molecular mechanics force field: bond stretching, angle bending, torsion, and non-bonded interactions.

angles away from their equilibrium values are described by the force field. An elemental functional form that can be used to model molecules could be written down as

$$\begin{aligned}
 U(r) = & \sum_{bonds} \frac{k_i}{2} (l_i - l_{i,0})^2 + \sum_{angles} \frac{p_i}{2} (\theta_i - \theta_{i,0})^2 + \sum_{torsions} \frac{V_n}{2} (1 + \cos(n\omega - \gamma)) \\
 & + \sum_{i=1}^N \sum_{j=i+1}^N \left(4\epsilon_{ij} \left[\left(\frac{\sigma_{ij}}{r_{ij}} \right)^{12} - \left(\frac{\sigma_{ij}}{r_{ij}} \right)^6 \right] + \frac{q_i q_j}{4\pi\epsilon_0 r_{ij}} \right),
 \end{aligned} \tag{2.46}$$

where the first two harmonic terms express the energy contribution of bond and angle deviations from their respective reference values $l_{i,0}$ and $\theta_{i,0}$. The third term in Eq. (2.46) is a torsional potential that models how the energy changes as the bonds rotate. The multiplicity n is the value that gives the

number of minimum points in the function as the bond is rotated through 360° , and γ is the phase factor which determines where the torsion angle passes through its minimum value. Taking two sp^3 carbon atoms for example, the rotational profile could be represented by a single torsional term with $n = 3$ and $\gamma = 0^\circ$ giving minima at $\pm 60^\circ$ and 180° . A double bond between two sp^2 carbons atoms would have $n = 2$ and $\gamma = 180^\circ$ giving minima at 0° and 180° . The value of the coupling constant V_n would also be significantly larger for the double bond than for a single bond. In Fig. 2.13 the energy profile of this example is shown. The last term in the representative force field Eq. (2.46) is the non-bonded term. Here, the energy is calculated between all pairs of atoms i and j that are in different molecules using a Lennard-Jones potential for van der Waals interaction and a Coulomb term for additional electrostatic effects.

The simple force field that was presented in Eq. (2.46) already contains a multitude of coupling constants, namely two for each bond, two for each bond angle, and three for each torsion angle that a molecule in the system might have. The use of a harmonic potential for the bond length and bond angle is only the first order approximation. Terms in higher orders can be added (each with their own

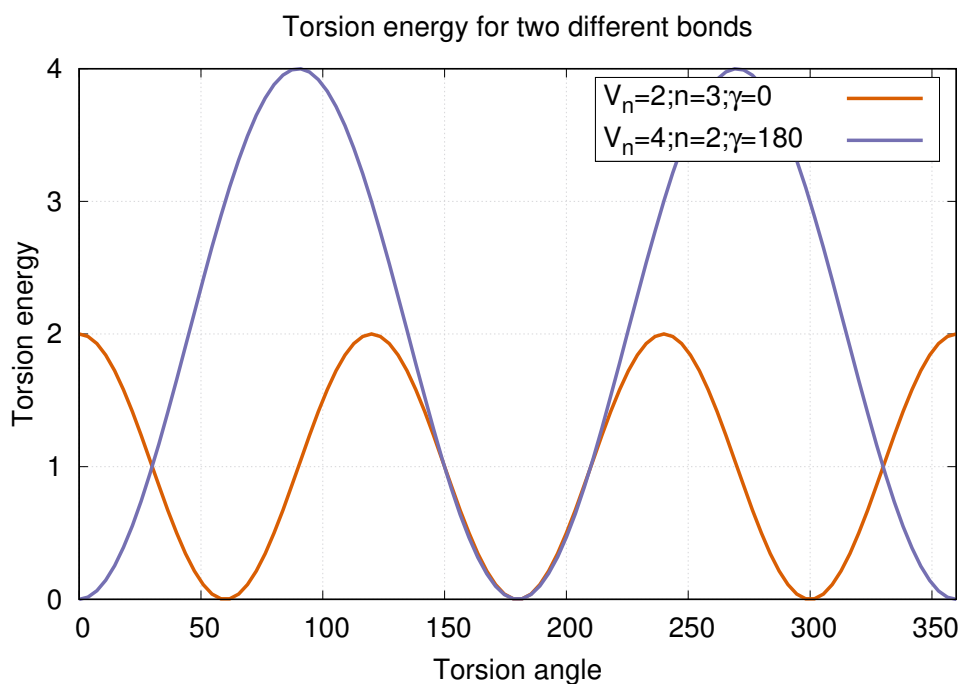


Figure 2.13 Torsional potential for the example of a single bond between two sp^3 carbon atoms (given by $V_n = 2; n = 3; \gamma = 0$) and a double bond between two sp^2 carbon atoms ($V_n = 4; n = 2; \gamma = 180$).

coupling constant) in order to resemble a Morse potential more closely. But more importantly, cross terms need to be introduced between the different terms. For example, as a bond angle is decreased it is found that the adjacent bonds stretch. One should in principle include cross terms between all these contributions in an efficient force field. The values of the different constants arising in this type of parametrisation need to be fitted against data obtained from different experimental or computational methods for each atom type. The atom type is not just the atomic number of an atom, it also needs to contain information about its possible hybridisation states. Taking carbon for example, the force field needs to distinguish a sp^3 hybridised atom (which forms a tetrahedral geometry), with sp^2 hybridised carbon (which are trigonal), and the linear sp hybridised carbon structure. So called *bond order potentials* can describe several different bonding states of an atom, using the same set of parameters.

It should be clear by now that force field methods are not easily constructed, and why different force fields are being developed parallel to each other, while dealing with the same physics. The force that was mainly used in this thesis when dealing with molecular systems was ReaxFF (reactive force field), which is a force field with bond ordered potentials developed at the California Institute of Technology [48]. At the start of each force calculation, the bond order of each atom is calculated using the inter-atomic distances:

$$BO_{ij} = \exp \left[p_{bo,1} \left(\frac{r_{ij}}{r_0^\sigma} \right)^{p_{bo,2}} \right] + \exp \left[p_{bo,3} \left(\frac{r_{ij}}{r_0^\pi} \right)^{p_{bo,4}} \right] + \exp \left[p_{bo,5} \left(\frac{r_{ij}}{r_0^{\pi\pi}} \right)^{p_{bo,6}} \right], \quad (2.47)$$

where constants $p_{bo,i}$ and r_0^i are parameters of the model depending on the atom types involved. In Fig. 2.14 different contributions to the bond order are visualised for covalent bonds.

Note that the value of BO_{ij} does not have to be an integer, fractional bond-orders indicate weakly bonded atoms. In ReaxFF, the coupling constants appearing in Eq. (2.46) are bond order dependent, ensuring that their energy contributions disappear upon bond dissociation. Similarly, non-bonded interactions are dependent on the bond order parameter of the molecules participating in the interaction. The hydrogen bond between a electronegative charged atom Z in the vicinity of a hydrogen atom (H), covalently bonded to X, is described in ReaxFF by:

$$E_{Hbond} = p_{hb,1} [1 - \exp(p_{hb,2} \cdot BO_{XH})] \exp \left[p_{hb,3} \left(\frac{r_0^{hb}}{r_{HZ}} + \frac{r_{HZ}}{r_0^{hb}} - 2 \right) \right] \sin^4 \left(\frac{\Theta_{XHZ}}{2} \right), \quad (2.48)$$

where $p_{hb,i}$ and r_0^{hb} are again parameters of the model depending on the atom types involved, BO_{XH} is the bond order term of the X-H molecule, and r_{HZ} gives the distance between hydrogen and the Z atom. The angle between the covalent bond from the X-H molecule and the hydrogen bond between H and Z is given by Θ_{XHZ} . For hydrogen bonding to be strong, it is critical that these three atoms

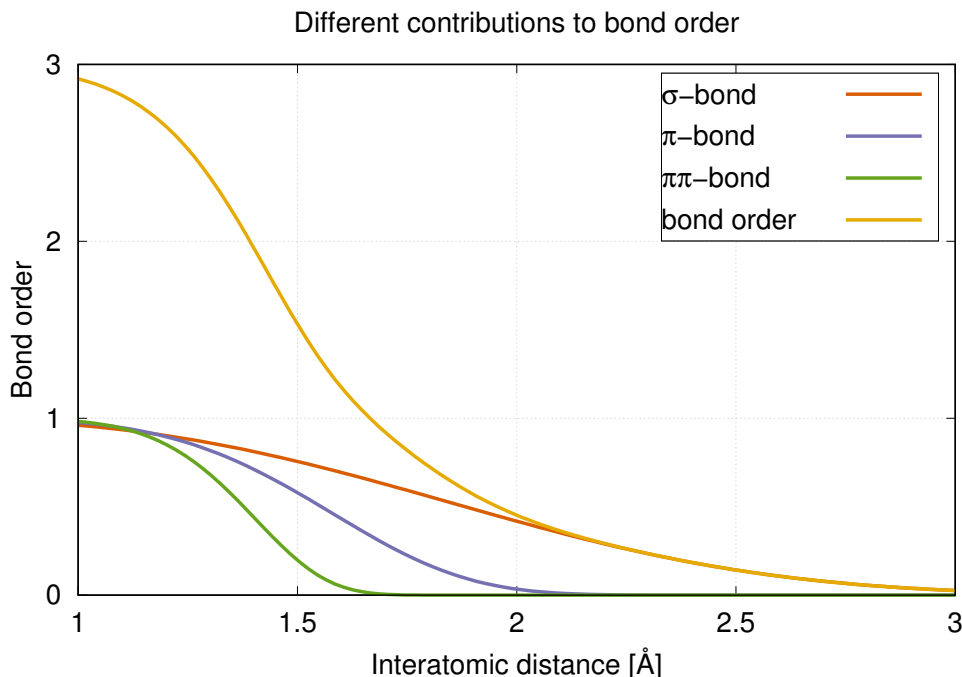


Figure 2.14 Example of the bond order dependence on the interaction distance for different covalent bonds.

are aligned on a straight line. This is expressed by the $\sin^4\left(\frac{\Theta_{XHZ}}{2}\right)$ term in Eq. (2.48), which is maximized when $\Theta_{XHZ} = \pi$.

Lastly, ReaxFF uses the bond order to calculate charge polarization within molecules using the Electronegativity Equalization Method (EEM) [106]. This method allows for the fast generation of atomic charges and molecular dipoles using a set of calibrated parameters and knowledge of the molecular structure.

6 LAMMPS

The molecular dynamics simulations presented in this work were performed using the Large-scale Atomic/Molecular Massively Parallel Simulator (LAMMPS) distribution developed by the Sandia National Laboratories [107]. LAMMPS is an open-source project that contains a large variety of functionality and is made to be easily extended by the user². Because of its versatility and parallel

²Although it forces the user to write low-level code, some of which is redundant. A brief list of the general classes and features can be found at <http://lammps.sandia.gov/features.html>

performance, LAMMPS is widely used in different research branches (e.g., solid mechanics, organic molecules & granular materials) for which independent community written modules are available. It has been used in the detailed simulation of a single molecule [108] up to systems containing billions of atoms [109].

6.1 Neighbour lists

LAMMPS uses spatial-decomposition techniques to partition the simulation domain over different processors. Each processor becomes responsible for one of these sub-domains, and can perform a large fraction of the computations independent of the processes running on the other CPU's. In Fig. 2.15, the three most used approaches to computing interactions is shown. The "all pairs" method is only efficient when the interaction range r_c is very small or very large with respect to the simulation region. As the amount of computations grow as $\mathcal{O}(N^2)$ only small systems can be studied. Two techniques for which the computational effort reduces to $\mathcal{O}(N)$ are used in tandem by LAMMPS. Cell subdivision is used to distribute the workload over different CPU's as outlined above [110]. Each subsystem uses neighbour lists [63] to keep track of nearby particles (exceeding the boundaries of the sub-domains) that are within the interaction range. Nearby particles are defined as the ones lying in the interaction range r_c or are nearing this territory by increasing the length for which a particle is included in the list with a value Δr_c .

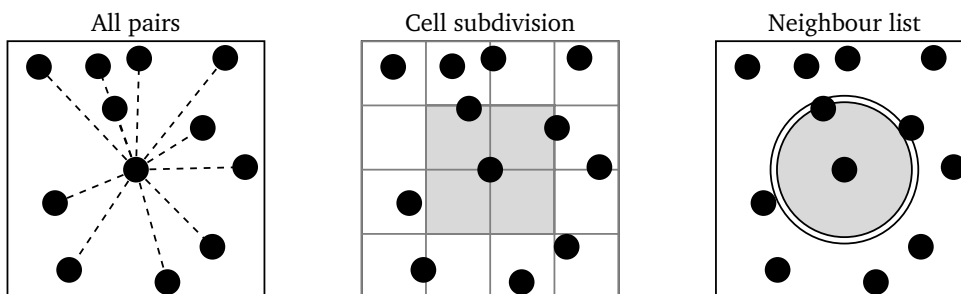


Figure 2.15 Illustration of the different approaches to constructing neighbour lists: all pairs, cell subdivisions and neighbour lists. The inner circle shows the interaction range, the outer circle depicts the extra range covered in the construction of the list.

The success of this approach is a consequence of the slowly changing environment during a typical simulation. As a consequence the neighbour list does not have to be rebuilt every time-step (otherwise it would hardly be more effective than looking at all pairs), but is refreshed when the

maximum velocities of particles in the system exceed the following criterion:

$$\sum_{time-steps} \left(\max_i |\mathbf{v}_i| \right) > \frac{\Delta r_c}{2\Delta t}. \quad (2.49)$$

For objects that are in the neighbour list, but outside of the sub-domain, each processor must store and communicate *ghost* atom information of particles that border each domain. In a parallel computing sense, LAMMPS is the most efficient for rectangular systems with an uniform particle density.

6.2 Periodic Boundary Conditions

The use of these ghost atoms in neighbour lists makes it possible to model infinitely large systems. Finite and infinite systems behave very differently, and the question of how large a system must be to resemble the behaviour of an infinite system lacks an unique answer. In order to be able to neglect the effect of the boundaries of the simulation domain, only a small fraction of the atoms should be affected by the boundaries of the domain. Consider, for example, a three dimensional system containing $N_m = 10^{21}$ equally spaced atoms, the number of atoms adjacent to the wall is of the order of $N^{2/3} = 10^{14}$, only one in each 10^7 particles. A more realistic example of a computational units cell is the simulation of 10^4 atoms, of which roughly 50% will be directly affected by the boundaries. If one were to study the typical behaviour of an interior atom, a better approach is needed. LAMMPS elegantly implements periodic boundaries, by also sharing translated ghost atoms between processors at the opposite boundary of the simulation domain. This is illustrated in Fig. 2.16 for the case of a single processor unit (indicated by the thick lines inside the figure). Particles at the boundary regions are added as ghost atoms at positions that lie outside of the original simulation domain when building neighbour lists and during the integration of the equations of motion.

6.3 Thermostatting

In the following chapters, a thermostat is used to perform simulated annealing: in order to find the global minimum energy structure of a large system, the system is initialized at a high temperature, and then is slowly relaxed until the desired temperature is obtained.

The temperature of a system is related to the time average of the kinetic energy, following the equipartition theorem:

$$\langle H_{kin} \rangle = \frac{D_N}{2} N k_B T, \quad (2.50)$$

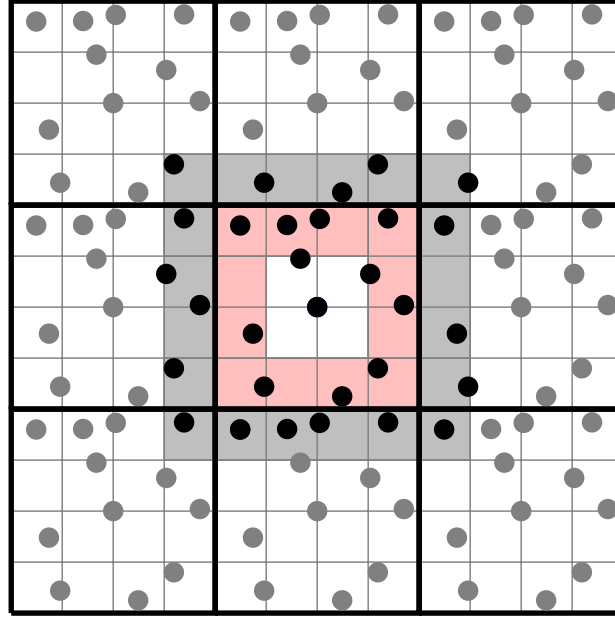


Figure 2.16 Implementation of periodic boundary conditions in 2D: particles at the boundary region (in red) are added as ghost atoms at positions outside of the simulation box (grey area). The width of the boundary region depends on the interaction length.

where D_N is the number of degrees of freedom, and N the number of particles. An obvious way to alter the temperature of the system is to scale velocities by a factor λ [111]:

$$\begin{aligned}\Delta T &= \frac{1}{2} \sum_{i=1}^N \frac{2}{D_N} \frac{m_i (\lambda v_i)^2}{N k_B} - \frac{1}{2} \sum_{i=1}^N \frac{2}{D_N} \frac{m_i v_i^2}{N k_B} \\ \Delta T &= (\lambda^2 - 1) T_{curr} \\ \lambda &= \sqrt{T_{new}/T_{curr}},\end{aligned}\tag{2.51}$$

where T_{curr} is the current temperature, and T_{new} the desired temperature after the velocities have been scaled. An alternative way to write down the scaling factor λ is to couple the system to an external heat bath that remains fixed at the desired temperature [112]. The heat bath acts as a source of thermal energy, supplying or removing heat from the system when it is necessary. The velocities are scaled so that the rate of change of temperature is proportional to the temperature difference between the system and the heat bath:

$$\frac{\partial T(t)}{\partial t} = \frac{1}{\tau} (T_{bath} - T(t)),\tag{2.52}$$

τ is a coupling parameter that determines how fast the bath and the system conduct thermal energy. For a finite time-step Eq. (2.52) becomes

$$\Delta T = \frac{\Delta t}{\tau} (T_{bath} - T(t)), \quad (2.53)$$

so that the scaling factor can be written down as

$$\lambda^2 = 1 + \frac{\Delta t}{\tau} \left(\frac{T_{bath}}{T(t)} - 1 \right) \quad (2.54)$$

For large τ , the coupling is weak and the system will slowly adjust itself to the heat bath. When the coupling parameter equals the time-step, then this algorithm is equivalent to the simple rescaling in Eq. (2.51). A constant of ≈ 100 time-steps is considered good practice [55].

6.4 Barostatting

In the same spirit as the scaling of velocities to control the temperature of the system, a barostat maintains or alters the pressure by changing the volume of the simulation domain. The amount of volume fluctuation is related to the isothermal compressibility κ :

$$\kappa = -\frac{1}{V} \left(\frac{\partial V}{\partial P} \right)_T \quad (2.55)$$

Methods used for pressure control are analogous to those used for temperature. The system is coupled to a *pressure bath* [112] for which the rate of change is given by:

$$\frac{\partial P(t)}{\partial t} = \frac{1}{\tau_p} (P_{bath} - P(t)). \quad (2.56)$$

Here, τ_p is the coupling parameter that determines how quickly the exchange in pressure takes place. The volume of the simulation box is rescaled with a factor λ

$$\lambda = 1 - \kappa \frac{\Delta t}{\tau_p} (P - P_{bath}), \quad (2.57)$$

which results in, for a three-dimensional system, that the coordinates are scaled by a factor $\lambda^{1/3}$:

$$\mathbf{r}'_i = \lambda^{1/3} \mathbf{r}_i. \quad (2.58)$$

6.5 Nosé-Hoover

The thermostat and barostat which were described above are extremely efficient in relaxing a system to a target temperature and pressure. But once the system reached equilibrium, it might be more important to probe the system in a correct canonical ensemble by considering the heat bath as an integral part of the system. This approach, which was originally developed by Nosé and later improved by Hoover [113, 114], extends the Hamiltonian H of the initial system with two artificial terms:

$$H_{NH} = H + \frac{p_s^2}{2Q} + k_B T (3N + 1) \ln s, \quad (2.59)$$

for which s takes the form of the "position" of the heat reservoir, p_s its "momentum", and Q its "mass". The constant N that appears on the rhs of Eq. (2.59) is the number of momentum degrees of freedom of the original system. The physical significance of these variables is not really evident at this point. The choice of their form is motivated on how they can transform the micro-canonical partition function. One can show that the micro-canonical partition function of the extended Hamiltonian (including the heat bath's degrees of freedom) returns the canonical ensemble of the original system. Equations of motion can be developed for this extended Hamiltonian system where a value must be chosen for the "mass" Q , which is important in determining the rate of energy exchange with the imaginary heat bath. For a detailed discussion, the reader is referred to [78].

Part II

Self-assembly of Janus particles

CHAPTER 3

Self-assembly of Janus particles confined in a channel

Colloidal particles, larger than molecules but small enough to undergo Brownian motion, are known to assemble into clusters as a result of non-covalent interactions [115]. Janus particles present an important class of building blocks for directional assembly, where the orientation of each colloid places a central role in the formation of clusters. As was discussed in Sec. 1.2 these are colloids whose surfaces is divided into two areas of different chemical composition. In this chapter, we consider a two-dimensional model of Janus discs consisting of a hydrophobic semicircle and an electro-negatively charged one. When placed in a solution, the hydrophobic sides will attract each other while the charged sides will give rise to a repulsive force.

Using molecular dynamics simulations, we study the morphology of these particles when confined in a channel-like environment using a one dimensional harmonic confinement potential. This type of potential can be experimentally achieved by letting two tilted lasers interfere on the sample, as was shown in Sec. 4.5. The interest to this system is first of all due to the fact that it could serve as a simple model for membrane formation. Indeed, the recently synthesised new class of artificial amphiphiles, known as Janus dendrimers, were shown to self-assemble in bilayer structures mimicking biological membranes. In turn, Janus particles that combine the amphiphilicity and colloidal rigidity serve as a good model for Janus dendrimers. A variety of ordered membrane-like morphologies are found consisting of single and multiple chain configurations with different orientations of the particles with respect to each other that will be summarized in a phase diagram.

This chapter is organized as follows. In subsequent Sec. 1 a small introduction is given outlining some of the features of directional assembly and general concept that were further discussed in Sec. 1.2. In Sec. 2 the underlying model is given, combining the hydrophobic effect which was previously discussed in Sec. 4.2 with the DLVO potential for charged surfaces (which was given in Sec. 4.3) into a single pair potential that describes the Janus particle dynamics. Sec. 2 is devoted to the numerical results of the molecular dynamics simulations. We start by determining the equilibrium configurations of the system, followed by the proposal of a classification scheme that will be used to construct a phase diagram. Finally the conclusions are given in Sec. 5. Part of this chapter has been published in Ref. [116].

1 Introduction

Fabrication of ordered arrays of nano-particles is of significance for both fundamental science associated with low-dimensional physics and applications. Up-to-date lithography is the major technique in generating arrays. This technique is fairly expensive, complicated and time-consuming. As an alternative route to this top-down approach is a bottom-up self-assembly. Mono-disperse spheres of sub-micron size can readily self-assemble into highly ordered and close-packed arrays, so-called colloidal crystals [117]. Most of these early studies were restricted to isotropic interactions and therefore the possible structures that can be realized were limited. Recently, patchy colloidal particles have attracted a large amount of interest. These are colloids that have an anisotropic inter-particle interaction. Different experimental techniques are available to locally modify the chemical composition and the shape of colloidal particles [118–121]. These local modifications are called patches, and depending on the number, size and the chemical properties of each patch these colloids exhibit extraordinary diffusive properties [122, 123] or can be used as building blocks for complex structures [124–126]. The substantial research effort in preparing these nano-particles is driven by their potential applications in nano-electronics [127], drug delivery [128, 129], liquid optics [30, 130], separation of mixtures [131], etc. For molecular amphiphiles, such as phospholipids, soaps, and many block copolymers, the segregation of their polar and nonpolar groups plays a central role in the creation of soft materials. Living cells, mayonnaise, and fracturing fluids used in oil recovery are representative examples where molecular amphiphiles play an important role [132]. Similarly, Janus particles (which are several orders of magnitude larger) assemble into clusters owing to directional non-covalent interactions. Although the level of commonality between these two fields is unknown, the *molecular mimetic* self-assembly of anisotropic colloidal particles are known to act like surfactant molecules, and segregate strongly to liquid interfaces, stabilizing emulsions and foams [133]. Particles can stabilize emulsions in two ways: they can absorb the oil-water interface and remain forming a film around the drops impeding coalescence, and additional stabilisation occurs when the particle-particle interactions are such that a three-dimensional network of particles develop around the droplet [134]. In Figure 3.1 this stabilization of biphasic systems consisting of two immiscible fluids (such as air/water, oil/water) is shown. In Fig. 3.1(A) the oil-in-water or water-in-oil stabilization is shown as a function of the contact angle $\theta_{o/w}$. This angle is directly related to the hydrophobicity of the colloid [135]:

$$-\Delta E = \pi\sigma^2\gamma_{o/w}(1 \pm \cos\theta_{o/w})^2, \quad (3.1)$$

in which $\gamma_{o/w}$ is the surface tension and ΔE is the required energy to remove a particle of radius σ from the interface. The sign of $\cos\theta_{o/w}$ is negative for removal into the water phase, and positive for removal into the air or oil phase. The range is ΔE is much higher for colloids than for surfactant

molecules, and as a consequence colloids can be thought of as irreversibly absorbed in liquid interface, which is marked in contrast to surfactant molecules which can adsorb and desorb [136]. For hydrophobic particles, $\theta_{o/w}$ is smaller than 90° , hydrophilic particles have $\theta_{o/w} > 90^\circ$ so the larger fraction of particles prefers to reside in water, which forces the particle monolayer to curve to oil and leads to oil-in-water emulsions which is shown in Fig. 3.1(B). In subsequent Fig. 3.1(C) sedimentation is shown as a result solid surfactants, and in Fig. 3.1(D) a high resolution image of a stabilizing cluster of colloids of $0.9 \mu\text{m}$ in diameter is shown where the pore space between colloids is measured to be $0.15 \mu\text{m}$.

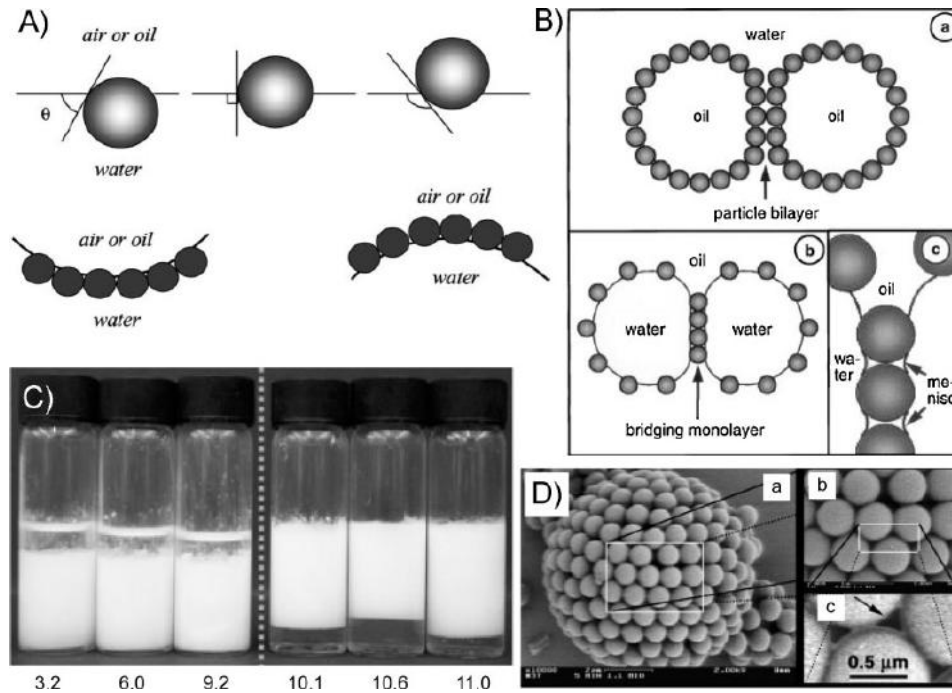


Figure 3.1 (A) Upper panel: position of colloidal particles at an oil–water interface for different contact angles $\theta_{o/w} < 90^\circ$ (left), $\theta_{o/w} = 90^\circ$ (centre), and $\theta_{o/w} > 90^\circ$ (right). Lower panel: corresponding positioning of particles at a curved interface (adapted from Ref. [135]). (B) Emulsion stabilization by colloidal particles: steric stabilization (a), and bridging stabilization (b and c) (adapted from Ref. [137]). (C) Stabilization or sedimentation of emulsions affected by either a change in pH value or salt concentration using the JPs we considered here. Emulsions (white) are of water-in-oil at $\text{pH} \leq 9.5$ (left) and undergo sedimentation to liberate a clear oil phase above, and are of oil-in-water at $\text{pH} \geq 10.0$ (right) which cream with a clear aqueous phase separating below them (adapted from Ref. [136]). (D) Low (a) and high magnification (b and c) scanning electron microscopy (SEM) images of a $10 \mu\text{m}$ in diameter cluster of colloids composed of $0.9 \mu\text{m}$ diameter PS spheres. In (c) the pore space between neighbouring colloids is measured to be $0.15 \mu\text{m}$ (adapted from Ref. [138]).

In our work, we model Janus spheres by two-dimensional discs that consist of two semicircles: a hydrophobic side, and an electro-negatively charged one. The fabrication of these colloidal spheres has been achieved several years ago by depositing a mono-layer of octadecanethiol (ODT) on polystyrene spheres with a thin film of gold on one hemisphere [139]. When these particles are placed in a solution, the octadecanethiol polymer ionizes and will form an electrical double layer around one hemisphere. Only at relative short inter-particle distance (with respect to the particle size), the hydrophobic sides will attract each other, while the electrostatic repulsion will repel the particles at a larger length scale (which is defined by the Bjerrum length of the system). In experiment, the repulsive length scale can be dynamically controlled by adjusting the ionic strength of the solution (which can be easily tuned by changing the salt concentration of the solution), and different assembled structures can be expected. For low ionic strength, the kinetics will be dominated by electrostatic interactions: colloids will repel each other regardless of their relative orientation. By increasing the ionic strength of the solution, the screening length of the repulsion can become smaller than the diameter of the colloidal sphere. In this regime the orientation of each colloid becomes of importance. For each value of the ionic strength, there is a value of the angle for which the (total) inter-particle force switches from attractive to repulsive [139], which is shown in Fig. 3.5. The phase diagram and dynamic properties of Janus particles consisting of a single hydrophobic patch have been studied previously in great detail [140, 141]. How their properties are modified when such particles are confined in a channel-like environment is not yet known. The interest to this system is first of all due to the fact that it could serve as a simple model for membrane formation. Recently a new class of artificial amphiphiles was synthesized, known as Janus dendrimers [142]. These are molecular superstructures (with a typical size of ± 100 nm) terminated by different functionalities. In turn, Janus particles that combine the amphiphilicity and colloidal rigidity serve as a good model for Janus dendrimers. Therefore, we analyse here the morphologies of Janus discs in a two-dimensional (2D) plane, that are trapped in a one dimensional harmonic potential. We investigate the interplay between the strength of the inter-particle interaction, the strength of the 1D confinement and the density of the particles. Using this system we study the dynamics of Janus particles in a quasi-one-dimensional environment by means of molecular dynamics simulations.

2 Janus particle dynamics

We focus on a system of *soft discs* in a two dimensional plane. Each disc consists of two semicircles, one being hydrophobic and the other side being negatively charged. Because of the different chemical composition between these two regions, the interaction potential between two JP's depends not only on the separation between these two but also on their relative orientation. A mathematical model

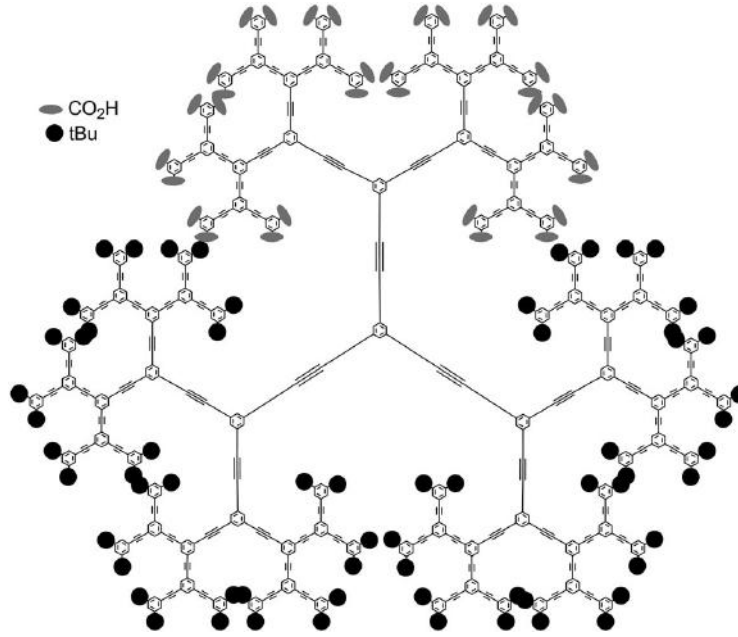


Figure 3.2 Example of a rigid Janus dendrimer with carboxylic acids on one side and tert-butyl groups on the other side (adapted from [143]).

describing the duality characteristics of a fluid of Janus particles has been proposed by Kern & Frenkel in Ref. [144] which considered a fluid of rigid colloids with one attractive patch covering half the sphere. It has been successful in reproducing the thermodynamical and structural properties of these colloids found in experiments [139, 140, 145]. In the *sticky limit*, where the attractive patch is represented by a square well infinitely deep and infinitesimally wide, analytical solutions have been proposed [146, 147]. Different variations of the model have been reported, where the size of the patch [148] and number of patches [149] have been altered. Here, we will propose a new variation of the model, expanding it to incorporate two patches of different chemistry, namely one hydrophobic and one electro-negatively charged semicircle.

The total pair potential between two discs placed at positions \mathbf{r}_1 and \mathbf{r}_2 can be written down in two distinct parts, an isotropic term representing the soft-disc repulsion and an angular dependent factor characterizing the patchy structure of the colloids,

$$\phi(r_{12}, \hat{u}_1, \hat{u}_2) = \phi^S(r_{12}) + \phi^I(r_{12}, \hat{u}_1, \hat{u}_2). \quad (3.2)$$

where $r_{12} = |\mathbf{r}_1 - \mathbf{r}_2|$ and \hat{u}_i is polar axes indicating the centre of the hydrophobic patch. As a simple

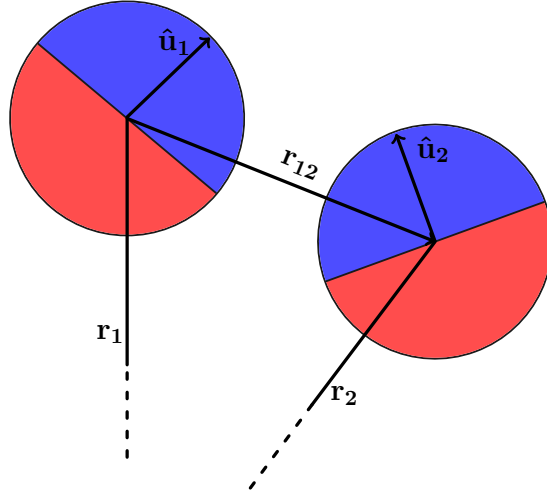


Figure 3.3 Configuration of two Janus discs. The polar axes \hat{u}_1 and \hat{u}_2 indicate the centre of the hydrophobic patch.

model for soft-disc repulsion, we use an elastic repulsion between two overlapping discs [81]:

$$\begin{cases} \phi^S(r_{12}) = \frac{\varepsilon}{2}(2\sigma - r_{12})^2, & r_{12} < 2\sigma \\ \phi^S(r_{12}) = 0, & r_{12} > 2\sigma, \end{cases} \quad (3.3)$$

where ε characterises the flexibility of the discs, and σ being the disc's radius. An elastic repulsion [81, 141, 150] is preferred over the hard wall potential proposed by the Kern-Frenkel model [144]. This will facilitate the usage of MD simulations, while still having the possibility of tuning the potential so that particles can hardly overlap. The anisotropic contribution ϕ^I depends on the relative orientation between two particles which is indicated by the polar vectors \hat{u}_1 and \hat{u}_2 (see Fig. 3.3). Two patches interact only if the line joining the centres of the two particles intercepts the patch on surface of one particle and the patch on the surface of the other particle. The pair-potential is separated as followed:

$$\begin{cases} \phi_{HF}^I(r_{12}, \hat{u}_1, \hat{u}_2) = -\frac{\kappa_H}{2}(2\sigma_H - r_{12})^2, & r_{12} < 2\sigma_H \wedge \hat{u}_1 \cdot \hat{r}_{12} \geq 0 \parallel \hat{u}_2 \cdot \hat{r}_{21} \geq 0 \\ \phi_{EL}^I(r_{12}, \hat{u}_1, \hat{u}_2) = Z_{eff}^2 \lambda_B \left(\frac{\exp(\kappa\sigma)}{1 + \kappa\sigma} \right)^2 \frac{\exp(-\kappa r_{12})}{r_{12}}, & \hat{u}_1 \cdot \hat{r}_{12} \leq 0 \wedge \hat{u}_2 \cdot \hat{r}_{21} \leq 0. \end{cases} \quad (3.4)$$

κ_H and σ_H are elastic parameters similar to the ones used in Eq. (3.3), they measure the strength and the range of the attraction. The electrostatic repulsion of colloids in a solution is governed by a screened Coulomb potential given by the DLVO [151] theory. Z_{eff} is the effective charge on the

surface of the colloidal particles, λ_B is the Bjerrum length, κ^{-1} is the Debye-Hückel screening length which depends on the solvent, and $\beta^{-1} = k_B T$ is the thermal energy of the system at temperature T with k_B the Boltzmann constant. The potential landscape is visualised on the left-hand side of Fig. 3.4.

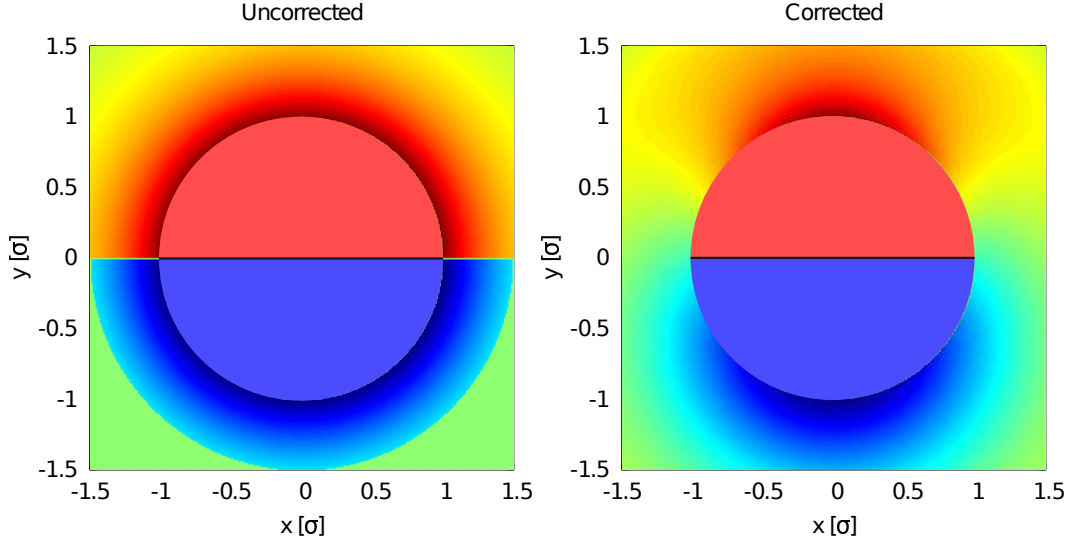


Figure 3.4 Janus potential indicated by red saturation for the repulsive DLVO potential, and blue colouration for the attractive hydrophobic effect. (lhs) Uncorrected Janus potential with discontinuous behaviour near the boundary of the two semicircles. (rhs) Corrected Janus potential with a continuous potential landscape.

3 Simulation technique and parametrization

The anisotropic pair potential ϕ^I that was defined in Eq. (3.4) has a discontinuous behaviour near the boundary of the two semicircles, resulting in divergent forces which makes this model unusable for dynamical calculations. The pair potentials that were defined in Sec. 2 are a consequence of the effective charge and hydrophobicity of the surfaces. When taking a mean-field approach of these surface interactions, they can be written down as the pair potential of a single point that is placed at $\pm \frac{\pi}{4\sigma} \hat{u}_i$ for the hydrophobic and electronegative patch respectively by taking the mean of a uniform function around a semicircle:

$$\frac{1}{2\sigma} \int_{-\sigma}^{\sigma} \sqrt{\sigma^2 - x^2} dx = \frac{1}{2\sigma} \int_0^{\pi} \sin^2 \theta d\theta = \frac{\pi}{4\sigma}. \quad (3.5)$$

Parameters are chosen such that particles can hardly interpenetrate, and that the electrostatic repulsion can be neglected when two charged patches are not in direct contact with each other. If the solvent has a weak ionic strength, the electrostatic repulsion is so severe that particles repel each other regardless of their relative orientation. This effect weakens strongly as soon as the Debye-Hückel screening length κ^{-1} becomes smaller than the particle size. The hydrophobic attraction, on the other hand, is believed to be insensitive to or only weakly dependent on ionic strength [86].

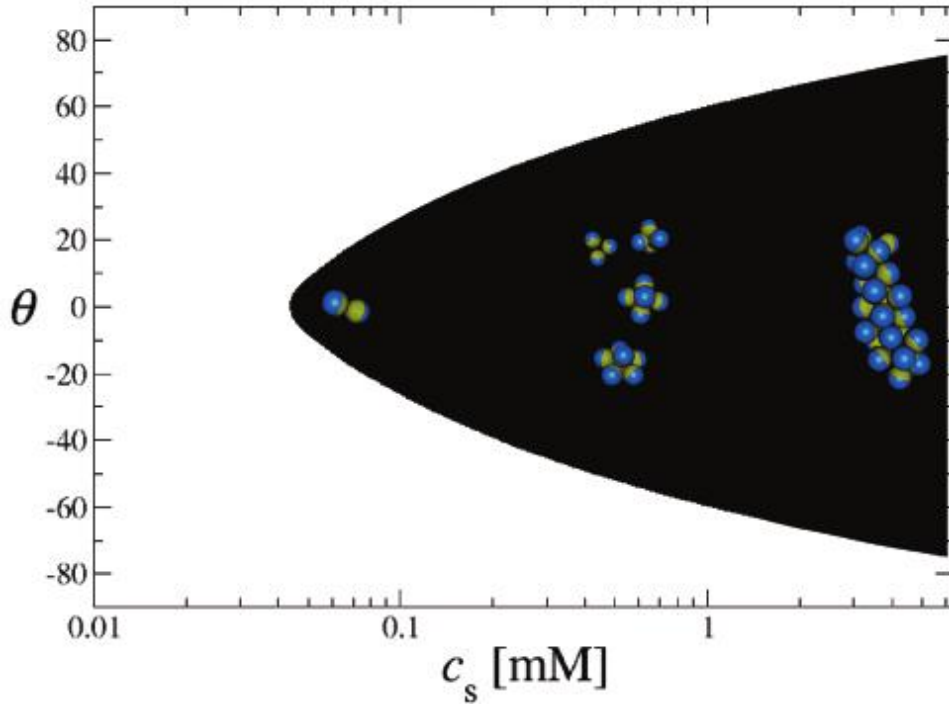


Figure 3.5 Region of permitted tilt angles between two charged hemispheres with $1\ \mu\text{m}$ diameter held at a centre-to-centre distance of 1.020 micrometers, plotted as a function of the logarithmic concentration of monovalent salt. The hydrophobic (charged) hemisphere are denoted by yellow (blue) colours. The boundary is determined by requiring the electrostatic energy cost per simultaneous rotation of the particles over an angle θ to be smaller than $k_B T$. The reference angle $\theta = 0$ refers to the situation where the hydrophobic hemispheres face one another (adapted from Ref. [139])

This effect is illustrated in Fig. 3.5, where the allowed angles are given between two particles in near-proximity. The higher the ionic strength, the greater the range of allowed angles for which particle orientations become energetically stable, allowing for more complex clusters to be formed.

With this parametrisation in mind, the anisotropic force field around the colloid can be written down by taking the sum of the two contributions ϕ_{HF}^I and ϕ_{EL}^I that were introduced in Eq. (3.4):

$$\phi^I(\mathbf{r}_{12}, \hat{u}_1, \hat{u}_2) = \phi_{HF}^I\left(\left|\mathbf{r}_{12} + \frac{\pi}{2\sigma}(\hat{u}_1 + \hat{u}_2)\right|\right) + \phi_{EL}^I\left(\left|\mathbf{r}_{12} - \frac{\pi}{2\sigma}(\hat{u}_1 + \hat{u}_2)\right|\right), \quad (3.6)$$

which is shown on the right-hand side of Fig. 3.4. The resulting pair potential can be considered as two patches of high intensity in a region $\pi/2$ around the polar vector \hat{u}_i , which gradually decays as it nears the boundary between the two patches. This smooth interpolation between the two different chemistries results in a continuous potential making it applicable in MD simulations.

Because the origin of force is now offset from the centre of the colloid, a torque can be defined on the colloidal particles:

$$\tau_i = \pm \frac{\pi}{4\sigma} \hat{u}_i \times \mathbf{F}_i \left(\mathbf{r}_{12} \pm \frac{\pi}{2\sigma} (\hat{u}_1 + \hat{u}_2) \right). \quad (3.7)$$

where again the polar axes $+\hat{u}_i$ indicates a hydrophobic patches, and $-\hat{u}_i$ the centre of a charged surface. Lastly, a hydrophobic patch will also be attracted by a negative charged surface. This is taking into account by expanding Eq. (3.6) with an extra term:

$$\frac{1}{2} \phi_{HF}^I \left(\left| \mathbf{r}_{12} + \frac{\pi}{2\sigma} \pm (\hat{u}_1 - \hat{u}_2) \right| \right) \quad (3.8)$$

where the added fraction $\frac{1}{2}$ denotes a weakened hydrophobic effect between these two patches. In Fig. 3.6 a summary is shown of the different interactions that are incorporated in this model. Hydrophobic patches will be attracted to nearby colloids, regardless of their orientation, and the centre of the half circle will be attracted to the centre of the neighbouring particle, minimizing the exposure of the hydrophobic surface to the solution. Two charged surfaces, on the other hand, will be repelled and will be pivoted away from their interaction centre.

Molecular dynamics were performed using LAMMPS (see Sec. 6) by extending its library with a new atom style to incorporate the JP interaction scheme that was outlined above. Two dimensional molecular dynamics simulations were performed using a computational unit cell of 100-400 particles confined in a one-dimensional parabolic potential $V(y) = \frac{1}{2}Ky^2$ and periodic boundary conditions in the perpendicular direction were applied, forcing the colloids in a quasi one-dimensional state. In this work, the strength of the parabolic potential will not be altered as its sole purpose is to localize particles in the centre of the trap. The motion of the Janus particles was studied using the Verlet algorithm which was introduced in Sec. 3. A thermostat is applied to the system, which controls the translational and rotational diffusivity coefficients of the colloids. The parameters of the pair potentials are given in table 3.1, where 1 aN (attonewton) equals 10^{-18} N = 1 pg μ m/s². Taking the

ϕ^S		ϕ_{HF}^I		ϕ_{EL}^I		
$\varepsilon[aN/\mu m]$	$\sigma[\mu m]$	$\kappa_H[aN/\mu m]$	$\sigma_H[\mu m]$	$Z_{eff}[e]$	$\kappa^{-1}[\mu m]$	$\lambda_B[\mu m]$
8	1	2	1.5	0.32	0.2	0.01

Table 3.1 Parameters for the pair potentials that were defined in Eqs. (3.3-3.4).

mass of the polystyrene colloidal sphere to be of the order of 1 *pg*. The size of the harmonic constant of the external potential is taken as 0.2 *aN/μm*, and the used timestep is given by $\Delta t = 0.05s$.

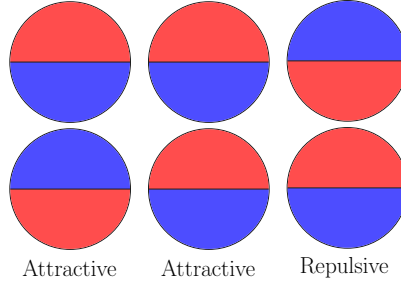


Figure 3.6 Different configurations of adjoining Janus particles in a solution using the parametrisation outlined in Sec. 3: The anisotropic potential ϕ^I (see Eq. (3.4)) has an attractive contribution if a hydrophobic patch is involved in the interaction. If charged patches faces each other, the colloids will repel each other.

4 Numerical results

As a starting point in the determination of the equilibrium configurations and resulting phase diagram we aim to determine the minimum harmonic trap constant K for which aggregation occurs on a large scale, as we are not interested in micelle formation inside the quasi-one-dimensional channel. Our aim is to focus on the aggregation behaviour of the system depending on the packing fraction

$$\eta = N_{part}\pi\sigma^2/L^2, \quad (3.9)$$

where N_{part} is the number of particles in a square simulation box with length L . Depending on the packing fraction and external potential, a wide variety of morphologies can be found (see Fig. 3.7). The largest one-dimensional periodic structure in the trap is an aligned chain where all particles

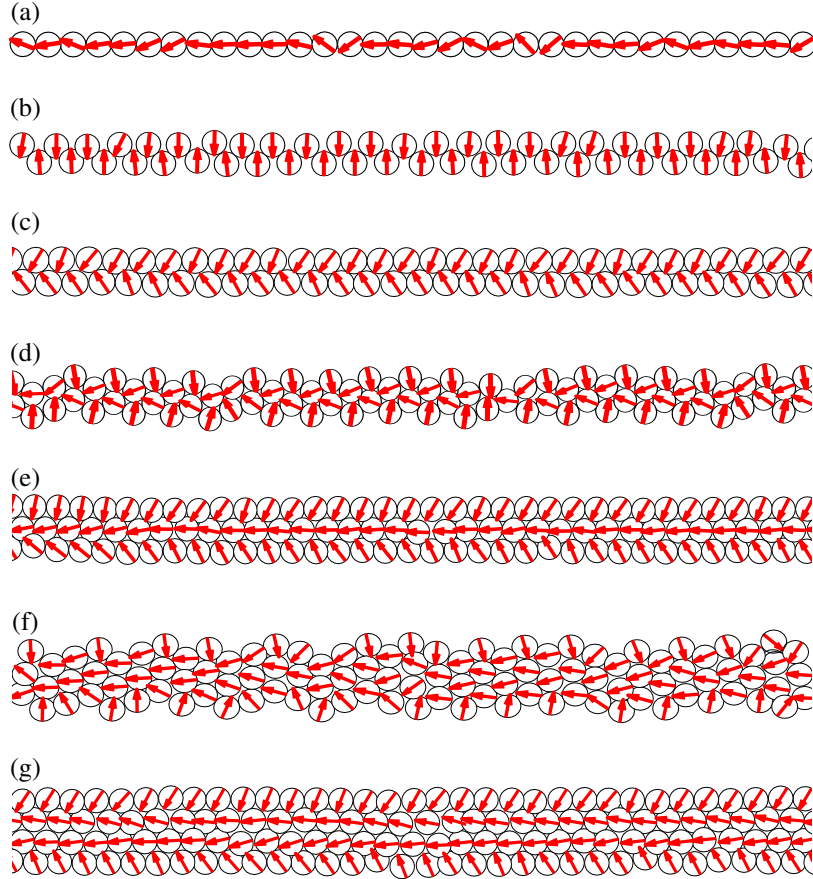


Figure 3.7 Different particle morphologies of Janus particles in a quasi-one-dimensional parabolic confinement potential found with molecular dynamics simulations, depending on the packing fraction η and the strength of the transverse trap potential $K\sigma$: (a) oriented chain ($\eta = 0.008, K\sigma = 0.5$), (b) zig-zag 1-chain ($\eta = 0.019, K\sigma = 0.5$), (c) oriented 2-chain ($\eta = 0.031, K\sigma = 0.2$), (d) zig-zag 2-chain ($\eta = 0.042, K\sigma = 0.2$), (e) oriented 3-chain ($\eta = 0.070, K\sigma = 0.2$), (f) zig-zag 3-chain ($\eta = 0.092, K\sigma = 0.2$), (g) oriented 4-chain ($\eta = 0.128, K\sigma = 0.2$). The particle orientation is represented by an arrow pointing toward the hydrophobic patch.

are orientated in the same direction, effectively nullifying the repulsive patch (Fig. 3.7(a)). When increasing η , it becomes impossible for all the particles to stay in the centre of the trap, which results in a zig-zag transition to a membrane structure (Fig. 3.7(b)), driven by the minimisation of the transverse trap potential. When further increasing the packing fraction we find a succession of close-packed oriented chains, and zig-zag variants. Each of the found stable structures succeeds in cancelling out the Coulomb repulsion at small particle distances.

4.1 Correlation functions

For molecular fluids it is convenient to introduce several types of distribution functions, correlation functions and related quantities in order to quantify different states. Once, for example, the total correlation function $g(r^h, \hat{u}^h)$ for a given system is known, thermodynamic properties of the system can be obtained [152]. To study the equilibrium properties of a general potential, the pair correlation function $g(12) = g(r_{12}, \hat{u}_1, \hat{u}_2)$ gives complete information about pairs of molecules [152]. We consider the spherical harmonic coefficients $g_{l_1 l_2 l}(r_{12})$ of $g(12)$ to highlight particular aspects of the function $g(12)$. The different morphologies are characterized by their density g_{000} and angular pair correlation functions g_{110} :

$$g_{000}(r) = \frac{L}{2\pi r N} \sum_i \sum_{j \neq i} \delta(r - r_{ij}), \quad (3.10)$$

$$g_{110}(r) = \frac{L}{2\pi r N} \sum_i \sum_{j \neq i} \delta(r - r_{ij}) \hat{u}_1 \cdot \hat{u}_2 \quad (3.11)$$

The density correlation function Eq. (3.10) is used to characterize the density profile of the structure, the angular pair correlation function Eq. (3.11) represents the relative orientation of two particles inside the cluster. Positive values of $g_{110}(r, \hat{u}_1, \hat{u}_2)$ represent an average parallel orientation between two particles, while a negative value expresses an anti-parallel orientation.

Each structure can be characterized by the pair correlation functions, Eq. (3.10) and Eq. (3.11), discussed previously. In Fig. 3.8 the characteristic correlation functions are shown for different temperatures for three values of packing fraction η : $\eta = 0.019$ (zig-zag 1-chain or membrane), $\eta = 0.042$ (zig-zag 2-chain), and $\eta = 0.070$ (oriented 3-chain) which correspond to cases (b), (d) and (e) in Fig. 3.7. When increasing temperature and thus the mobility of particles in the cluster, the complex gradually loses its positional and orientational order, until the thermal forces become larger than the Janus-particle interactions which dismantles the structure. The oscillating character of the correlation functions is due to: (i) the periodicity of the structure and (ii) orientational interactions. The zig-zag 2-chain and oriented 3-chain (cases (d) and (e) in Fig. 3.7) are similar in terms of density correlations. The difference is that the latter is more ordered since the structure contains more chains (three vs. two for (d)). For the zig-zag 1-chain or membrane (case (b) in Fig. 3.7) we find two

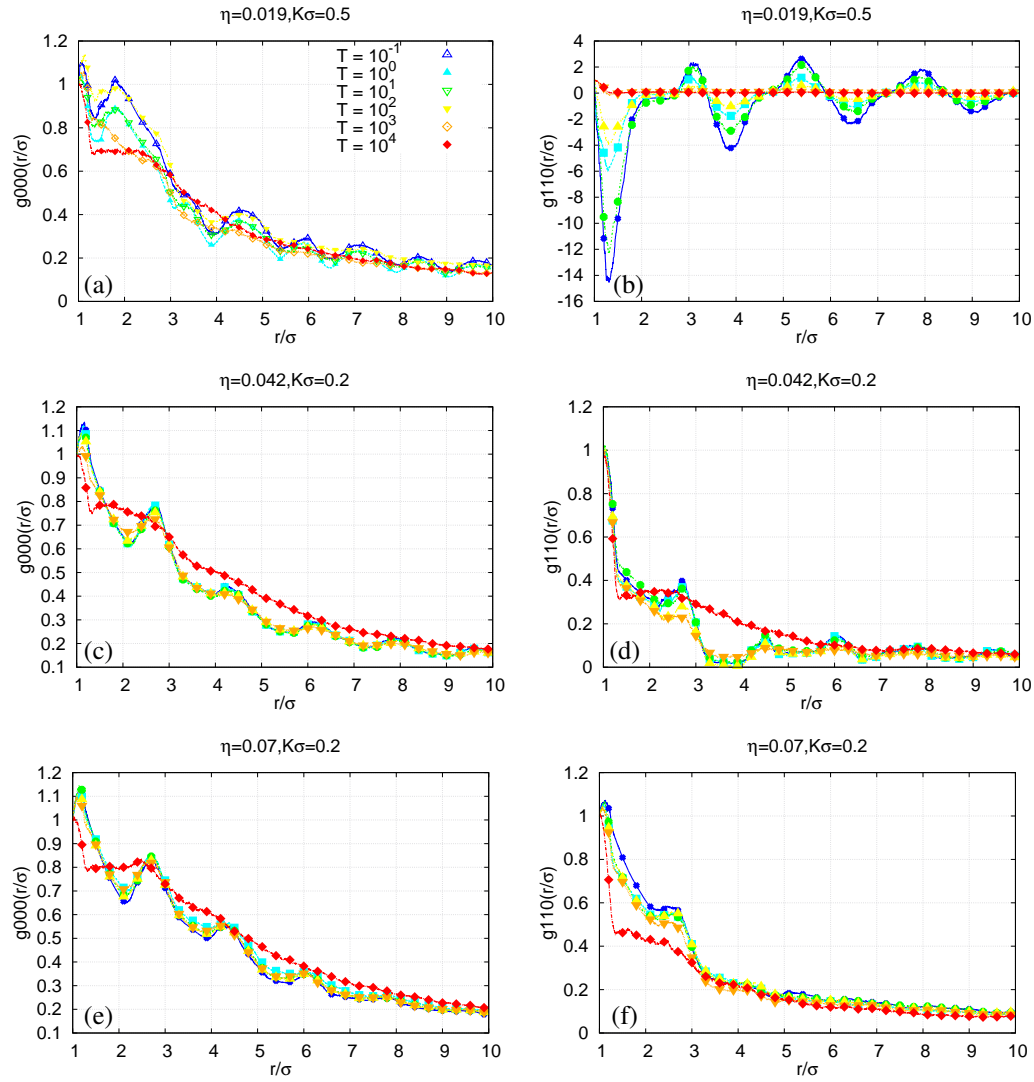


Figure 3.8 Correlation functions g_{000} and g_{110} for characteristic morphologies at $T = 10^{-1}, 10^0, 10^1, 10^2, 10^3$, and 10^4 (shown by symbols as indicated in (a)) for: membrane (a-b), zig-zag 2-chain (c,d) and oriented 3-chains (e,f). The density profile and angular pair correlation give a quantitative description of each morphology, and are used to construct a phase diagram. Each function is normalized at $r/\sigma = 1$.

periodicities for the nearest neighbours: one between particles in the same chain ($r/\sigma = 2$), and one between particles from different chains ($r/\sigma = 1$). Therefore the oscillations in the density correlation function ((a) in Fig. 3.8) have two harmonics. The orientational pair correlation function, on the other hand, loses its oscillating characteristic when increasing the density, as the particles in the cluster consist of stripes with different orientations. The particles in the outer chains of the cluster are oriented like in a membrane, i.e., with the hydrophobic sides inside, while the particles inside the cluster form oriented chains, assuring that no charged half-discs come in close contact with one another (see Figs. 3.7(d-g)). Apart from losing its periodic structure, we find that the overall magnitude of g_{110} increases for higher η . Again, referring to Fig. (3.7), in (b) we have a fully antisymmetric, anti-ferromagnetic (AF)-type, orientation. This property is clearly shown in Fig. 3.8 (b): on average, the orientational correlation is zero since the positive and negative contributions cancel each other. Increasing the density results in the formation of oriented chains inside the cluster (Figs. 3.7(d-g)), which causes a monotonic rise in the values of g_{110} .

4.2 Phase diagram

To construct a phase diagram, we need to compose a set of *order parameters* for each structure. A possible approach in achieving this is by defining a set of local pair correlation parameters for each structure:

$$\Gamma_{000} = \int_{\sigma}^{3\sigma} g_{000}(r) dr, \quad (3.12)$$

$$\Gamma_{110} = \int_{\sigma}^{3\sigma} g_{110}(r) dr, \quad (3.13)$$

which measures the structural order in the direct vicinity of each particle.

For the reference structures the local pair correlation parameters are calculated and plotted in Fig. 3.9 for $T = 0.1$. Each intermediate state consists of different areas, where one part of the system is in reference state A, while another part is in state B. For a broad range of values of parameter η , the functions Γ_{000} and Γ_{110} both exhibit a gradual increase (i.e., a linear increase followed by saturation) when increasing η , except for small values of η where the function Γ_{110} takes values in the vicinity of zero and then shows a sharp drop. This drop in Γ_{110} at $\eta \approx 0.01$ corresponds to the transition between the oriented chain (Fig. 3.7(a)) and zig-zag 1-chain (Fig. 3.7(b)). The observed behaviour is explained as follows: when increasing the packing fraction, the number of neighbouring particles for each colloid increases, and thus the value of Γ_{000} increases as well. The linear increase in Γ_{000} (for $\eta = 0$ to 0.02) corresponds to 1-chain and zig-zag 1-chain configurations, when adding new particles results in the linear growth of the number of neighbours for each particle. The value $\eta \approx 0.02$ corresponds to the formation of a 2-chain configuration, i.e., the appearance of the hexagonal order.

For further increasing η , new particles form additional layers but the hexagonal order remains thus leading to the saturation in Γ_{000} . Similarly, the function Γ_{110} gradually increases (for $\eta > 0.01$) since the number of inner (co-oriented) chains grows. The sharp drop in Γ_{110} at $\eta \approx 0.01$ is due to the chain-to-zig-zag transition when the nearest-neighbouring particles are oppositely oriented (AF ordering). Adding new inner chains with increasing η gradually destroys the AF ordering of the outer chains leading to the above gradual increase in the function Γ_{110} . Note that the function Γ_{110} also shows a linear and saturating trends. The former is the signature of the orientational order of the “all surface” particles (for one or two chains) while the latter is related to the formation of the inner layers where all the particles are co-oriented. A phase diagram in the η - K plane is presented in

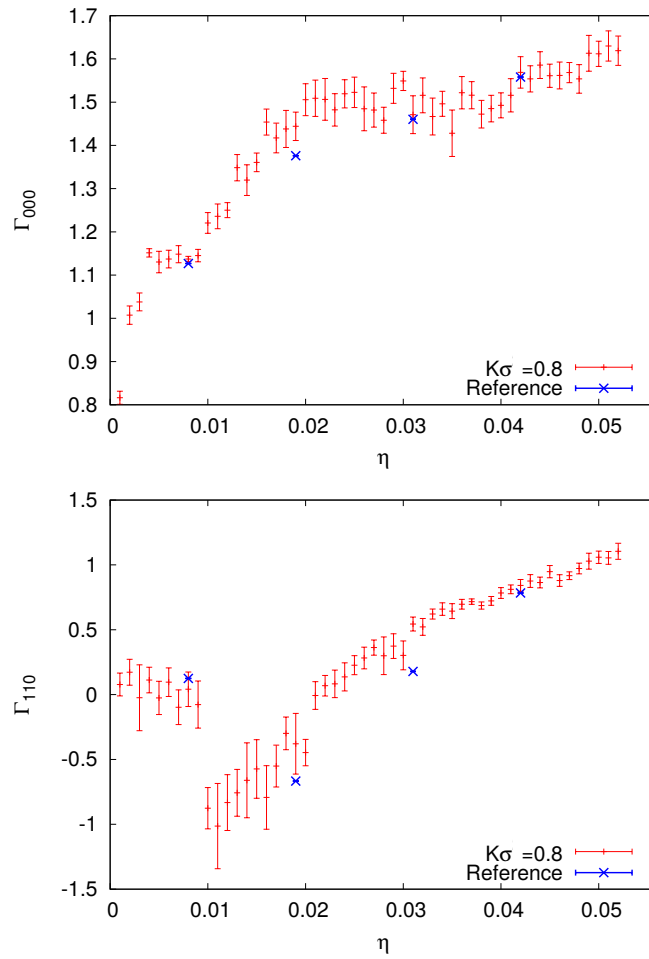


Figure 3.9 Progression of local pair correlation parameters Γ_{000} and Γ_{110} for the reference structures displayed in Fig. 3.7 and intermediate states for a fixed value of the external potential ($K\sigma = 0.8$).

Fig. 3.10. The different states and transitions can be visualised by assigning a colour to each state

depending on the value of Γ_{000} and Γ_{110} . No new phase jumps are present, only gradual transitions between different morphologies (except for the sharp transition between the oriented chain (green) and the zig-zag 1-chain (blue)). The reason for this is two-fold: local density fluctuations (which are more profoundly visible at low K) make it possible for the system to be at the same time locally in state A (e.g., zig-zag 1-chain) and B (e.g. oriented 2-chain), and there is a certain degree of freedom in which two morphologies can interchange. We find that the most decisive factor in determining a morphology is the packing fraction η , whereas each state is stable for a large interval of K -values. For $\eta < 0.007$ the oriented 1-chain is the most stable morphology, except for very low confinement strength. Here the hydrophobic attractive strength is larger than the trap potential, resulting in the formation of a membrane. For $\eta > 0.007$ it becomes impossible for all the particles to occupy the centre of the trap, and different morphologies abruptly arise. For low K an oriented 2-chain can easily be formed, while for higher trapping potential the particles get squeezed into a membrane structure. When increasing the density even further, the membrane gradually evolves into a close packed membrane with horizontal orientation, a state which we previously labelled as an oriented 2-chain. Increasing the density even further limits the diversity in possible structures, resulting in a succession of the most tightly packed structures: 2/3-chain and zig-zag variants, with crossover states in between.

5 Discussion and conclusions

We have studied a modified Kern-Frenkel model for soft-discs on a two dimensional plane using molecular dynamics simulations. Each disc consists of a charged semicircle, and one being hydrophobic. The electrostatic repulsion between colloids in solution takes the form of a screened-Coulomb potential given by the DLVO theory. For a solvent where the Debye-Hückel screening length is smaller than the particle size, the Janus nature of the colloids becomes profound and a wide range of morphologies were found. These differ in shape and orientational order, which were identified by their density and angular pair correlation footprint. These distinctive features can be used to label each state, and construct a η - K phase diagram. Apart from the abrupt transition between 1D and quasi-1D states, we find smooth crossovers between different morphologies, where increasing the transverse trap potential aids the formation of close-packed and highly-ordered states. The Janus particles considered in this work have been already fabricated [139] and we believe that the straightforwardness of the model and its rich phase behaviour begs for experimental verifications.

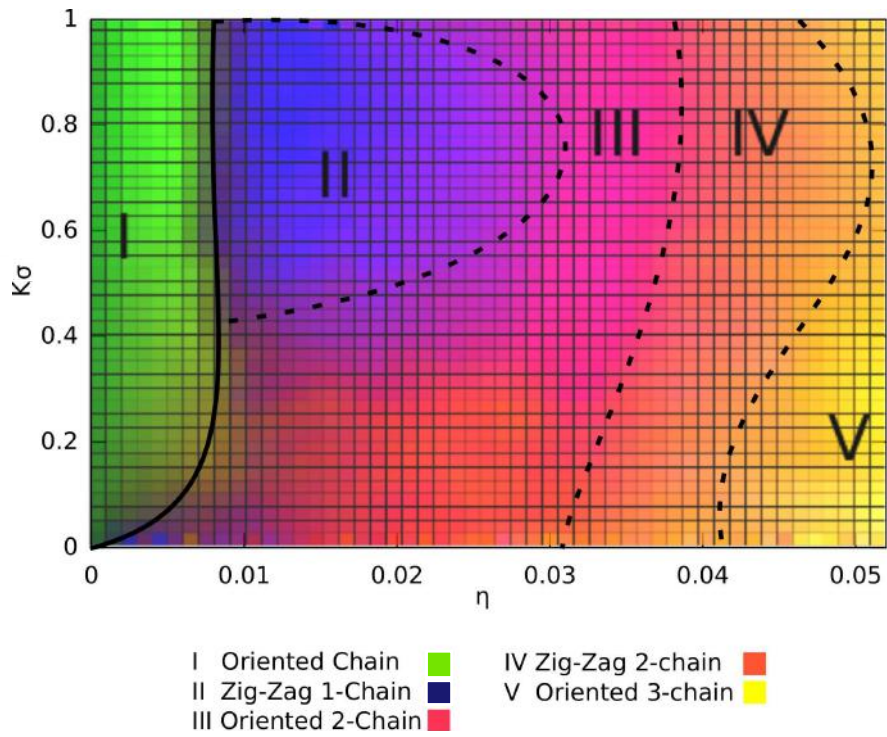


Figure 3.10 Phase diagram of the different structures formed by Janus discs in a harmonic trap for various values of the packing fraction η and confinement strength K . Each pure state is represented by a given colour: oriented chain (phase I) by green, zig-zag 1-chain (phase II) by blue, oriented 2-chain (phase III) by magenta, zig-zag 2-chain (phase IV) by orange, and oriented 3-chain (phase V) by yellow; mixed (intermediate) states are shown by colour gradients. The abrupt transition between oriented chain and zig-zag 1-chain/oriented 2-chain is shown by a solid line, while smooth transitions are (approximately) indicated by dashed lines.

CHAPTER 4

Self-assembly of Janus particles into helices with tunable pitch

In this chapter we wish to describe the level of commonality between amphiphilic Janus particles and peptide amphiphiles (PAs) by studying the level in which JPs can form helical superstructures. Accordingly, we analyse various superstructures of Janus spheres that are confined in a narrow channel. This is achieved numerically by placing them in a 3D box and applying a circular symmetric harmonic trap. Using this system we investigate the self-assembly dynamics of Janus particles in a quasi-one-dimensional channel environment by extending the 2D Janus model that was introduced in Chap. 3 to form a representation of three-dimensional Janus spheres. A variety of ordered membrane-like morphologies are found consisting of single and multiple connected chain configurations. For example, the system can be prepared so that the colloids form modified Boerdijk-Coxeter (B-C) helices [153, 154], an assembly of regular tetrahedra in a twisted fashion with the colloids placed on the vertices. The packing of spheres into a B-C helix is closely related to the study of close-packed conformations in biomolecules [155]. Our assembly strategy to obtain these helical structures is the interplay between interactions of different length-scales [156]. Competing interactions play a role in protein folding [157], and other polymeric macromolecules. For example, DNA is a polymeric macromolecule that can form a double helix as a result of the interplay between van der Waals and hydrophobic forces [158]. Using Janus colloids in a solution, we show that it is possible to manipulate the helicity of the super-molecule by screening the electrostatic interaction. This approach has been used by adding an electrolyte to the solution (such as NaCl [119]).

The chapter is organized as follows. In subsequent section the relation between molecular amphiphiles and helical structures is discussed. These clusters have been extensively studied for their structural diversity, with broad applications in tissue engineering, drug delivery and bacterial inhibition. For which some examples are given. In Sec. 2 we discuss the expansion of the JP model that was introduced in 2, design rules for the formation of helical structures, simulation method and used parameters. Sec. 3 is devoted to the numerical results of the molecular dynamics simulations. We start by determining equilibrium configurations of the system in subsection 3.1, followed by subsection 3.2 discussing the controllability of the helix pitch by changing the interaction length. Special attention is given to the observed Bernard spines in subsection 3.3. Finally, our conclusions are given in Sec. 4. Results presented in this chapter have been published in Ref. [159].

1 Introduction

Particle clusters, an intermediate level of matter between building blocks (atoms, molecules, colloids) and bulk phases are found throughout nature and technology: during the nucleation of bulk phases [160, 161], formation of nano-particles [162], protein aggregation in biology [163, 164], et al. Where onset of cluster formation resulting from isotropic interactions are well studied [165, 166], it is more challenging to understand the mechanisms between cluster formation in the case of non-covalent directional interactions [133, 167]. As shown in the previous Chapter, the comparison between colloidal particles and molecular amphiphiles with respect to their behaviour in mixtures is well known. In this chapter however, we will shift our attention to the kinetics and structures of clusters of JPs composed of a hydrophobic and charged hemisphere. Molecular amphiphiles are known to self-assemble into helical structures.

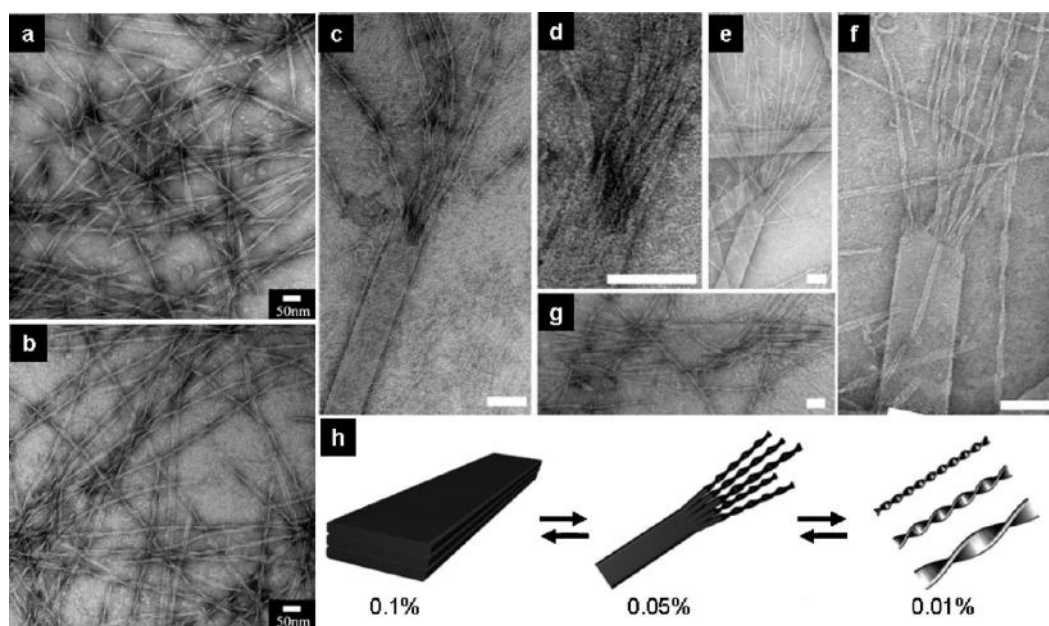


Figure 4.1 TEM images of nanobelts assembled from a peptide amphiphile composed of a polar negatively charged peptide and a hydrophilic valine face. At low pH, the glutamate faces are well protonated, and form a layered structure which are called multi-layered nanobelts. (a,b) At high pH, the deprotonation of the glutamate groups leads to a dissociation of the nanobelt, so that narrow nanobelts and twisted nanoribbons are observed. In (c-g) intermediate states are shown for the gradual transition of the flat nanobelt into twisted nanoribbons. The scale bars of panels (c-g) equals 100 nm. (h) Schematic representation of the morphological transitions with a change in salt concentration (adapted from [168]).

Different functional helical structures can be obtained by the self-assembly of peptide sequences containing hydrophobic and charged residues [169]. Here, the hydrophobic groups residues contribute to structural stability, while the charged residues are considered responsible for structural specificity of the targeted structures [170]. In Fig. 4.1 and example is shown where the ionic strength of the solution determines the morphology of the structures. When increasing the number of ions in the solution, helical structures are formed. These structures have been intensively studied for their self-assembly abilities, and structural diversity with broad applications in tissue engineering [171], drug delivery [172], regenerative medicine [173] and bacterial inhibition [174, 175]. A description

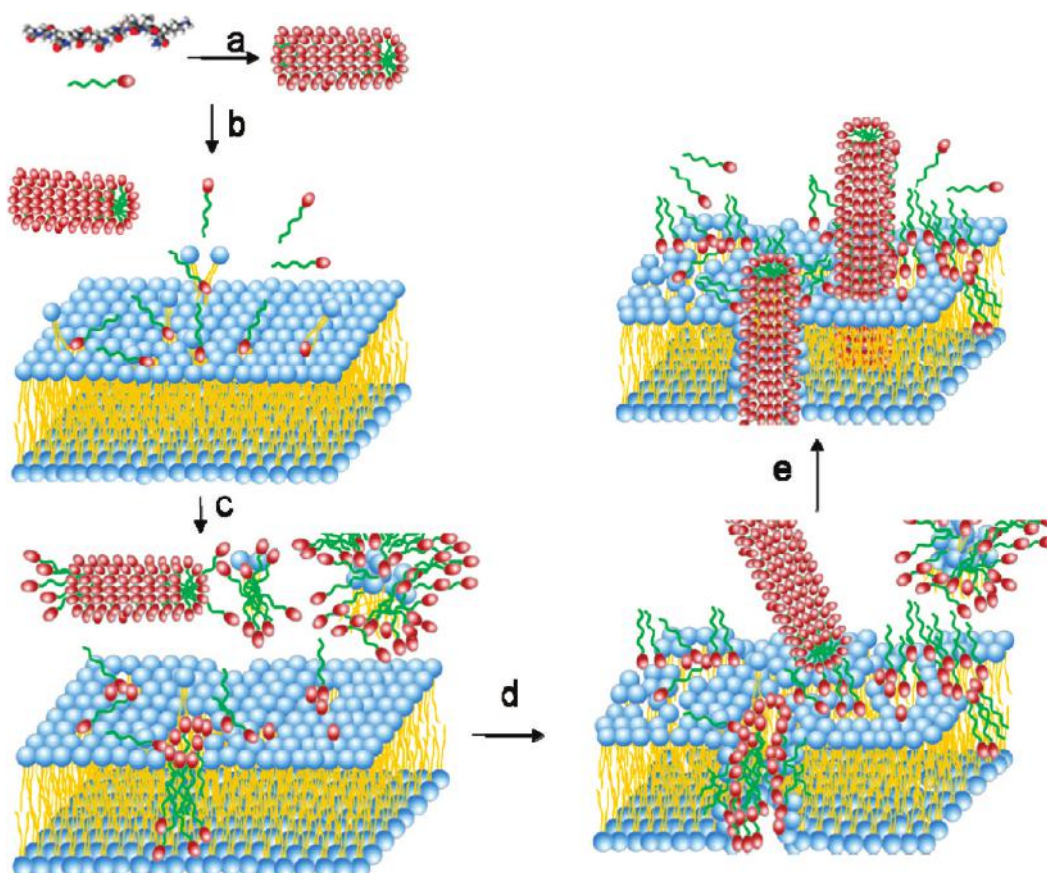


Figure 4.2 Schematic illustrations of actions of a PA leading toward bacterial membrane permeation and disruption. (a) PA molecules self-assemble into nanorods with the charged peptide (red) at the outside the rod. (b) These molecules may attach to outer membrane surface through charge interaction and may become inserted in the membrane through hydrophobic effects causing them to flip and insert into the inner leaf of the membrane (c) and disrupt the membrane causing leakage or lysis. (d) Nanorods might also associate with the cell membrane surface directly (e) become inserted in the membrane (adapted from Ref. [174]).

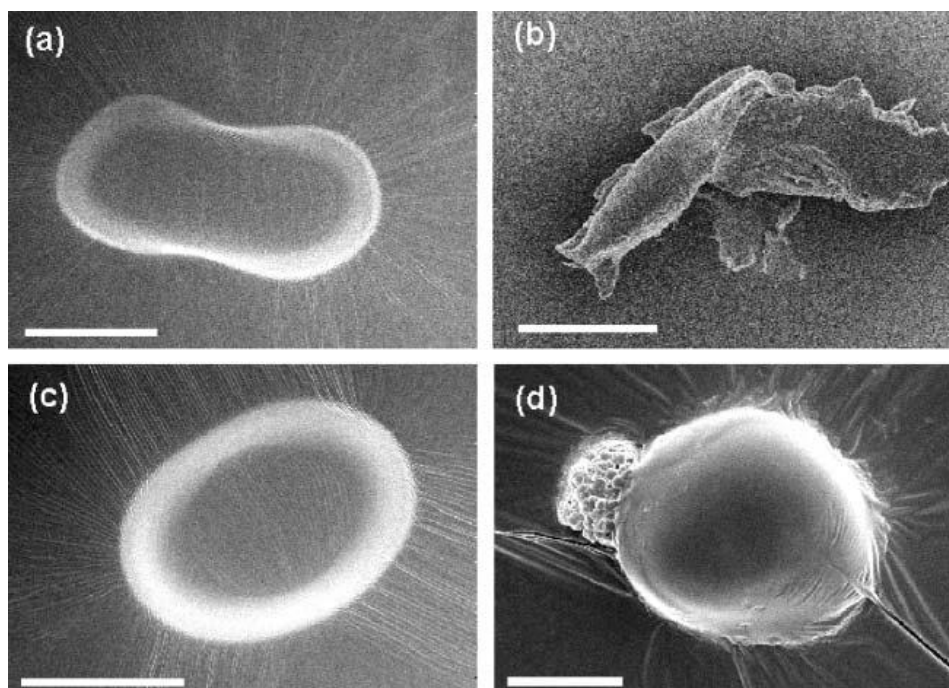


Figure 4.3 Scanning electron microscopy (SEM) images of the disruption of the cell membrane of *E. coli* (a-b) and *S. aureus* (c-d). The LHS (RHS) of the figure shows an image of the bacteria before (after) treatment with PAs. The scale bar in left hand corners equals $0.5 \mu\text{m}$ (adapted from [175]).

of the disruption of these types of peptide amphiphiles on a bacterial cell membrane is illustrated in Fig. 4.2, where in Fig. 4.3 scanning electron microscopy images show the collapse of the cell wall of *E. coli* and *S. aureus* bacteria. Finally, in Fig. 4.4 the use of these helical structures as a means for drug delivery is shown. Here, some of the charged peptides are replaced with therapeutic agents. When these nanorods come in contact with the cell membrane, they can dissolve (as was shown in Fig. 4.2), causing these agents to be released in close proximity to the targeted cell.

Interested in the similarity between PA's and amphiphilic Janus particles, we wish to study the effects of environment induced structural changes of colloidal clusters. In [176] Granick and coworkers, JPs were found to self-assemble in Boerdijk-Coxeter (B-C) helices at high particle concentrations. A BC helix is a helical assembly of regular tetrahedra, arranged so that the edges of the complex form three intertwined chains with non-trivial translation or rotational symmetry, which will be further discussed in Sec. 3.3. In Fig. 4.5 their experimental result is shown: by increasing the salt concentration large helical clusters are formed consisting of dual and triple helices.

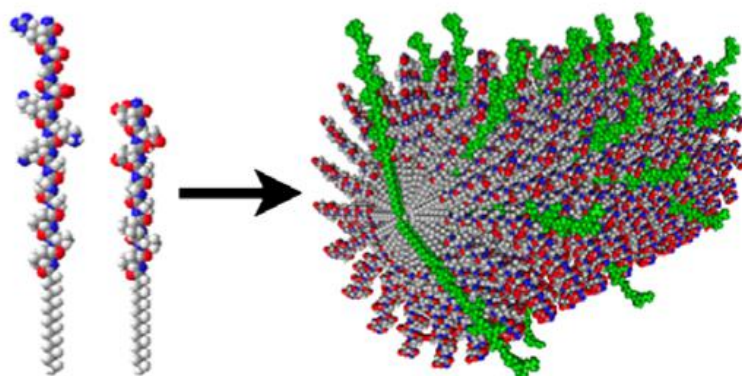


Figure 4.4 PA assembly when used as a carrier for therapeutic cell delivery. Some strands of polar peptides are replaced with reactive agents. When these nanorods come in contact the cell membrane (see Fig. 4.2), they are released in close proximity to the targeted cell.

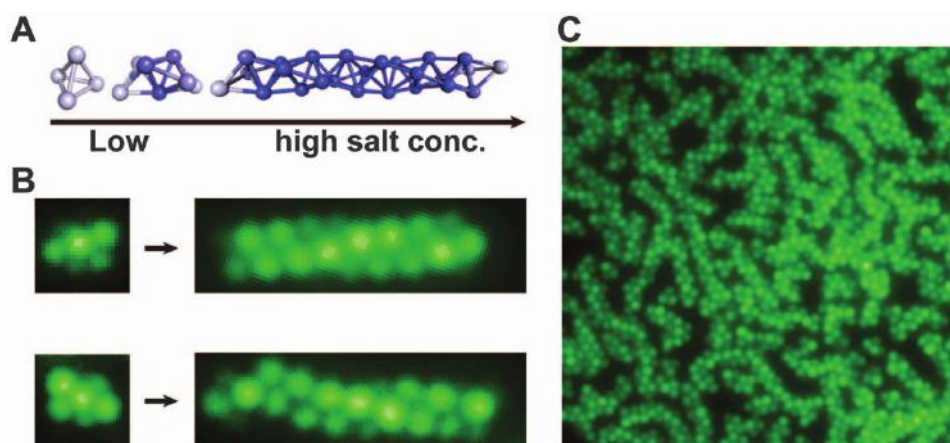


Figure 4.5 (A) By increasing the salt concentration of the solution, larger particle clusters are formed. (B) Fluorescence images illustrating the comparison between a small chiral cluster at low salt concentration (3.8 mM NaCl) and a longer helical cluster (at 5 mM NaCl). The Janus spheres have a diameter of $1\ \mu\text{m}$. (C) Fluorescence image illustrating the stability of worm-like structures at high volume fraction (adapted from Ref. [176]).

2 Model and simulation technique

The system of interest consists of soft spheres in a three dimensional geometry. Each spherical colloid is composed of two hemispheres, one being hydrophobic while the other hemisphere has an electrostatic charge. The implementation of the JP model in order to perform molecular dynamics

was already discussed in Sec. 2 and will not be repeated here. The polar vector $u_i(\theta_i)$ that indicated the centre of each patch are now defined by the spherical angles $\omega_i = (\theta_i, \phi_i)$ for which the same pair potentials apply to, namely Eq. (3.4). The same procedure (outlined in Sec. 3) is carried out for the three dimensional form of the pair potential in order to have a smooth potential around the borders of the two hemispheres and to define continuous torques.

Furthermore, in [176] critical design rules are given for the formation of large scale helical clusters. The first point is that the interaction range of the electrostatic repulsion must be short relative to the particle size, in order to have aggregation (which we have previously discussed in Sec. 3). In order to produce helical superstructures, small clusters of aggregates must grow into larger assemblies, changing their local structure. For very high salt concentrations, the electrostatic interaction between neighbouring clusters becomes negligible which causes particles to aggregate irreversibly. This results in an assortment of small scale aggregates [177], except for large densities. Lastly, the size of the hydrophobic patch must be large enough so that each particle in the cluster has sufficient orientational freedom in order to promote dynamical conversions between clusters. In figure 4.6 observed reaction pathways between individual particles and larger aggregates are shown. Because of the size (and corresponding orientational freedom) of the hydrophobic hemispheres dynamical interconversion between several states are possible. They form an extensive network in which multiple cluster possibilities emerge from each point.

In order to consolidate the dynamical pathways of helical cluster formation with a condensed framework, in which we want to perform MD simulations for the assembly of a single helical structure, the following scheme is proposed: A three-dimensional simulation box is considered with a computational unit cell of 500 – 2500 particles. The size of the rectangular unit cells measures 50σ in the x/y-direction and 1000σ in the z-direction.

Particles are confined in a circular symmetric harmonic trap

$$V(x, y) = \frac{1}{2}K(x^2 + y^2), \quad (4.1)$$

and periodic boundary conditions are applied in the perpendicular direction, forcing the colloids in a quasi one-dimensional state. The constant of the harmonic trap is slowly increased during the simulation. After a certain confinement potential is reached, the temperature of the solution is annealed from room temperature (300 K) to 0K to find the minimum energy configuration of the dynamically acquired structure. The role of the harmonic trap is to promote nucleation at the centre of the simulation cell. By slowly increasing the strength of the confinement, different nucleated cluster can reconfigure and form a single assembly. Growth proceeds by rotations of particles in a feeder cluster. Particles that are located at the ends have the largest rotational freedom, and act as nucleation

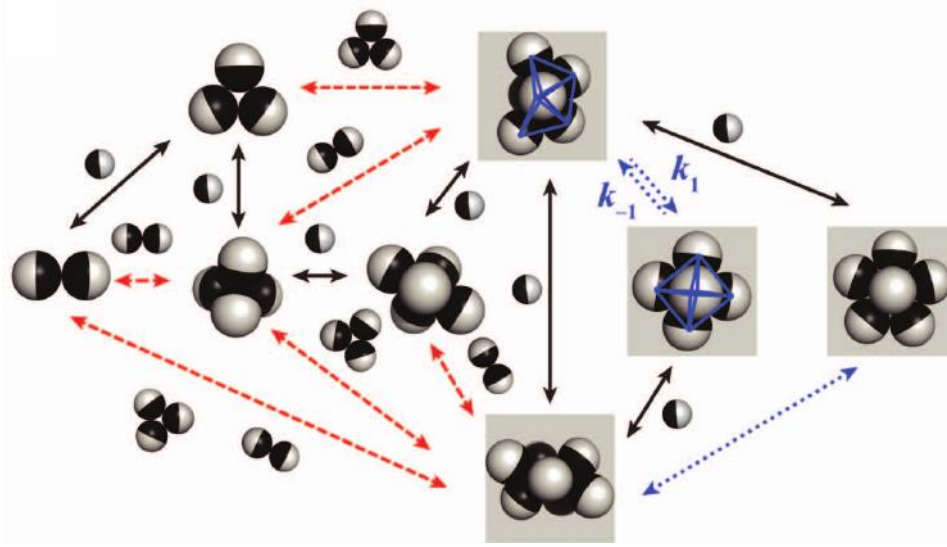


Figure 4.6 Network of reaction pathways at low salt concentration (3.8 mM NaCl), all of which were experimentally observed. Black hemispheres indicate hydrophobic surfaces, and grey surfaces are electrostatically charged. Different reaction mechanisms are denoted by coloured arrows: monomer addition (black), cluster fusion (red), and isometrisation (blue) (adapted from Ref. [176]).

points for new particles to join the growing cluster. Parameters are chosen such that particles can hardly interpenetrate. Parameters are chosen similar to those used in the previous chapter, outlined in table 3.1, unless stated otherwise. The size of a single time-step is decreased to $\Delta t = 0.005s$. A single simulation consists of $1.5 \cdot 10^5$ time-steps: during the first $5 \cdot 10^5$ steps, the confinement potential is increased from $K = 0.05 \text{ aN}/\mu\text{m}$ to $K = 0.2 \text{ aN}/\mu\text{m}$, after which the temperature is annealed.

3 Numerical results

3.1 Morphologies

By varying the concentration of particles inside the channel, we find a series of different morphologies, which we will characterize here by the geometric shape of the basal area. The complete morphology diagram is remarkably rich: for each geometric shape of the basal area, different superstructures exist with tunable helical properties which we will address in the following section. In this part however, we will focus only on periodic superstructures without particular helical properties. As we will show in the following section, these assemblies correspond with a large inverse screening length $\kappa\sigma$ for which the electrostatic repulsion is small. Assembling superstructures with different

geometries can be done merely by altering the packing fraction. The emergence of chirality, on the other hand, is the result of a competition between interactions with different length scales. This has been shown previously in other colloidal systems such as asymmetric dumbbells [178, 179] and disc-like ellipsoids [180]. Here, we show the same mechanism for spherical particles, where the asymmetric length scales are a result of patch interaction rather than using asymmetric colloids.

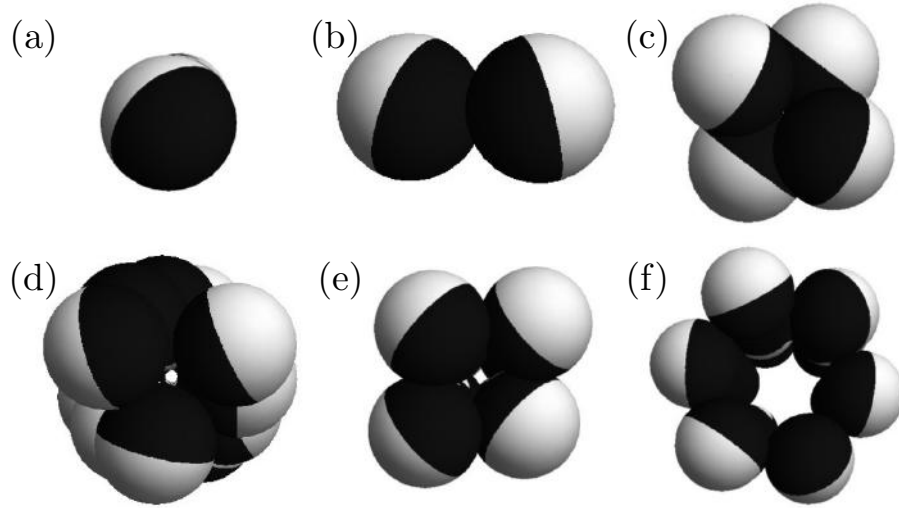


Figure 4.7 Basal area of different elongated superstructures at increasing packing fraction for $\kappa\sigma = 0.95$:

(a) single chain ($\eta \leq 2 \cdot 10^{-3}$), (b) double chain ($2 \cdot 10^{-3} \leq \eta \leq 4 \cdot 10^{-3}$), (c) rotated dimer ($4 \cdot 10^{-3} \leq \eta \leq 4.5 \cdot 10^{-3}$), (d) Bernal spiral ($4.5 \cdot 10^{-3} \leq \eta \leq 6.5 \cdot 10^{-3}$), (e) rectangular chain ($6.5 \cdot 10^{-3} \leq \eta \leq 8 \cdot 10^{-3}$), (f) and finally a chainlike structure with a pentagon at its base ($\eta \geq 8 \cdot 10^{-3}$).

In Fig. 4.7 the different superstructures are shown for increasing packing fraction $\eta = 4/3N_{part}\pi\sigma^3/(L_xL_yL_z)$, where N_{part} is the number of particles of size $4/3\pi\sigma^3$ in a simulation box lengths L . Each of these phases correspond with a complete simulation run carried out at a different initial packing fraction. For a packing fraction $\eta \leq 2 \cdot 10^{-3}$ all the colloids trapped in the parabolic confinement can occupy the centre of the trap (Fig. 4.7a), forming a single chain in the vertex of the trap. For $\eta \geq 2 \cdot 10^{-3}$ it becomes unattainable for all the colloids to position themselves in the centre, and a double chain is formed (Fig. 4.7b). The apolar patch of the Janus sphere is attracted to the interior of the structure, and the polar charged hemisphere is presented to the outside of the structure. The formation of two anti-parallel chains is favourable both for the masked hydrophobic patch, as for the charged patch which attains a low number of neighbouring charges. For $\eta > 4 \cdot 10^{-3}$ also this density restricted configuration reaches its limit. Before the superstructure switches to a

triangular morphology, there exists an intermediate structure where each sequential ‘dimer’ is rotated by 90° , reducing the length of the total complex (Fig. 4.7c). This state is stable in a small region of densities up to $\eta > 4.5 \cdot 10^{-3}$. Here we find a helical assembly with a triangular base (Fig. 4.7d). Helical assemblies will be discussed in the subsequent sections, but it is worth mentioning here that no straight complexes with a triangular base are found. We will discuss this *tetrahelix* in detail in Sec. 3.3. Following this we again find a straight complex with a square base between $6.5 \cdot 10^{-3} \leq \eta \leq 8 \cdot 10^{-3}$ (Fig. 4.7e) above which the system orders itself to form a pentagon (Fig. 4.7f). At even higher packing fractions ($\geq 1.2 \cdot 10^{-2}$), the spacing in-between the base is large enough to fit a particle at its centre, which will not be studied here.

3.2 Tunable pitch

By altering the range of the electrostatic repulsion, we find that the colloidal building blocks can form superstructures with a tunable pitch. This effect has been observed for the different helical structures that were produced in our simulations. In Fig. 4.8 three different morphologies are given that arise when varying solely the value of $\kappa\sigma$. For a low value of $\kappa\sigma$ (which coincides with a long range interaction), the resulting superstructure is a planar zig-zag chain. When we decrease the length of the electrostatic repulsion, we find the same zig-zag structure, twisted in a helix. Reducing the interaction-range even further, we find a straight linear chain of colloids, consistent with what would be expected as a solution of hard-spheres in a confinement potential without any additional inter-particle interactions. By simply altering the interaction range of the repulsive component, the morphology can be altered between linear, planar or helical.

This mechanism of unfolding of a helix when decreasing the interaction range can also be seen for more complex structures. In Figs. 4.9 and 4.10 we observe the same mechanism at higher packing fractions for a helix that contains two ($\eta = 3 \cdot 10^{-3}$) and four ($\eta = 7 \cdot 10^{-3}$) intertwined strands. When gradually reducing the range of the repulsive interaction between the charged hemisphere of the JPs, the helix unravels and we are left with two or four straight chains of JPs with opposite orientation towards the centre of the complex.

3.3 Boerdijk-Coxeter helix

A Boerdijk-Coxeter (BC) helix is a helical assembly of regular tetrahedra, arranged so that the edges of the complex form three intertwined helices with a non-trivial translational or rotational symmetry. Although one would expect to find the thermodynamically favoured a $3(0,1,1)$ helix [164] (a helical structure with three particles at its base arranged in a triangular lattice), these structures have been found experimentally in solutions of Janus particles at high particle concentration [176]. Their

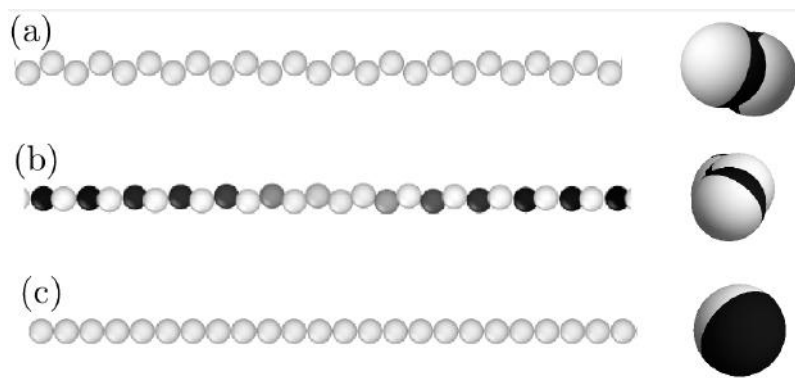


Figure 4.8 Different helical structures while varying the electrostatic interaction range for $\eta = 10^{-3}$: (a) planar zig-zag chain for $\kappa\sigma = 0.05$, (b) one full rotation of a helical chain for $\kappa\sigma = 0.35$, (c) and straight chain for $\kappa\sigma = 0.95$. The particles in the chain are coloured by their inclination in Z-direction. On the right hand-side, the basal area of the chains are shown in accordance with Fig. 4.7.

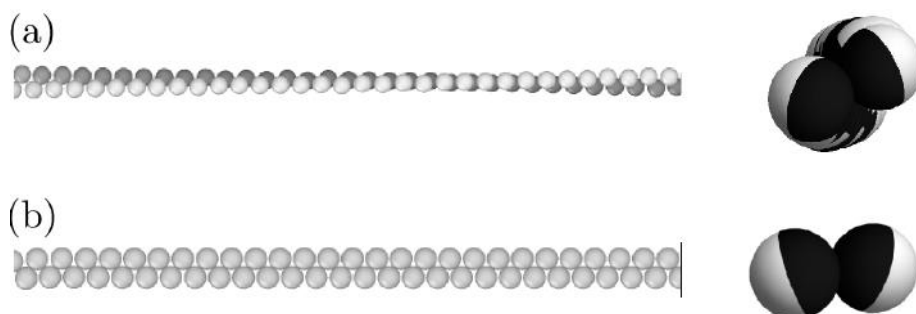


Figure 4.9 Helical superstructure consisting of two intertwined spirals ($\eta = 3 \cdot 10^{-3}$) (inset (a), showing one helix turn) for $\kappa\sigma = 0.25$, and corresponding straight complex (b) for $\kappa\sigma = 0.95$.

appearance have been accredited to being kinetically more favourable: during the initial formation of the helix, the base building block of a BC helix (which is a capped trigonal bipyramidal isomer) is preferred over the octahedrol isomer which forms 3(0,1,1) helices. Once formed, the relaxation of a BC helix into a 3(0,1,1) helix would require a collective transition, in which for each group of three particles at least one bound must be broken. In Fig. 4.12 the difference in free energy per particle is shown between these two clusters as a function of size of the hydrophobic patch. Using the distilled framework of molecular dynamics simulations, we find that these metastable BC helices indeed are found in a wide range of $\kappa\sigma$ values ($0.12 \leq \kappa\sigma \leq 0.5$), while a 3(0,1,1) helix is never observed.

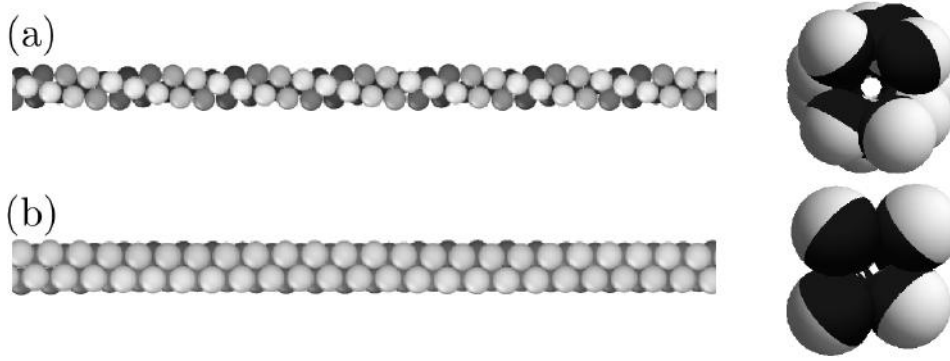


Figure 4.10 Helical superstructure at $\eta = 7 \cdot 10^{-3}$ consisting of: (a) four intertwined spirals for $\kappa\sigma = 0.15$, and (b) corresponding straight complex for $\kappa\sigma = 0.95$.

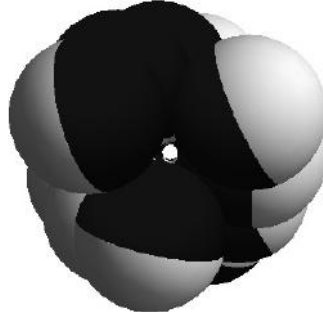


Figure 4.11 Top view of a Boerdijk-Coxeter Helix, which consists of 3 intertwined chains where the position of each particle can be constructed from Eq. (4.2).

The coordinates for the vertices of these tetrahedral structures are given by the sequence [181]:

$$s_n = (r \cos(n\theta), \pm r \sin(n\theta), nh), \quad (4.2)$$

where $r = 3\sqrt{3}/10EL$, $\theta = \arccos(-2/3)$ and $h = EL/\sqrt{10}$, and EL is the edge length of the tetrahedra. The \pm sign in front of the second term determines the chirality of the helix. Due to the irrational nature of θ , it is clear that the BC helix will have an aperiodic nature. A top-down view of the structure can be seen in Fig. 4.11.

In Fig. 4.14 we show the transition between a large unconnected single spiral and a close-packed Boerdijk-Coxeter helix. This is accomplished by varying the screening length over a broad range of $\kappa\sigma$ values. For small values of $\kappa\sigma$ the repulsion between neighbouring particles is strong enough to overcome the strength of the confinement potential, regardless of their relative orientation, and no bound state is present. For a critical value of $\kappa\sigma$, the interaction between particles will be determined

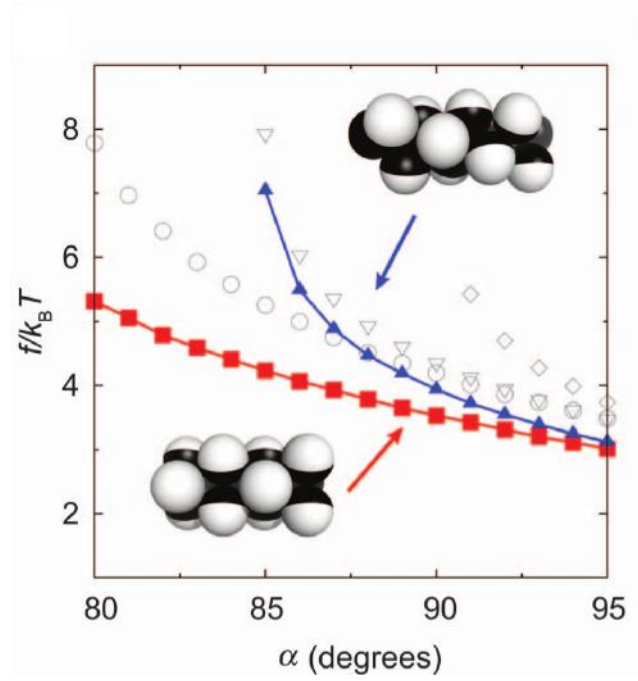


Figure 4.12 Free energy per particle as a function of half the opening angle of the hydrophobic patch. The blue line corresponds with the found BC helix, whereas the red line indicates the free energy of is the 3(0,1,1) helix (adapted from Ref. [176]).

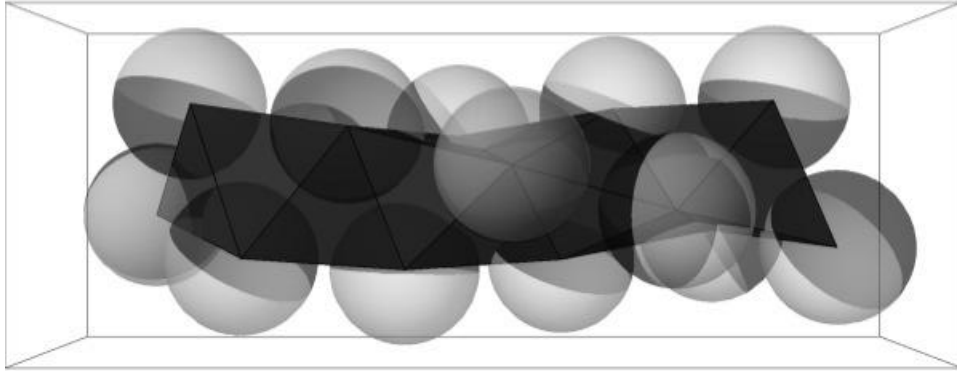


Figure 4.13 Illustration of a BC helix found in simulations alongside a reconstruction of the underlying tetrahelix structure as described by Eq. (4.2).

by their orientation towards one another, and the structure transforms to a triple-helix. We find that the angle θ as introduced in Eq. (4.2) becomes well-defined for the entire structure, and more importantly equal to $\arccos(-2/3)$, in agreement with the definition of a BC-helix. As the value of

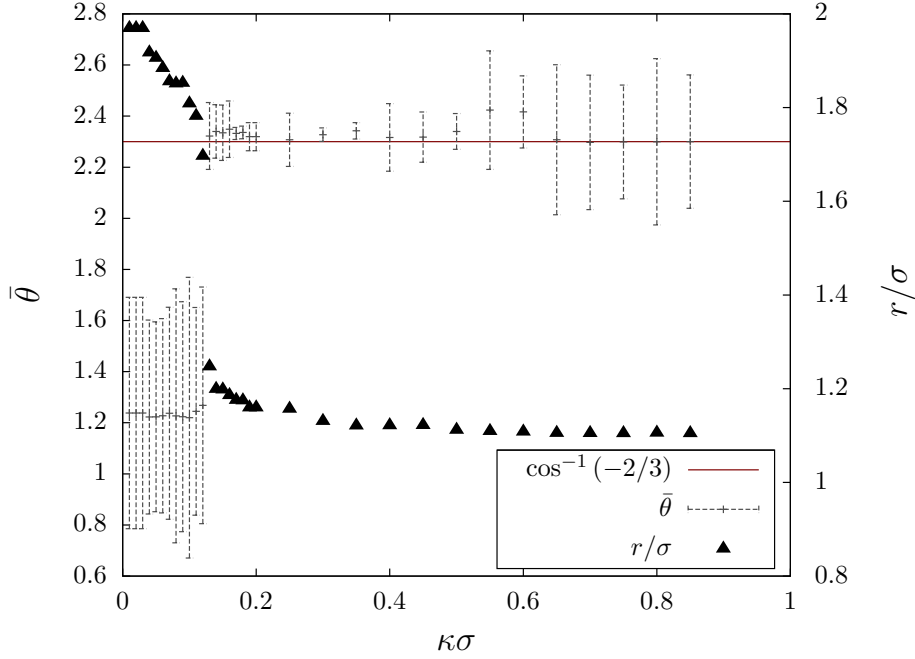


Figure 4.14 BC helices are characterized by the sequence given by Eq. (4.2). The triangles are the value of $r = 3\sqrt{3}/10EL$ and correspond with the edge length of the tetrahedra, while θ is the angle between sequential particles in the helix. For $\kappa\sigma \simeq 0.12$ a sharp transition is observed between a single helix and a Boerdijk-Coxeter triple helix, which is also apparent in the value for the radius r of the helix. For larger values of $\kappa\sigma$ the BC state becomes less dominant in the system, which can be seen by the large variance of θ .

$\kappa\sigma$ is further increased, we find that the spread on the mean value of θ increases. In this regime the repulsion between the charged hemispheres is weak enough to allow more stochastic variations on the orientation of the JPs during the nucleation of the complex. In Fig. 4.13, the underlying tetra-helix structure is shown for $\kappa\sigma = 0.18$. We find an excellent agreement between the tetrahedra as described by Eq. (4.2) and the helical packing of Janus spheres.

4 Discussion and conclusions

Using molecular dynamics simulations, we studied a system of Janus particles weakly confined in a three-dimensional channel. Each particle consists of a charged hemisphere, and the other being hydrophobic. The electrostatic repulsion between colloids in solution takes the form of a screened-Coulomb potential given by the DLVO theory. The different morphologies were discussed for a wide

range of packing fractions in the channel. The basic Janus pair-dynamics of shielding the hydrophobic patch from the liquid on the one hand, and maximizing the distance between charged hemispheres gives rise to a rich variety of morphologies, which are identified according to the arrangement of the particles in a single base. A striking property of these chains is that their helicity is altered depending on the ionic concentration of the environment which can be easily achieved experimentally by changing the salt concentration of the solution. We showed the formation of helices consisting of single, double, triple, and quadruple chains. Lastly, the formation of Boerdijk-Coxeter helices was discussed. Our results reinforce the importance of kinetic selection in the formation of BC helices, as first observed in an experiment by Chen et al. [176]. Where the experimental setup consisted of a large network of worm-like structures, we established that BC helices indeed are found in a wide range of $\kappa\sigma$ in an uncluttered system. Furthermore, we showed that the proclaimed BC helix indeed has an aperiodic sequence, and is kinetically the most favoured structure in a wide range of electrostatic screening lengths.

Part III

Flat ice between graphene layers

CHAPTER 5

AA-stacked bilayer square ice between graphene layers?

The phase diagram of water and its extraordinary properties have been an interesting topic of research in biology, chemistry, and physics for many decades. Depending on the hydrophobic confinement width several two-dimensional ice structures can be formed [182–185]. Different theoretical methods, e.g. molecular dynamics (MD) simulations using different force fields [182, 185], density functional theory [186], and Monte Carlo simulations [187], have been used to study ice formation in the presence of high pressure. In particular, monolayer ice was proposed by Zangi and Mark [182, 183] using MD simulations by applying a five site and tetrahedrally coordinated model, i.e. TIP5P. They confined water between two parallel plates and applied a high lateral pressure (P_l) of about 1 GPa and found a non-flat monolayer of ice.

Recently, it was found experimentally that confined water exists as a quasi two dimensional layer with different properties than those of bulk water [188, 189]. Graphene, the two-dimensional allotrope of carbon, was used in a recent experiment to confine water [189] into monolayer, bilayer and three layers. Using transmission electron microscopy (TEM) a square lattice structure was observed.

The lateral pressure for confining water between two sheets of graphene can be estimated [189–191] to be about 1 GPa using the van der Waals (vdW) adhesive energy between two layers which is typically around $20 \text{ meV}\text{\AA}^{-2}$. This experiment was supported by MD simulations that showed that by increasing the pressure, bilayer square ice (three layer ice) with a lattice constant of 2.82 \AA nucleates where the graphene layers are separated by a distance $h = 9 \text{ \AA}$ (11.5 \AA) [189]. However, the MD simulations failed to reproduce the experimental found AA-stacking of bilayer ice. Ab-initio calcula-

tions found that monolayer ice confined between hydrophobic graphene layers can be rippled or flat, depending on the confinement width and lateral pressure [186]. However, this DFT study is based on a small super-cell which therefore missed structures that involve more than 4 water molecules.

Using the reactive bond order potential, that was introduced in Sec. 5 we reveal new physics of confined ice between two graphene layers. We performed annealing MD simulations starting from high temperature, i.e. 400 K and found the low temperature minimum energy configuration, and determined the structure of monolayer, bilayer and three layer ice. We evaluate the different energy terms, charge distribution, and hydrogen bond strength of confined water. The ReaxFF potential allows for different bond formations and takes into account the polarization of charge within the molecules, which makes our study very different from previous investigations. The studied systems are found to be all flat, non-polar and non-ferroelectric where the microscopic structure depends on the number of ice layers.

The first section attempts to give an overview of the current state of work concerning water clustering near interfaces, as well as a detailed overview of the experimental observation of square ice between two graphene layers on which our study is based upon. The second section discusses the used methodology in order to replicate the experimental system of confined ice. A third section concentrates on the acquired numerical results, where a comparison is made with the experimental observations. Finally our conclusions are given in the final section. Results presented in this chapter have partially been published in Ref. [192].

1 Introduction

1.1 Structure of ice

Ice is a naturally occurring solid with a regular crystalline structure, based on the molecule of water. However, many of the physical properties of ice are controlled by the formation of hydrogen bonds between oxygen and hydrogen atoms from neighbouring water molecules. Ice is known to have a multitude of crystalline forms, most of which are only created in laboratory conditions. In Fig. 5.1 some of the phases of bulk ice are given as a function of pressure and temperature.

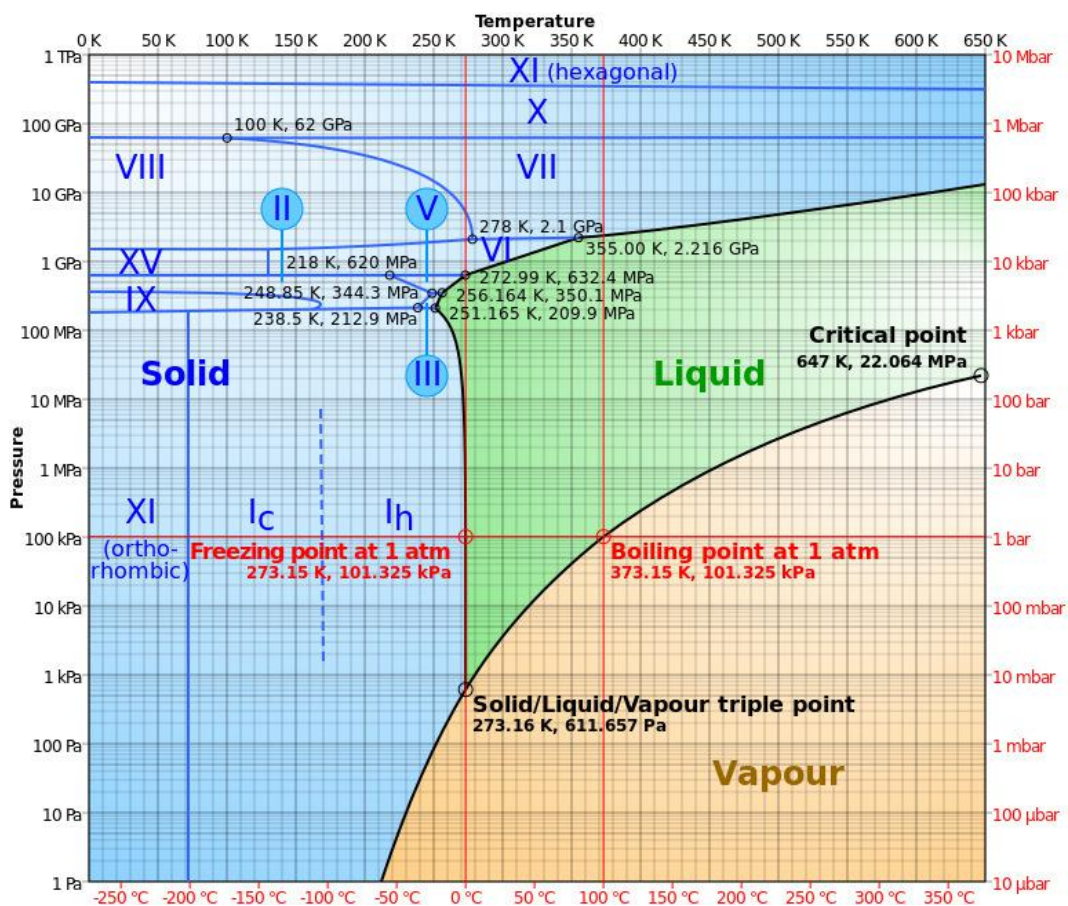


Figure 5.1 Phase diagram of water as a log-lin chart with pressure from 1 Pa to 1 TPa and temperature from 0 K to 650 K. The dashed line between I_c and I_h indicates a metastable phase (adapted from Ref. [193]).

Virtually all ice in the biosphere is I_h , with a hexagonal crystal structure as depicted in Fig. 5.2. Oxygen atoms (shown by open circles), are arranged on a hexagonal lattice where each atom has four nearest neighbours arranged at the corners of a regular tetrahedron. Molecules are linked to another by hydrogen bonds, where each molecule offers its hydrogen atoms to two other molecules and accepts two hydrogen bonds from different molecules.

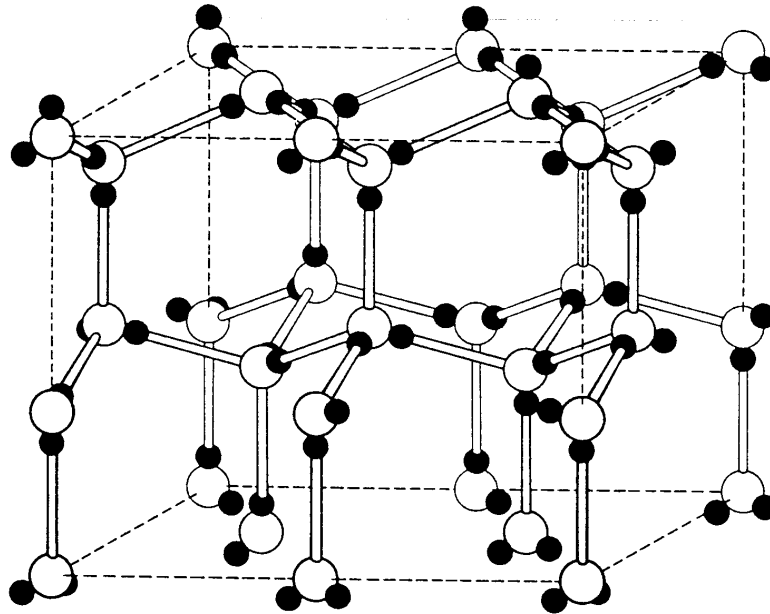


Figure 5.2 Ice I_h structure consisting of the formation of four hydrogen bonds for each water molecule in the crystal. The molecules are arranged in a hexagonal lattice, where the distance between oxygen atoms along a bond equals 2.76 \AA (adapted from Ref. [194]).

The arrangement of the structure of the different phases of ice follows the so-called Bernal-Fowler rules (also called ice-rules) that state that [195]:

- (a) Each oxygen is covalently bonded to two hydrogen atoms.
- (b) There is precisely one hydrogen between each pair of oxygen atoms.

These rules do not imply that the crystal is uniquely defined, nor does it have long-range order in the orientations of the molecules. There are many ways to arrange the hydrogen bond network such that these rules are satisfied, all of which are equally probable. In fact, the ice-rules were devised in part to account for the known zero-point entropy of ice [196]:

Considering an ice crystal of N molecules (and ignoring the boundaries), then there will be $2N$ bonds between these molecules with one proton between each bond. The neighbours of each molecule are

arranged in a tetrahedron, so that the two hydrogen atoms can be placed in 6 different configurations (shown in Fig. 5.3).

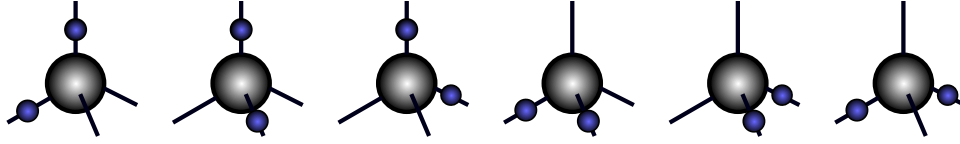


Figure 5.3 Six possible orientations of an H_2O molecule at a given site in the lattice.

Ignoring the second ice rule for a moment, we find that there are 6^N possible arrangements of these molecules. Each bond within these possible arrangements will have one of four equally possible states: HH , $H-$, $-H$ or $--$, where H expresses the presence and $-$ the absence of a proton. The fraction of the 6^N arrangements in which all $2N$ are correctly bonded is $(\frac{1}{2})^{2N}$, so that the total number of acceptable configurations of the crystal is given by:

$$W = 6^N \left(\frac{1}{2}\right)^{2N} = \left(\frac{3}{2}\right)^N. \quad (5.1)$$

So that the zero-point entropy S_0 given by the Boltzmann relation equals:

$$S_0 = k_B \ln W = Nk_B \ln \frac{3}{2}. \quad (5.2)$$

Secondly, the H-O-H angle of 104.52° of a free water molecule does not exactly fit into the tetrahedral bond angle between oxygen atoms of 109.47° , and a complication arising from the disorder in hydrogen bonds is that molecules are subjected to small displacements in the lattice of their average sites, further increasing the disorder in the crystal.

Within a macroscopic piece of ice, many arrangements of the hydrogen atoms are consistent with the ice rules. For small water clusters, or water in confined geometries the first ice rule is often violated as the geometry of the confinement forces the hydrogen-bond network to be terminated near the its surface.

1.1.1 Small isolated clusters

Interestingly, when the first attempt was made at modelling the structure of ice in terms of the individual molecules Bjerrum argued the dipole-dipole interaction between adjacent molecules would favour a *trans* configuration, in which the dipole moments of two neighbouring molecules point in opposite directions [198]. It was later shown that this effect would be weakened when additional

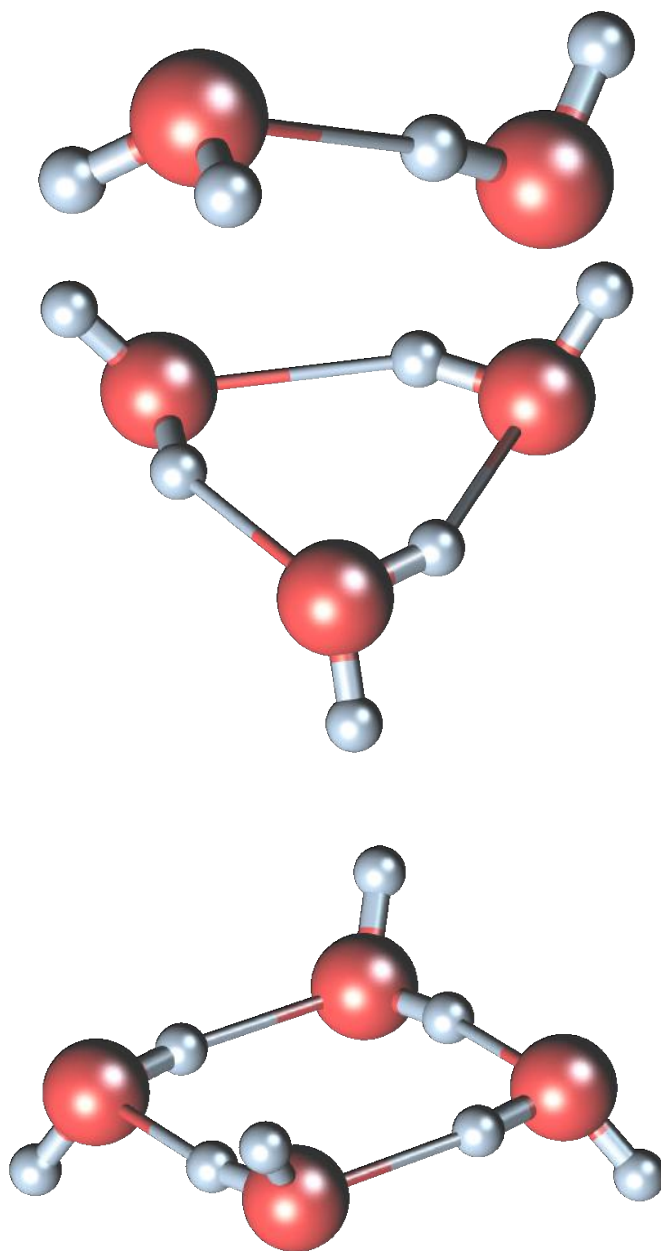


Figure 5.4 Visualisation of the experimentally-identified structures of a water dimer (top), trimer (middle) and tetramer (bottom). The oxygen-oxygen distance r_{OO} is measured to be 2.98 Å (dimer), 2.88 Å (trimer), and 2.83 Å (tetramer) in ab initio calculations (adapted from [197]).

molecules were taking into account in a three dimensional lattice [199]. However, in small scale water clusters $(H_2O)_n$ the most energetically favourable structures exhibit this effect, as can be seen in Fig. 5.4. In these small aggregates, the distance between neighbouring oxygen atoms is measured to be larger then the lattice constant of hexagonal ice (2.76 Å) [200].

1.1.2 Water clusters on a graphite sheet

One of questions concerning water is the extent to which its properties are modified when interacting with a surface and confined environments. At low temperatures (< 150 K), and low coverage, water has been measured to form two-dimensional clusters on top of a graphite layer which converts to a three-dimensional structure upon warming [201]. The geometries of these clusters are predicted to be similar to those of the isolated gas-phase clusters that were shown in Fig. 5.4.

These clusters are adsorbed by the graphite surface layer caused by van der Waals forces. To give a simplified illustration of this effect, consider an adsorbed hydrogen atom in front of a perfect conductor, where the nucleus is located at $R = (0, 0, Z)$ as shown in Fig. 5.5.

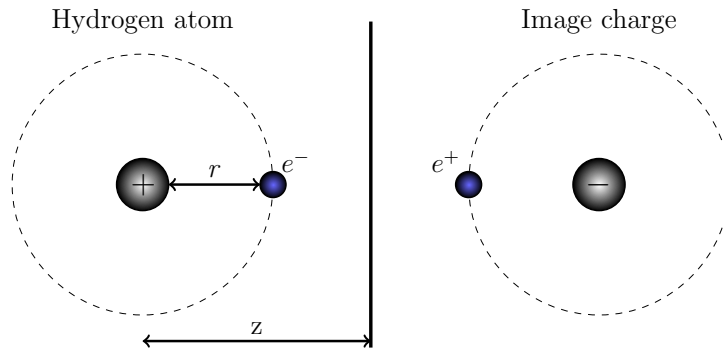


Figure 5.5 Simplified illustration of an adsorbed hydrogen atom near a conductor interacting with its image charges.

The charge distribution of the hydrogen atom will create image charges at the surface. The electrostatic energy between the hydrogen atom and the induced polarisation of the surface can be written down as:

$$V = \frac{e^2}{4\pi\epsilon_0} \left(-\frac{1}{2z} - \frac{1}{2(z-r)} + \frac{1}{(2z-r)} + \frac{1}{(2z+r)} \right), \quad (5.3)$$

taking into account the interaction between the nucleus and electron with the image charges. For $r \ll z$

$$V = -\frac{1}{8} \frac{e^2 r^2}{z^3} - \mathcal{O}(z^4). \quad (5.4)$$

In Fig. 5.6 the adsorption energy is plotted against the interaction distance for a water molecule with its two hydrogen atoms directed upwards from a graphene sheet.

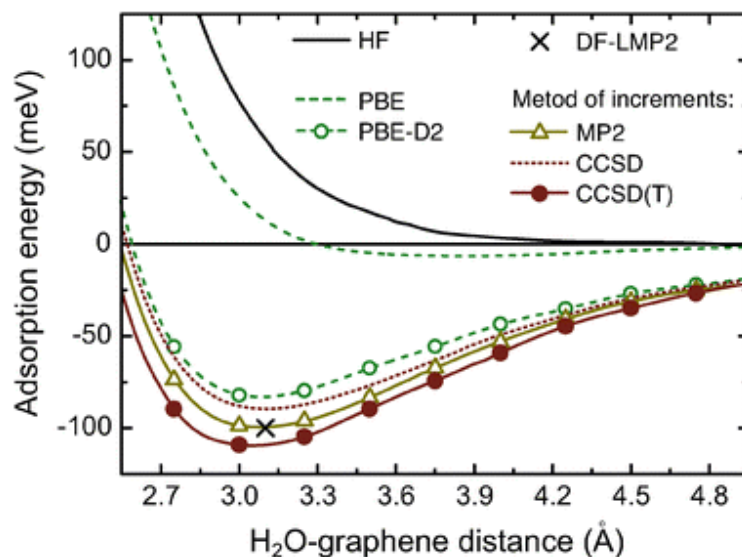


Figure 5.6 H_2O -graphene interaction energy as a function of substrate-adsorbate distance as obtained with different computational methods (adapted from Ref. [202]).

The actual minimum energy structure for a single water monomer on a graphite surface has the water molecule oriented perpendicular to the graphite sheet with one H atom pointed towards the sheet (shown in Fig. 5.7), here the distance between the oxygen atom and the monolayer is calculated to be 3.387 Å [203].

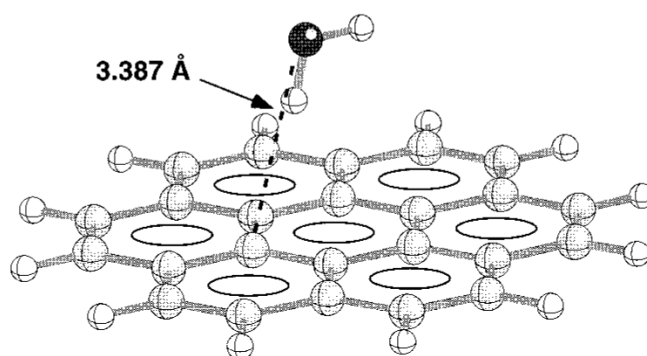


Figure 5.7 Optimized geometry of a monomer adsorbed on a graphite sheet (adapted from Ref. [203]).

In Ref. [204] as comparison is made between different methods, where the distance between the oxygen atom of the physisorbed water molecule and a graphite sheet is also reported to be between 3 – 3.5 Å. In these studies, the binding energy of a single water molecule towards a graphite sheet has been found to be 0.12 ± 0.02 eV, which is smaller than the interaction energy between two water molecules in a fully hydronized network (-0.22 ± 0.01 eV) [203].

Although the graphite-water interaction is significantly smaller than the binding energy in a water cluster (where the hydrogen bonding network consists of four hydrogen bonds), the graphite-water binding energy is sufficiently large to expect a significant role of the surface on the formation of clusters in confined geometries. Moreover, the difference between multiple layers of graphite or a single layer has been calculated to be small, the binding energy is enhanced by $4 \cdot 10^{-3}$ eV, or about 3% [205]. The addition of a third layer was mostly neglected when performing water on graphite calculations [204, 205].

Water molecules can freely diffuse over the graphite layer, the pathway for motion of a water monomer between adjacent rings on the surface is depicted in Fig. 5.8. The energy barrier is calculated to be 10^{-3} eV [205] indicating that monomers will readily diffuse on the graphite surface except for temperatures lower than 150K.

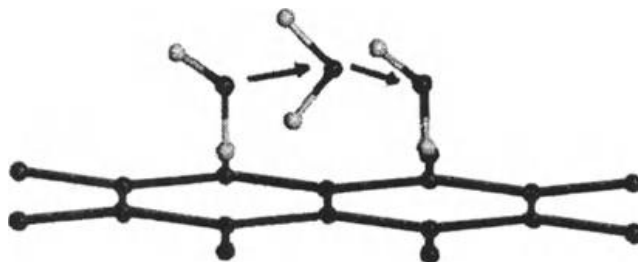


Figure 5.8 Pathway for diffusion of a water monomer on the graphite surface (adapted from Ref. [205]).

With these considerations in mind, it should be clear that it is energetically favourable for water molecules to assemble into clusters on graphite (or graphene) surfaces. In Fig. 5.9, the minimum energy configuration of small water clusters on top of graphite is shown. The geometric configurations of these clusters on a graphite layer coincides with that of the corresponding free water clusters that were shown in Fig. 5.4.

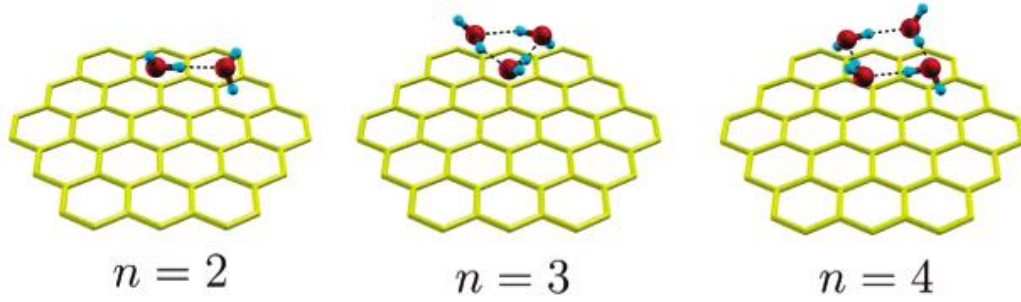


Figure 5.9 Optimized geometries of water clusters $(H_2O)_n$ adsorbed on a graphite sheet (adapted from Ref. [206]).

1.2 Water under extreme confinement

We will consider water under extreme confinement by hydrophobic surfaces, meaning that at least one dimension of the confined space is of the order of a few nanometers. When water is confined in hydrophobic pores, the hydrogen-bond network is forced to terminate at the surfaces. Because of this, the entire hydrogen-bond network is frustrated, causing the properties of the water to be altered, rather than merely perturbed.

1.2.1 Water inside carbon nanotubes

A carbon nanotube (CNT) is a practical example of a quasi-one-dimensional confinement. Water confined in carbon nanotubes has been the subject of extensive studies as the molecularly smooth hydrophobic graphitic walls, and nanoscale inner diameter of a CNT gives rise to a unique phenomenon of ultra-efficient water transport through these molecular pipes. As a result, they demonstrate higher water flux with lower energy than more currently used membranes, making them useful in water desalination and purification applications. Salt ions should be unable to flow through them, because their surrounding shells of water molecules are too wide.

Their interesting diffusive properties aside, we will focus here on the lattice structure of ice in CNTs. Depending on the size of the CNT, different structures are formed which are shown in Fig. 5.10. The confined organizes the water molecules into H-bond connected wires. Each molecule's dipole moment parallels the CNT axis, where it has the lowest potential energy [209].

For larger CNTs clusters of fully hydrogen bonded water molecules are formed, some of which have spontaneous electric polarizations along the axis of the CNT. For larger CNT's the ice structures are less stable (with an exception of $n = 4$, see Fig. 5.10(c)), and are measured to have a lower

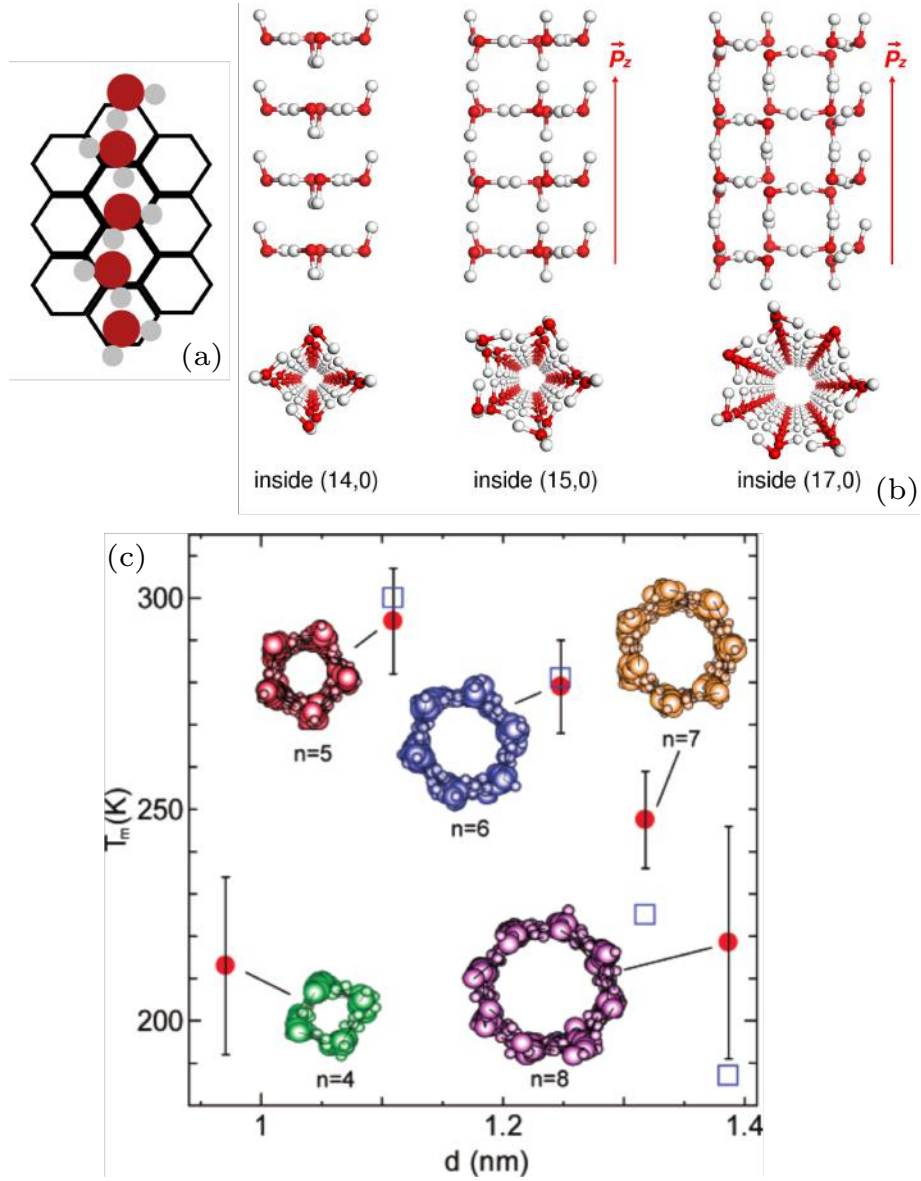


Figure 5.10 Relaxed structures of ice inside carbon nanotubes: (a) water is organized into H-bond connected wires, with each molecules dipole moment parallel to the CNT axis. (b) For larger CNTs different clusters are formed depending on the diameter of the tube. The ice nanotubes inside (15,0) and (17,0) CNTs have spontaneous electric polarizations along its axis direction (adapted from Ref. [207]). In (c), the melting temperature T_m for various numbers of ice-nanotubes ($n=4-8$) is given. Simulation results (red circles) are compared with the experimental results (squares) (adapted from Ref. [208]).

transition temperature. Larger tubular ice structure have not been found, beyond $n = 8$ unstable ice tubes are found where the core is filled with water molecules [208].

1.2.2 Water confined in slit nanopores

The ability of water to form hydrogen bond networks manifest itself not only in bulk and quasi-one-dimensional systems but also in quasi-two dimensional arrangements. In [182] a numerical study

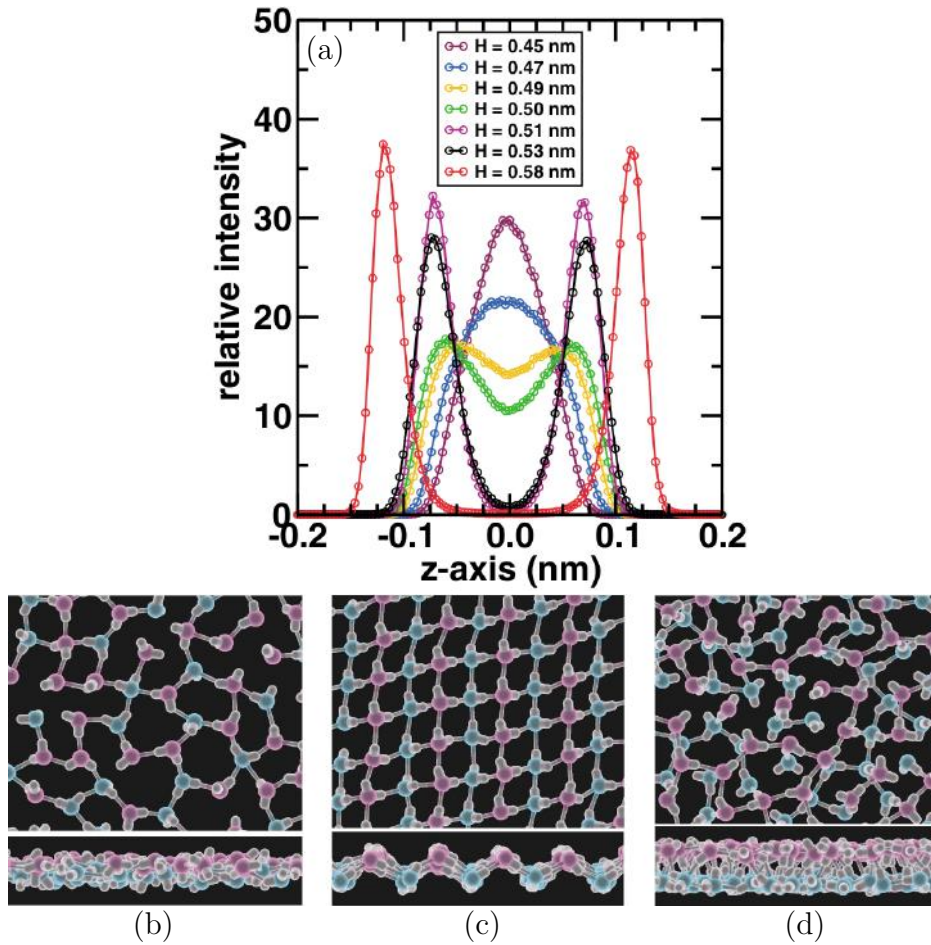


Figure 5.11 (a) Transverse distribution of the density of oxygen atoms for different plate separations H . Below: lateral and transverse views of (b) a water mono-layer at $H = 0.47$ nm, (c) ice mono-layer at $H = 0.53$ nm and (d) a water bilayer at $H = 0.58$ nm. Oxygen atoms that lie above and below the mid-plane are depicted in magenta and cyan, respectively (adapted from Ref. [182]).

was performed using molecular dynamics of water confined between two quartz (SiO_2) surfaces. The structure and dynamics of the water molecules was studied as a function of the distance between the

quartz layers and lateral pressure at $T = 300$ K. For plate separations in the range of $0.41 \leq H \leq 0.50$ nm the mono-layer consists of water molecules in a liquid phase (as depicted in Fig. 5.11(b)). At $H = 0.51$ nm a first order transition is observed in which the mono-layer transforms into a buckled frozen state which is polarized in the lateral direction along the quartz plates (Fig. 5.11 (c)). At $H > 0.57$ nm a liquid state is once more recovered, which forms a bilayer around the mid-plane of the confined area (Fig. 5.11 (d)). The lateral pressure was varied between 1 and 100 bar, for which no obvious difference in the behaviour of the system was found.

2 Square ice in graphene nanocapillaries?

In 2015, a high-resolution electron microscopy image was reported of water locked between two graphene sheets [189]. The observations showed that the confined water forms a *square ice* crystal structure, with a lattice constant of 2.83 \AA . For this study, a graphene monolayer was deposited on

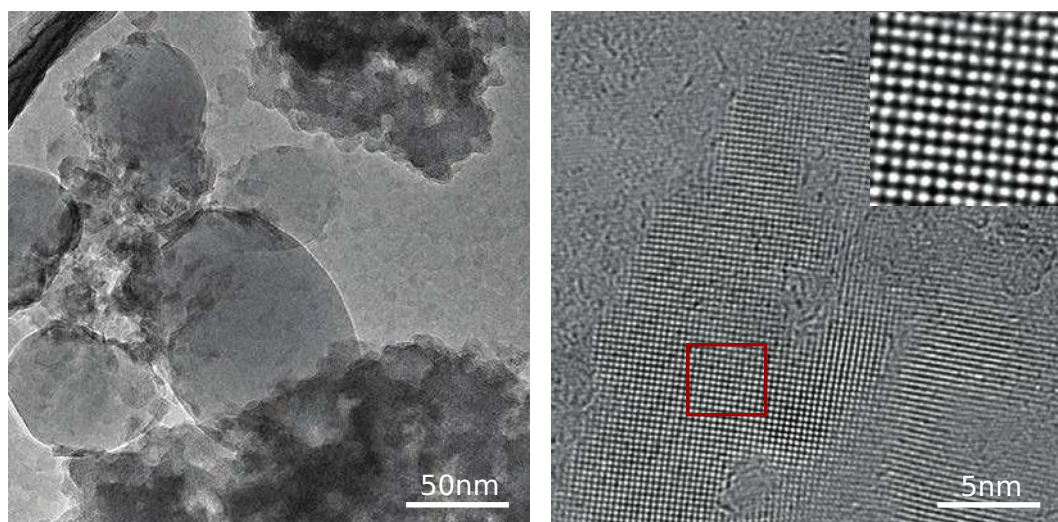


Figure 5.12 (lhs) Low magnification TEM image of a reference sample in which water was trapped in large bubbles with a diameter of ~ 100 nm. (rhs) Part of the water pocket at higher magnification. The top right inset shows a magnified image of the area outlined in red (adapted from Ref. [189]).

a standard transmission electron microscopy (TEM) grid, exposed to a small amount of water and covered with another graphene monolayer. Most of the water was squeezed out by the vdW forces between the two graphene layers, but some water remained trapped in pockets of sub-micrometre size (as shown in the lhs of Fig. 5.12). On the rhs of Fig. 5.12, an atomic resolution image is shown of graphene-confined water. The dark spots correspond to oxygen and are used to indicate the

positions of the water molecules. Hydrogen atoms generate too little contrast to be resolved in the experimental set-up. After taking a Fourier transformation of this lattice, the lattice constant is found to be $2.83 \pm 0.03 \text{ \AA}$ without any alignment with the graphene lattice.

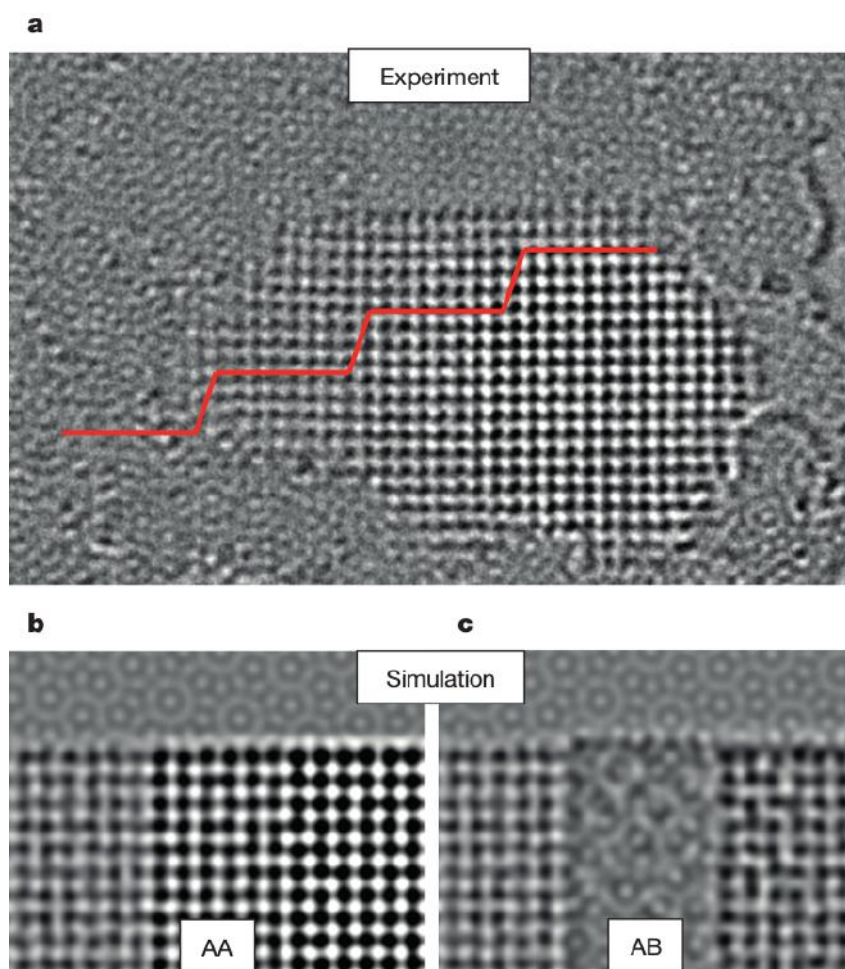


Figure 5.13 (a) Isolated crystallite with a varying number of layers. The red line shows changes in the contrast of the image, occurring in quantized steps. (b-c) Simulated TEM images for monolayer, bilayer, and trilayer ice with AA and AB stacking, respectively. The AA stacking agrees with the experimental images, in contrast with the AB stacked ice results (adapted from Ref. [189]).

In Fig. 5.13(a) contrast variations can be seen, which arise from differences in ice layer numbers (indicated by the red line). No more than three layers of ice are observed in the experiment. In order to find the type of stacking of subsequent water layers, an experimental (Fig. 5.13(a)) TEM image is compared with simulated TEM images of AA and AB stacked oxygen layers (Fig. 5.13(b-c)). In a AB stacked structure oxygen atoms in the second layer occupy the sites between oxygen sites in the

first and third layer. The comparison between simulated and experimentally measured TEM images favours the arrangement of an AA stacked lattice. This observation lead the researches of [189] to conclude that the confined ice formed a cubic crystal lattice corresponding with 90° hydrogen bonding both within and between the layers. This new ice structure does not follow the Bernal-Fowler ice-rules (see Sec. 1.1), in contrast with other observations of ice lattices. Not all oxygen atoms in the lattice are fully hydrogenated. In a cubic lattice, each particle 6 nearest neighbours, while only four hydrogen bonds can be formed. Secondly, a crystal lattice with 90° would mean a strong deviation from the quasi-tetrahedral shape of water molecules: the water molecule has four pairs of electrons on the central oxygen atom. Two pairs are bonded, two pairs are not. The lone pairs of electrons repel the bonding pairs more than the bonding pairs repel each other, closing the 109.5° bond angle down to 104.5° . In a cubic lattice, the bond angle is closed to 90° . According to our simulations, the closing of the hydrogen bond angle to 90° would require approximately 3 eV per water molecule, which is of the same order as the hydrogen-oxygen bond dissociation energy 4.5 eV [210]. The observation of square ice was challenged later by several experimentalists [211]. In the remainder of this chapter, a replication study is done using molecular dynamics in which the resulting crystal structures are compared with the experimental observations as well with previous calculations that were discussed in Sec. 1.

3 Methodology

We employed molecular dynamics (MD) simulations using reactive force field (ReaxFF) potentials [48, 212] in the well-known large-scale atomic/molecular massively parallel simulator LAMMPS [107]. Both of which were introduced in Sec. 5 and Sec. 6, respectively. The ReaxFF potentials used accounts for possible bond-formation and bond-dissociation of different bond orders [213]. It contains Coulomb and van der Waals potentials to describe non-bond interactions between all atoms. One of the main advantages of ReaxFF is that it calculates the polarization of charge within the molecules which is achieved by using electronegativity and hardness parameters based on the electronegativity equalization method and charge equilibration (QEq) methods. Therefore, we believe that ReaxFF is a better candidate to simulate water and the corresponding interaction between water and graphene. Furthermore, the ReaxFF potential allows bond extension/contraction in water as well as angle bending and charge relaxation over each atom. This is in contrast to the traditional force fields for water, e.g. SPC and TIP4P [214] (a rigid planar four-site interaction potential for water) that keep the water molecules rigid during MD simulations.

The computational unit cell contains 34848 carbon atoms and $5700 \times n$ water molecules where n is the number of ice layers. These numbers have been chosen so that the graphene lattice is

commensurate with the water lattice when performing simulations with periodic boundaries. To match two different lattice parameters in a simulation box the following equation should hold: $a_{GEM} = a_{OON}$, where the lattice constants $a_{OO}=2.83 \text{ \AA}$ and $a_{GE} = \sqrt{3}/2 a_{CC}$ and m and n should be integer numbers.

Before starting the minimization we do an annealing MD simulation by performing a NPT simulation starting at 400 K and ending at 0 K, in order to find the true simulation box size and O-O distances. Annealing was done using a combination of a barostat and thermostat with a damping constant of 0.1 ps and a cooling rate of 8 K/ps. The lateral pressure for confining water between two sheets of graphene can be estimated to be about 1 GPa using the van der Waals (vdW) adhesive energy between two layers which is typically around 20 meV \AA^{-2} [189–191]. A typical temperature evolution during the annealing phase is shown in Fig. 5.14. The high starting temperature guarantees that the O atoms and H-bonds can find their minimum energy configurations during the slow annealing process. Then, the total energy is minimized using the iterative conjugate gradient (CG) scheme.

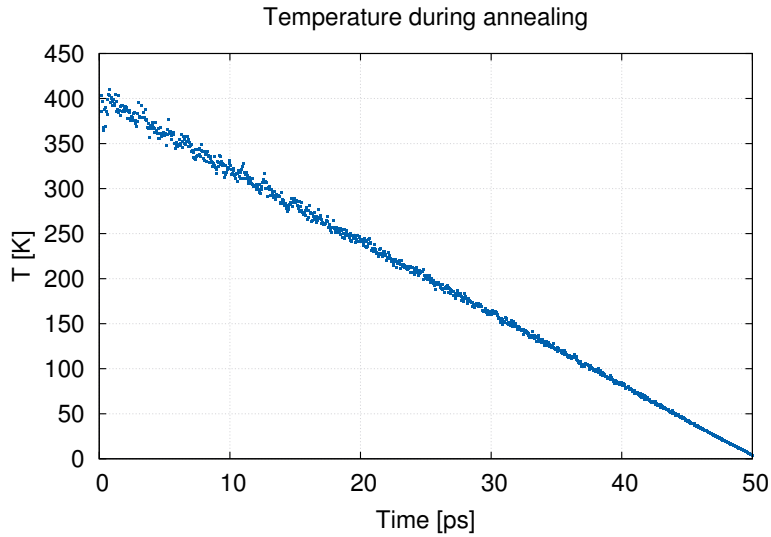


Figure 5.14 Typical temperature evolution of water during the annealing phase.

4 Confined ice

4.1 Monolayer of ice

We start from a random distribution for the H-bonds of the water molecules which are distributed between two graphene layers in a dense square structure, with O-O distance equal to 2.8 \AA . The initial O-O distance is set to have the experimentally observed density for confined ice but during annealing, which we start from 400 K, the positions are allowed to change. The graphene layers are rigid and separated by a fixed distance of 6.5 \AA having AB-stacking. However, the results for the water layer are found to be independent of the exact stacking configuration of the graphene layers.

By minimizing the potential energy, we found a flat rhombic-square lattice structure, see Fig. 5.15. The side view of the minimum energy configuration is shown in Fig. 5.15(a) which is a flat monolayer of ice with successive arrangements of square and rhombic building blocks, see Fig. 5.15(b). If the O atoms remain in the same plane, the H atoms should also be in that plane in order to preserve the symmetry. The other possibility would be a buckled (puckered) structure which results in non-flat ice [182] (which was not found in our simulations).

Our results are partially in agreement with ab-initio results where Corsetti et al [186] used non-local vdW exchange correlations and scanned both the confinement size and lateral pressure. However their unit cell (called Ab/Cd) was too small, i.e. it contained only 4 water molecules, in order to find the aforementioned asymmetry effect. The found rhombic-square structure can be considered as a periodic repetition of a flat water tetramer (as shown in Fig. 5.4 and Fig. 5.9) paralleling the graphene plates.

The crystalline structure and lattice constant of monolayer ice can be determined from the radial distribution function (RDF), see Fig. 5.16(a). We found the O-O distance to be $a = 2.84 \pm 0.01 \text{ \AA}$. The obtained lattice constant is in good agreement with the experimental value of $a = 2.81 \pm 0.02 \text{ \AA}$ and the lattice constant of single water tetramers (2.83 \AA). The angle 'H-O-H' is found to be $\theta = 106.31 \pm 0.03^\circ$ and is identical for all 'H-O-H' bonds. The H-bonding energy is about -0.16 eV which is in the lower range of the H-bond energy of bulk ice, i.e. $-(0.13-0.33) \text{ eV}$ [215]. For a two dimensional configuration of both the valence as well as the hydrogen bonds, a lower energy is to be expected. In Table 5.2, all relevant quantities for the different studied systems are listed.

The corresponding local dipoles of the water molecules in the minimum energy configuration is shown by the arrows in Fig. 5.16(b). Interestingly, the net dipole is zero and the system is non-ferroelectric which is in agreement with ab-initio results [186] and is in disagreement with the TIP5P model prediction [216]. We were able to deform the H-bond orientations using an in-plane electric field of about 1 V/\AA . For this field, we find a structural transition from the minimum energy

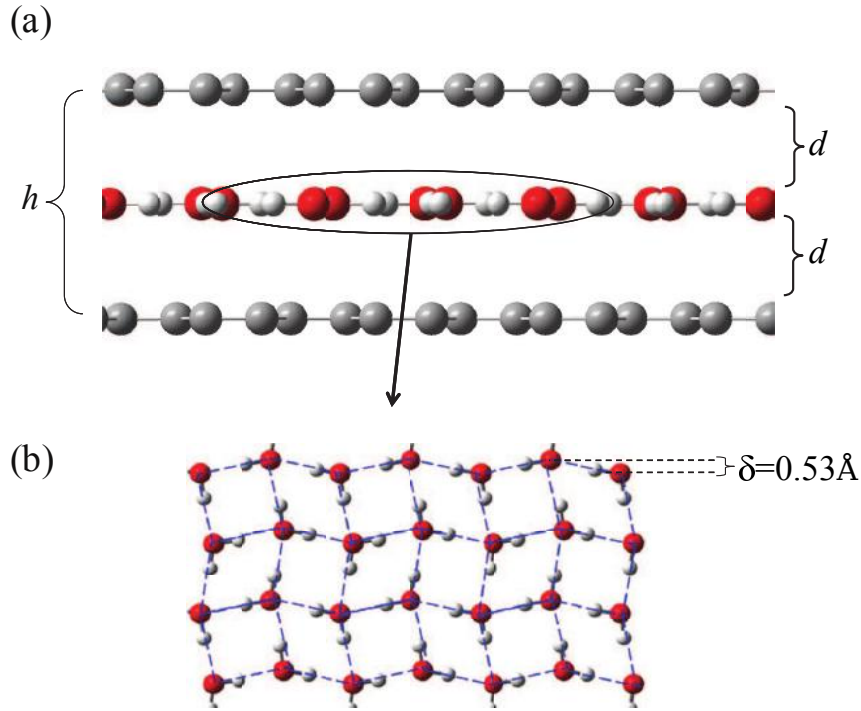


Figure 5.15 Side (a) and top (b) view of the relaxed monolayer of ice between two graphene layers (red(grey) circles indicate O(H) atoms). Parameter h denotes the distance between the graphene layers, d the distance between the ice monolayer and graphene, and δ measures the deviation of the structure to a square lattice.

configuration with zero dipole moment to a new higher energy configuration with a net non-zero dipole moment, i.e. the local dipoles of the water molecules rotate in the direction of the electric field. The effects of an in-plane electric field on a monolayer of 2D ice will be discussed in detail in the following chapter.

For non-polar flat monolayer ice there are many stable structures [186]. We made a detailed investigation of them and present the results of one of the most relevant ones. We performed additional MD annealing and minimization by starting from an initial configuration where the H-bonds are randomly oriented in three dimensions but have the same orientation for each water molecule. We found that the minimum energy configuration is a flat and polar structure which is shown in Fig. 5.17. The potential energy of this structure is 10 meV/atom higher than the non-polar structure (Fig. 5.15). We also performed simulations for the other possible polar structures proposed by Corsetti *et al.* [186] and found that all of them have higher energy than the one shown in Fig. 5.15.

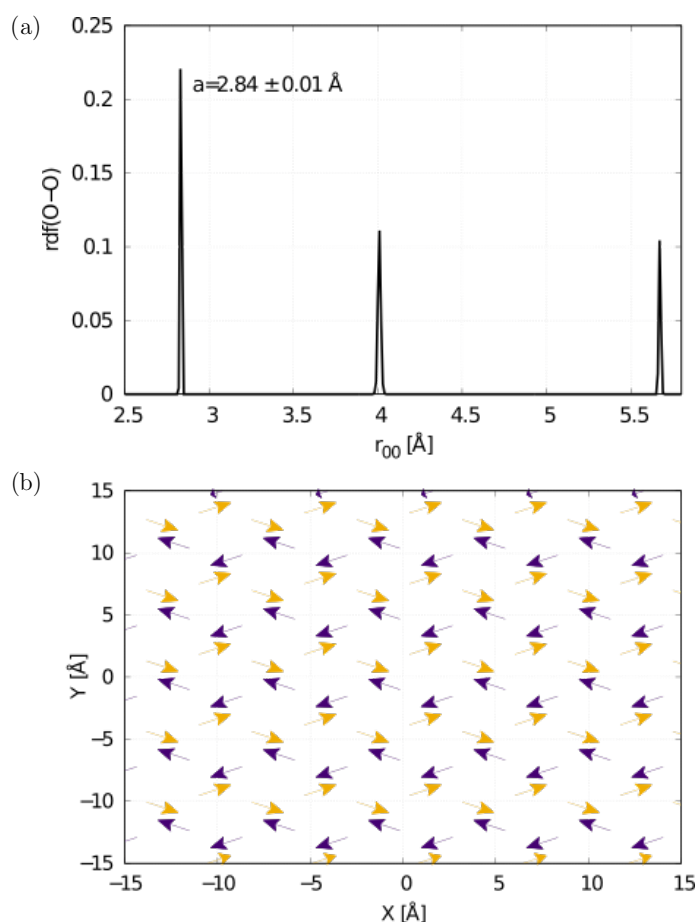


Figure 5.16 The (a) radial distribution function for O-O distances and (c) the local dipoles of the individual water molecules.

The role of the graphene layers is to act as a flat hydrophobic and inert surface which forces the hydrogen-bond network to be terminated at the surfaces. This indicates that the found phase should be present inside hydrophobic nano-channels independently of their exact atomic nature. By changing the graphene layers with hexagonal boron nitride (h-BN) we were able to check this hypothesis. Hexagonal boron nitride has a structure similar to graphite: within each layer boron and nitrogen atoms are bound by covalent forces, whereas the layers are held together by van der Waals interactions. In order to test the relevance of graphene in the observed phenomena, the two graphene layers were replaced with monolayers h-BN. The interaction between the water atoms are still determined by the Reax force field, but because of the lack of ReaxFF to deal with BN a LJ potential was used for the interactions between B-O and N-O. The corresponding LJ parameters are given in table 5.1.

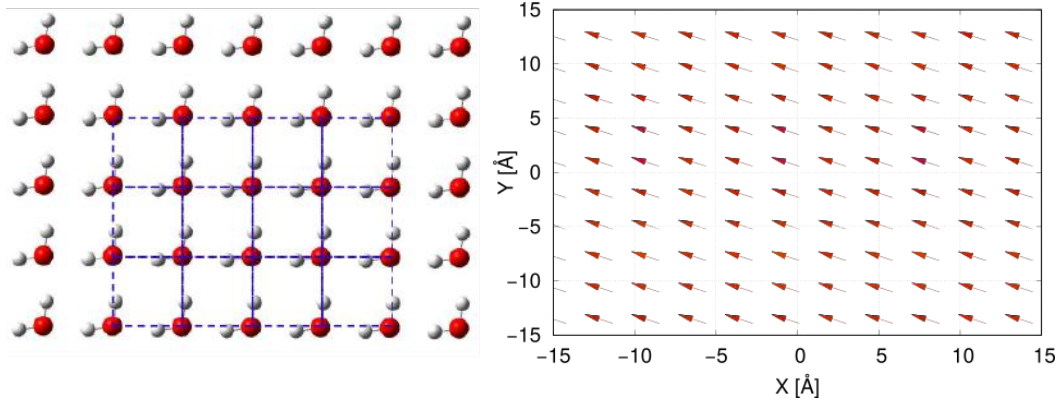


Figure 5.17 (lhs) A polar lattice of monolayer ice confined between two graphene layers which is about 10 meV/atom higher energy than the non-polar structure. (rhs) The corresponding local dipoles.

$B - O$		$N - O$	
σ_{BO} [Å]	ϵ_{BO} [eV]	σ_{NO} [Å]	ϵ_{NO} [eV]
3.3	$1.1 \cdot 10^{-2}$	3.2	$1.3 \cdot 10^{-2}$

Table 5.1 Parameters for the LJ potential between the h-BN layers and oxygen atoms [217].

A similar annealing scheme was performed as for graphene, starting with a temperature of 400 K, with a cooling rate of 8 K/ps and a damping constant of 0.1 ps. After annealing, the total energy is minimized using the iterative conjugate gradient (CG) scheme. For a distance of 5 Å between the h-BN layers, a similar flat ice crystal is found. The smaller channel width is due to the difference in the LJ parameters in our model for the C-O interaction and B-O & N-O interactions [217].

4.2 Bilayer square ice

Motivated by the experimental work of Algara-Siller et al [189] a bilayer of ice confined between two rigid graphene layers separated by $h = 9$ Å was investigated. The minimum energy structure is shown in Figs. 5.19(a,c). Surprisingly, also in this case the layers are flat (see Fig. 5.19(a)) and each has a perfect square lattice for the oxygen atoms (see Fig. 5.19(c)). Using the radial distribution function for each layer we found the lattice constant to be $a = 2.84 \pm 0.01$ Å. The radial distribution function for each ice layer is presented in Fig. 5.19(b) which are identical. The obtained angle ‘H–O–H’ is found to be $\theta = 106.15 \pm 0.02^\circ$. Each layer has a net dipole that is in the opposite direction with

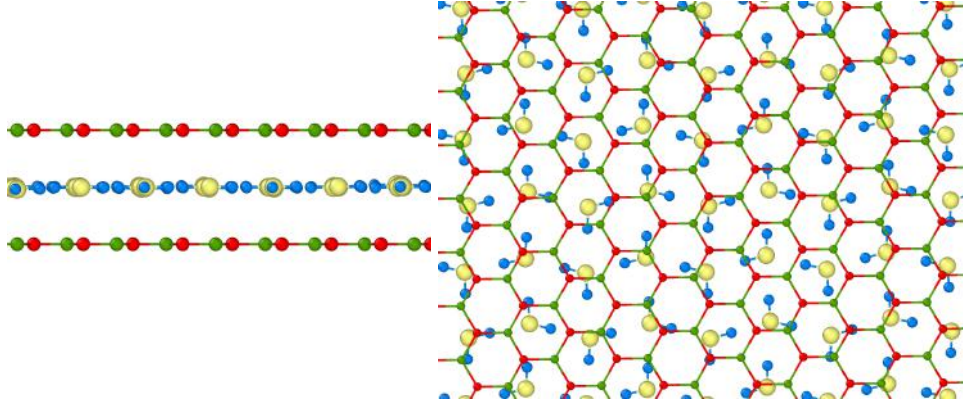


Figure 5.18 Side (lhs) and top (rhs) view of a relaxed ice monolayer between two h-BN layers. The red/green spheres indicate the positions of B/N atoms, while the yellow/blue spheres illustrate the position of the oxygen/hydrogen atoms in the water molecules.

respect to the other layer. The latter makes the bilayer of ice non-polar and non-ferroelectric. The interlayer distance between the ice layers is found to be $c = 3.24 \pm 0.01 \text{ \AA}$ which is in disagreement with the SPC/E model which obtained $a \cong c$ [189]. Our finding for ‘c’ is in the range of vdW adhesion between two ordinary neutral layers, e.g. the two graphene layers. The H-bonding energy is -0.14 eV .

The stacking of the two ice layers is not AA stacking nor is it AB stacked, i.e. the bottom layer has an in-plane shift of about 1.2 \AA (shown by the arrow in Fig. 5.19(c)) with respect to the top layer. The displacement of the O atoms with respect to each other is due to the fact that the O-atoms are negatively charged and thus repel each other. Note that the SPC/E model [189] predicts AB stacking for bilayer ice confined between two graphene layers. The TEM images in the recent experiment [189], which are shown by green circles in the bottom right part of Fig. 5.19(c), can be considered as the averaged positions of oxygen atoms in the top (red dots) and bottom layer (blue dots) of our results.

In order to investigate the importance of the interaction between ice and graphene and to present an independent test, we performed an additional MD minimization. We minimized the potential energy of monolayer ice with randomly distributed H-bonds (even out-of-plane) over a single layer of graphene at an initial distance of 3.0 \AA . The minimum energy configuration of ice is similar to Fig. 5.15 with the distance between graphene and ice of 2.90 \AA . This shows that the interaction between graphene and an ice layer is stronger than the interaction between two ice layers, which are separated by $c = 3.24 \text{ \AA}$ and the interaction between the two graphene layers even if they are at a distance of 9 \AA .

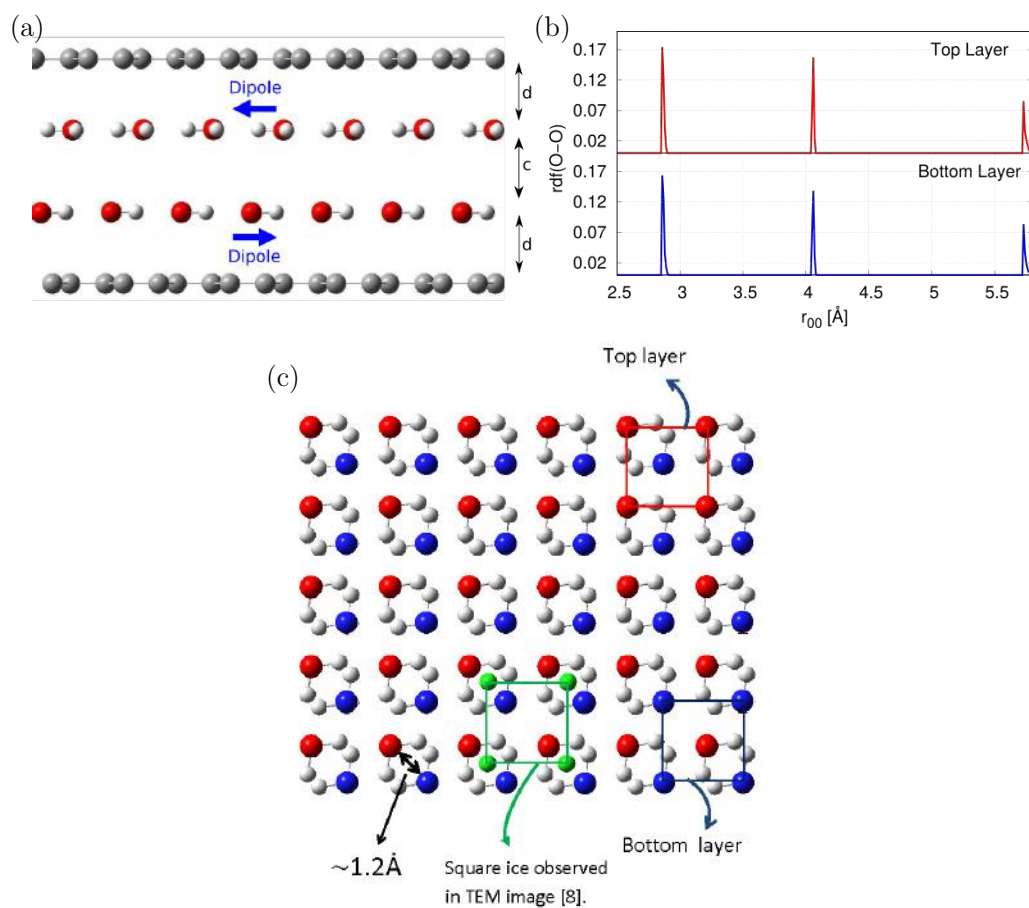


Figure 5.19 Relaxed bilayer ice between two graphene layers are shown in (a) side and (c) top view. In (b) the corresponding radial distribution function for O-O distances is shown. In the top view (c), the green dots refer to the TEM experiment [189]. The in-plane shift between top and bottom layer is about 1.2 Å.

	Minimum Energy Configuration			
	g.ice.g	g.ice.g (polar)	g.ice.ice.g	g.ice.ice.ice.g
$h[\text{\AA}]$	6.5	6.5	9	11.5
E [eV]	-3.87	-3.86	-3.83	-3.83
$E_{coulomb}$ [eV]	-1.71	-1.69	-1.76	-1.79
E_{VdW} [eV]	0.78	0.79	0.81	0.82
E_{HB} [eV]	-0.16	-0.14	-0.14	-0.16
$a = r_{oo}[\text{\AA}]$	2.84 ± 0.01	2.88 ± 0.01	2.84 ± 0.01	2.89 ± 0.02
$d[\text{\AA}]$	3.25 ± 0.01	3.25 ± 0.01	2.88 ± 0.01	2.70 ± 0.01
$c[\text{\AA}]$	0	0	3.24 ± 0.01	3.05 ± 0.01

Table 5.2 Different energy contributions (per atom, and for each hydrogen bond) and lattice parameters of the minimized energy configurations for mono (g.ice.g and g.ice.g (polar)), bilayer (g.ice.ice.g) and trilayer (g.ice.ice.ice.g) water confined between two graphene layers.

4.3 Trilayer ice

Finally, we turn our attention to the stacking and microscopic structure of confined three layer ice. By fixing two graphene layers at a distance $h = 11 \text{\AA}$ and performing annealing MD simulations, we found that each layer of the three layer ice is non-polar with a microscopic structure similar to that of monolayer ice (see Fig. 5.15(b)). The ice-graphene distance is found to be $d = 2.70 \pm 0.01 \text{\AA}$ and the distance between each of the ice layers is $c = 3.05 \pm 0.01 \text{\AA}$. H-bonding energy per water atom for the trilayer equals -0.16 eV, which is again identical as for the monolayer.

We found that it is energetically unfavourable to have an ice layer with a net dipole moment next to one with zero net polar moment. Therefore, we conclude that for an odd number of ice layers each layer has the structure of confined monolayer ice (each of them with a zero net dipole moment). However a system with an even number of ice layers confined between graphene will be comprised of pairs of layers where each pair has a structure like bilayer ice (Fig. 5.20).

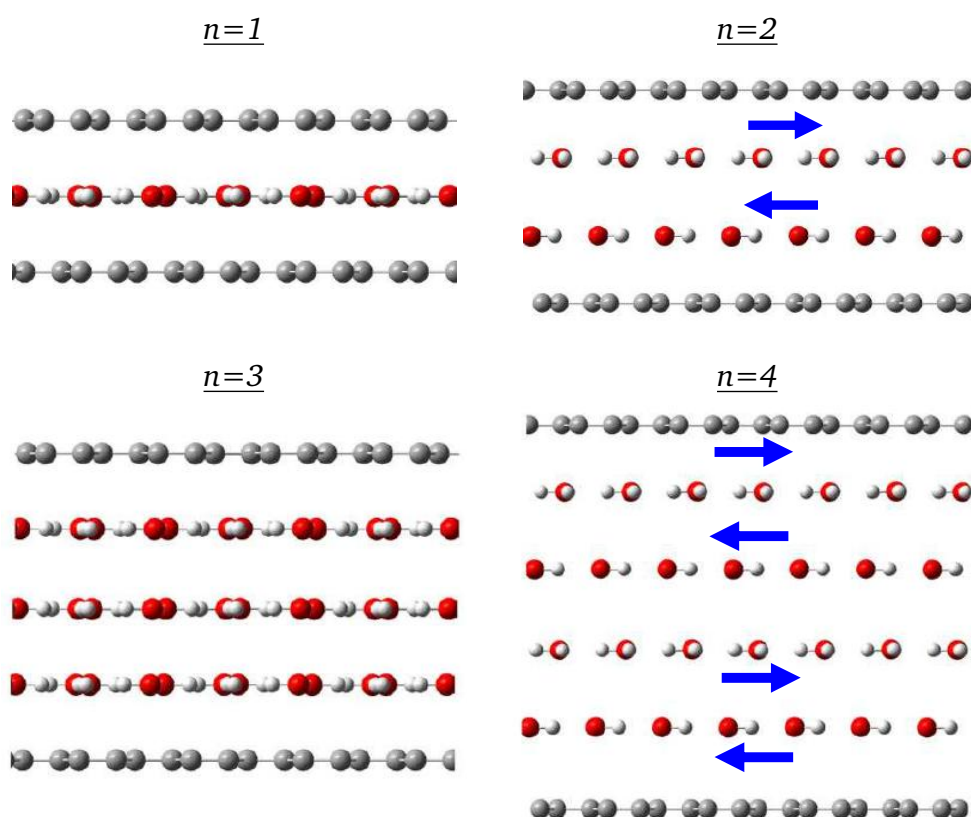


Figure 5.20 Multi-layer ice confined between graphene layers. The arrows indicate the net dipole moment in each layer.

5 Discussion and conclusions

In ordinary water the average distance between oxygen atoms is about 2.75 \AA and for each water molecule two hydrogen bonds (H-bonds) are randomly oriented resulting in an irregular network [215]. The H-bonds in liquid water have a life time of about $1 - 20 \text{ ps}$. Continuously bond formation and bond breaking takes place. The H-bonds are stronger in hexagonal bulk ice (ordinary ice) though the O-O distance is still 2.75 \AA but each water molecule takes part in four tetrahedrally-arranged H-bonds [215], i.e. forming a regular network with more room between the molecules yielding a lower density. Moreover, the strength and orientation of the H-bonds change when high pressure is applied. When water is confined between hydrophobic walls (here two graphene layers) in the presence of lateral pressure of about 1 GPa , monolayer ice is formed with an O-O distance of about

2.83 Å [189]. Therefore, the spacial orientation of the H-bonds and their strength and rearrangement is a key factor which determines the structure of water and the different phases of ice in confined monolayer and few layer ice.

In Table 5.2, different energy contributions of the different configurations are summarized. The Lennard-Jones interaction between oxygen atoms reaches its minimum at $\sigma_{OO} = 3.2$ Å [205]. The observed lattice constant of 2.83 Å lies in the repulsive area of the potential. In the confined ice layers under pressure, as well as in typical 3D ice structures (which have an even smaller lattice constant) the electrostatic attraction between H and O atoms dominates the repulsion between oxygen atoms.

The multiple configurations of ice at high pressures that meet the rules of absolute zero temperature amounts to randomness, or in other words, entropy which is called residual entropy. Therefore the ground state configuration of water either at zero temperature or high pressures strongly depends on the experimental procedure and details. The large degree of freedom for the hydrogen bond strength and its orientation gives the possibility to have several ice structures. This might be the reason for the observation of several different crystal structures as reported by different groups for confined ice using various methods [186, 189, 216].

This large degree of freedom is reduced when using a rigid molecular model in MD simulations which may result in incorrect lattice structures. In our case however, we find a layered structure which at zero temperature is an entropyleless structure. Three dimensional water ice is the first material for which residual entropy was proposed by Pauling [196]. By using MD simulations we showed that the Pauling proposal can be broken for a flat layer of ice.

For confined monolayer ice with a flat structure and zero net dipole moment the H-bonds should lie in the same plane. However, flat ice layers in non-polar bilayer of ice nucleates as a square lattice with a configuration between AA and AB stacking. We predict that an odd (even) number of ice layers are stacks of monolayer (bilayer) ice. We found that the interaction between ice layers is weaker than that between ice and graphene which results in a shorter distance between ice and graphene.

CHAPTER 6

Electric field induced structural changes of water confined between two graphene layers

Whether or not there exists a phase of ice with a net molecular dipole moment is an old question which is closely related to the debate on the existence of ferroelectricity in ice. It remains highly controversial because of the absence of both theoretical and experimental studies on the microscopic structure of water in the presence of an electric field. There is experimental evidence that at least partial ferroelectric alignment can be induced in normal ice, either by interaction with a substrate [218, 219] or by doping with impurities [220]. Su *et al.* [219] found ultra-thin hexagonal films of water covering a substrate (1-10 monolayer thick) with a net dipole moment. Ferroelectricity is expected to appear in the ordered phase of ice where the hydrogen bonds (H-bonds) are aligned uniformly [221]. Importantly, when reducing the degrees of freedom of the H-bonds the system becomes more ordered. The ferroelectricity of monolayer ice was studied by several groups which found conflicting results, e.g. hexagonal and flat/rippled rhombic phases were found to be ferroelectric by Zhao *et al* [216]. This ordered phase has a net dipole. However many other studies reported a disordered phase with zero net dipole moment [186, 222, 223]. An external electric field, should in principle, reorient the local dipoles of water. However because of the random distribution of the dipoles in ordinary water, the strength of the electric field should be sufficiently strong ($\geq 0.1 \text{ V/\AA}$) to disrupt the network of molecules in liquid water [224] and to change the equilibrium freezing point of water. Depending on the value of the electric field, the external pressure may cause melting or freezing of water [225].

An external electric field changes the physical properties of polar-liquids due to the reorientation of their permanent dipoles. Using molecular dynamics simulations, we predict that an in-plane electric field applied parallel to the channel polarizes water molecules which are confined between two graphene layers, resulting in distinct-ferroelectricity and electrical hysteresis. We found that electric fields alter the in-plane order of the hydrogen bonds: reversing the electric field does not restore the system to the non-polar initial state, instead a residual dipole moment remains in the system. The square-rhombic structure of 2D-ice is transformed into two rhombic-rhombic structures. Our study provides insights into the ferroelectric state of water when confined in nanochannels and shows how this can be tuned by an electric field.

This chapter extends the study of an ice monolayer in a graphene nanocapillary by including an in-plane electric field. In the first section, a condensed introduction is given, where the effects of an electric field on confined water in different systems are discussed. After which the model from previous Chapter 5 is recapitulated. In order to investigate the ferroelectric properties of a monolayer ice, the total dipole moment of the lattice is calculated as a function of the applied electric field. Section 3 is dedicated to the results of these calculations. Finally, our conclusions are given in Sec. 4. Results presented in this chapter have partially been published in Ref. [226].

1 Introduction

As was seen in the previous chapter, the confinement of water near surfaces or inside nanoscale geometries results in an altered phase behaviour, which differs substantially from bulk systems. When an external electric field is applied these systems, different effects occur depending on the type of confinement: they may for example cause melting, freezing or induce other structural transitions [108].

When an electric field is applied to an ice sample, two distinct physical processes occur. Firstly, the individual molecules are polarized by the external field. This involves displacements of the electrons relative to the nuclei and small distortions of the molecular order. These are effects which occur in all materials and their response of to a change in field is very rapid ($< 10^{-3}$ ns [227]), so that these effects are mostly independent of the frequency of the field. In a second stage, ice polarizes by a reorientation of molecules and their hydrogen bonds. In Sec. 1.1 we discussed the ice rules and the zero-point entropy of ice lattices. When placed in an electric field, the energies of some of the hydrogen bond configurations (that are compatible with the ice rules) are lowered relative to other configurations, so that in thermal equilibrium ice layers should have a net polarization. This is a dynamical process, in which hydrogen bonds need to brake and reattach in combination with the repositioning of individual molecules requiring thermal activation and local violations of the ice rules. Once a single or a small cluster water molecule switches to the polarized equilibrium state, the configuration of neighbouring molecules (that have lost their fully hydrogen bonded state) will increasingly lose their stability, resulting in avalanche like dynamics that spread over the entire system. In Chapter 5 a polar monolayer ice was found with a higher energy than the non-polar structure. When an external field is applied to the system, we can expect to find a polar ground state configuration.

For the small isolated water clusters that were discussed in Sec. 1.1.1 a uniform electric field with strengths in the range of $E \leq 0.6$ V/Å results in morphological shifts. After a tilting of the free hydrogen atoms towards the direction of the field, the oligomers form longitudinal chains with noticeable jumps in the internal energy and dipole moment during an extensive structural reorganization where hydrogen bonds need to break to enable the cluster to stretch along the direction of the field.

For bulk water previous studies have found that an electric field alters its physical properties such as the surface tension and vaporization enthalpy. Both properties increase under the influence of the field, from which it has been suggested that the electric field breaks certain hydrogen-bonds, resulting in clusters composed of smaller substructures for which the remaining hydrogen-bonds are stronger [228]. At 3 – 4 V/Å water is found to crystallize into an ordered, ice like structure stabilized through hydrogen bonds [229, 230].

In contrast, the buckled ice monolayer between two quartz plates that was previously shown in Fig.5.11, can melt into liquid water under a perpendicularly applied electric field with $E = 0.5 \text{ V/\AA}$. The melting temperature of the monolayer decreases with increasing strength of the external field due to the field-induced disruption of the well-ordered hydrogen bond network [231]. At high external fields ($E \geq 3.5 \text{ V/\AA}$) a two-layered crystal-like water phase is recovered. These results are summarized in Fig. 6.1 in which the in-plane diffusion coefficient is given at different electric field strengths.

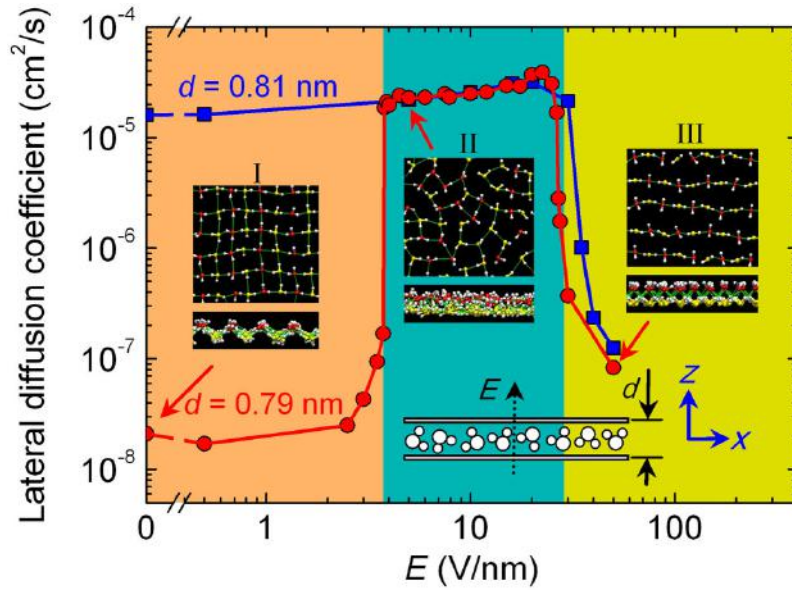


Figure 6.1 In-plane diffusion coefficient of water at 300 K as a function of the external electric field (E) at two inter-plate distances. The top insets show the in-plane and out-of-plane views of (I) an ice monolayer at $E = 0$, (II) a liquid water phase at $E = 5 \text{ V/nm}$, and (III) a crystal-like water phase at $E = 50 \text{ V/nm}$. The bottom inset schematically shows the simulation setup (adapted from Ref [231]).

Recently, it was proposed that confined water exists as a quasi-two-dimensional layer with different properties than those of bulk water [188, 189], however this observation was challenged later [211]. Graphene, the two-dimensional allotrope of carbon [35], was used in the experiment to confine water [189] into monolayer, bilayer and trilayer. In the previous chapter we showed that flat monolayers of ice exists between two graphene layers. Here we will address the effects of an electric field on such a monolayer of ice. The microscopic details of the orientation of the H-bonds is investigated and provides insights in the response of ice to an electric field.

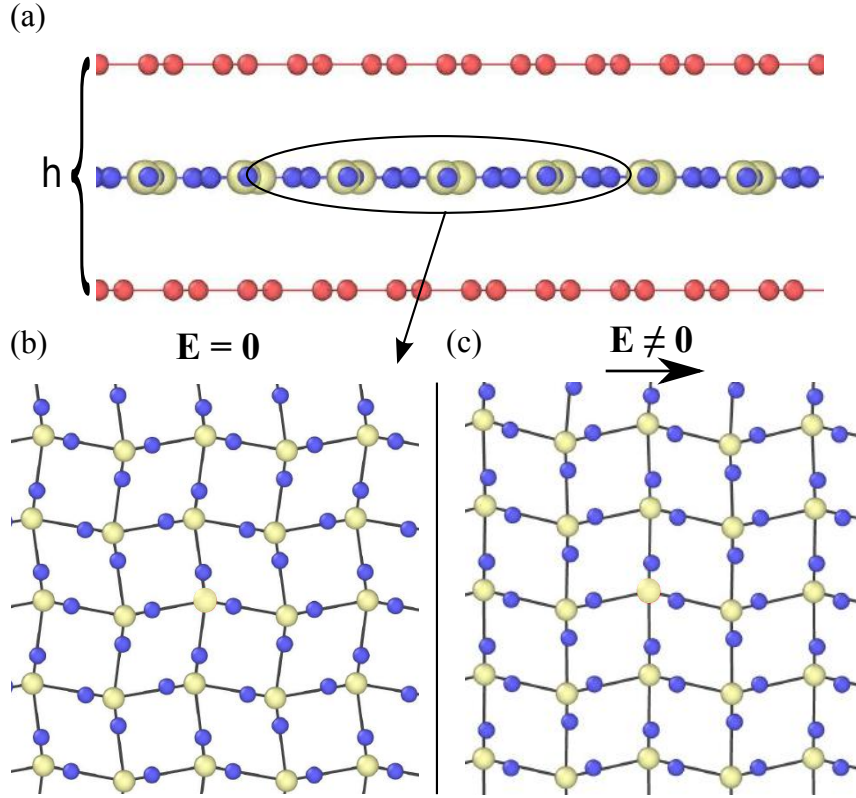


Figure 6.2 Side (a) and top (b) view of a relaxed square-rhombic monolayer of ice between two graphene layers, and the flat rhombic-rhombic monolayer (c) when an external electric field is applied.

2 Method and model

In our MD simulations (using LAMMPS [232, 233]) we used the reactive force-field ReaxFF [48], a general bond-order dependent potential that provides an accurate description of chemical bonds and reactions. This is in contrast with traditional force fields for water, e.g. SPC and TIP4P [214].

The computational unit cell is a square with dimension 283×163^2 that contains 34848 carbon atoms and is filled by 17100 water molecules. We start from a dense square structure of O atoms with a lattice constant of 2.8 \AA and a random distribution of H-bonds. The monolayer of water is confined between two graphene layers and interaction with the C-atoms is fully taken into account. We performed an annealing MD simulation using NPT starting at 400 K and ending at 0 K, in order to find the true simulation box size and O-O distances. The total energy is minimized using the iterative conjugate gradient (CG) scheme. The graphene layers are rigid and separated by a fixed distance (h)

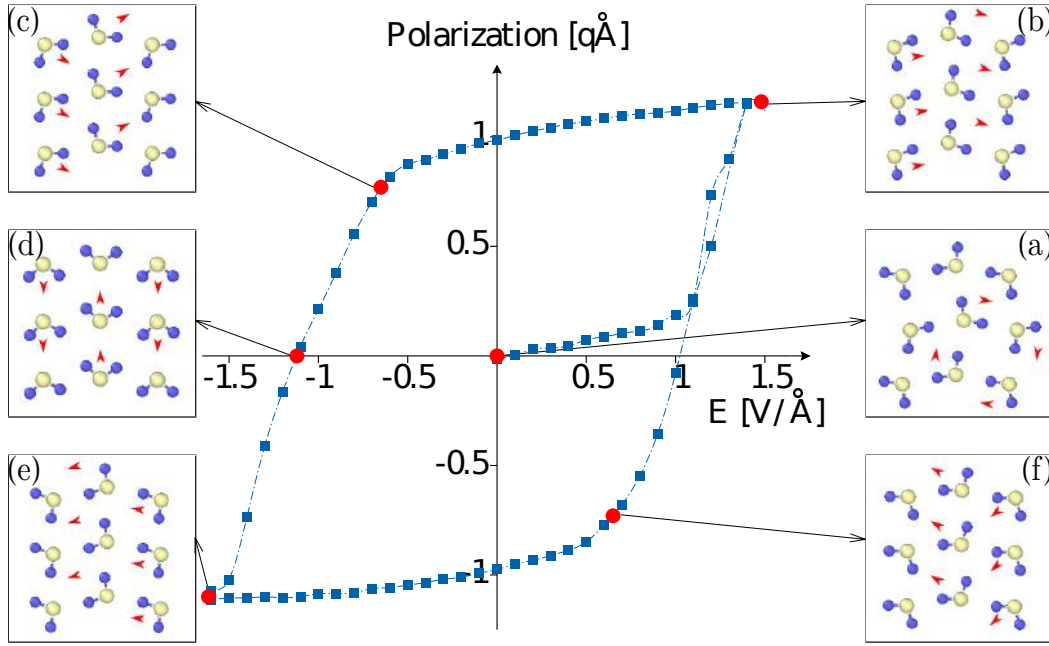


Figure 6.3 Hysteresis curve of the net polarisation (in units of electron charge times Å) of water confined between two graphene layers separated by $h=6.5$ Å. The insets show the structure of monolayer ice for six specific cases. The electric field was varied with a rate of 12.5 GHz.

having AB-stacking. The dimensions of the unit cell is important when studying the bulk behaviour of flat ice. When applying periodic boundary conditions (PBCs) the periodicity of the ice crystal has to be commensurable to the graphene lattice, i.e. the integers m and n must be chosen accordingly to the lattice constants (a_{CC}, a_{OO}) so that $ma_{CC} = na_{OO}$.

In order to investigate the ferroelectric properties of monolayer ice confined between two graphene sheets, we measure the total dipole moment by summing over all local dipoles ($\vec{P}_{total} = \sum_n \vec{p}_n$) in the presence of an external in-plane electric field in the zig-zag direction (see Fig. 6.2(c)).

3 Results

3.1 Square-rhombic lattice for 2D-ice confined between two hydrophobic layers when $E=0$

Using the reactive force-field (ReaxFF [48]), we confirmed that the minimum energy configuration of a flat monolayer ice confined between two graphene layers separated by 6.5 Å is a non-polar ordered

phase consisting of a combination of rhombic and tilted square lattice structure (see Fig. 6.2). The radial distribution function (RDF) shows that the O-O distance in flat ice is about $a=2.84\pm0.01$ Å which is in good agreement with the experimental value of $a=2.81\pm0.02$ Å [189]. This structure satisfies the ice rule while it is flat, ordered and non-polar. We study the response of such a monolayer ice to an external in-plane electric field. We found that an electric field of about 1 V/Å rotates the H-bonds, and reorients the dipoles changing the structure of monolayer ice. By reversing the electric field direction we found irreversibility in both the structure and the polarization of the system.

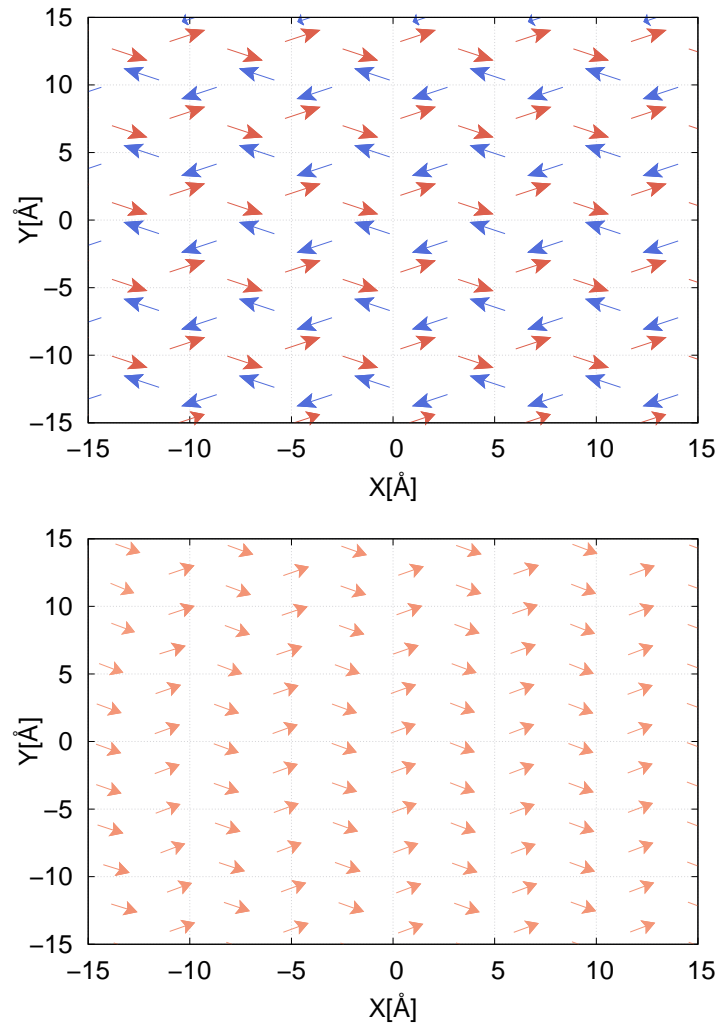


Figure 6.4 Arrows indicate the local dipoles in a monolayer of water confined between two graphene layers for (a) a non-polarised state, and (b) at the saturation polarisation.

3.2 Rhombic-rhombic lattice for confined 2D-ice when $E \neq 0$

By changing the electric field in the range $[-1.5, 1.5]$ V/Å we found hysteretic behaviour which for $h = 6.5$ Å is shown in Fig. 6.3. Due to the electric dipole moments of water molecules, the associated field strengths are extremely large, and not directly accessible in the laboratory. The experimentally attainable DC electric fields on bulk water have been reported several orders of magnitude weaker than the simulated fields, i.e. $\approx 10^{-2}$ V/Å [234]. They are however in line with the fields strength that have been previously reported for structural transitions in ice layers and electro-freezing experiments [183, 230, 235].

In the insets of Fig. 6.3 the corresponding ice structures for six special states are depicted. Inset (a) shows the minimum energy configuration of a monolayer of water (Fig. 1). By increasing the electric field the system becomes polarized and one naturally expects that the local dipoles orient along the direction of the external field. A linear response of \vec{P} to the external field is found before a significant jump in \vec{P} , i.e. $\vec{P} \propto \chi E$ for $0 \leq E < 1$ V/Å with $\chi = 0.20$ qA^2/V which is lower than the susceptibility of bulk ice. However, such a complete alignment does not occur in monolayer ice because of the local dipole-dipole interaction as well as the strong (mostly Coulomb) interaction between the neighbours. The minimum energy is determined by a competition between the external electric field and the local arrangement of the dipoles. In the inset (b) the water configuration is shown near the saturation point P_s . Two columns are visible for which the perpendicular dipole orientation is opposite, reminiscent of H-bonds between neighbouring water molecules. By comparing Fig. 6.3(a) with the other subsets (Figs. 6.3(b,c,...)), we find that the oxygen atoms align in the perpendicular direction of the field and that the square-rhombic structure is transformed into a rhombic-rhombic structure (see Fig. 6.2(c) for a detailed view of the structure). When decreasing the electric field after reaching the saturation point, the system retains a large fraction of polarization until a critical field is reached ($+P_r$). Here, the system reacts similar to a 2D Ising model: it relaxes through avalanche-like dynamics shown in the insets (c-d-e). We conclude that due to the presence of H-bonds, a larger electric field is needed to rotate the H-bonds and there is no significant change in the location of the oxygen atoms.

3.3 Electric hysteresis of confined 2D-ice

By changing the electric field as seen from the insets there are two distinguishable lines of water molecules with a different orientation of the local dipoles. At the coercitivity points $\pm E_c$ the local dipoles in two adjacent columns are in opposite directions which results in a zero net dipole moment. We can conclude that electric fields < 2 V/Å are weak enough to change the position of O atoms. Changing the position of O atoms demands a larger electric field which deforms the ice structure.

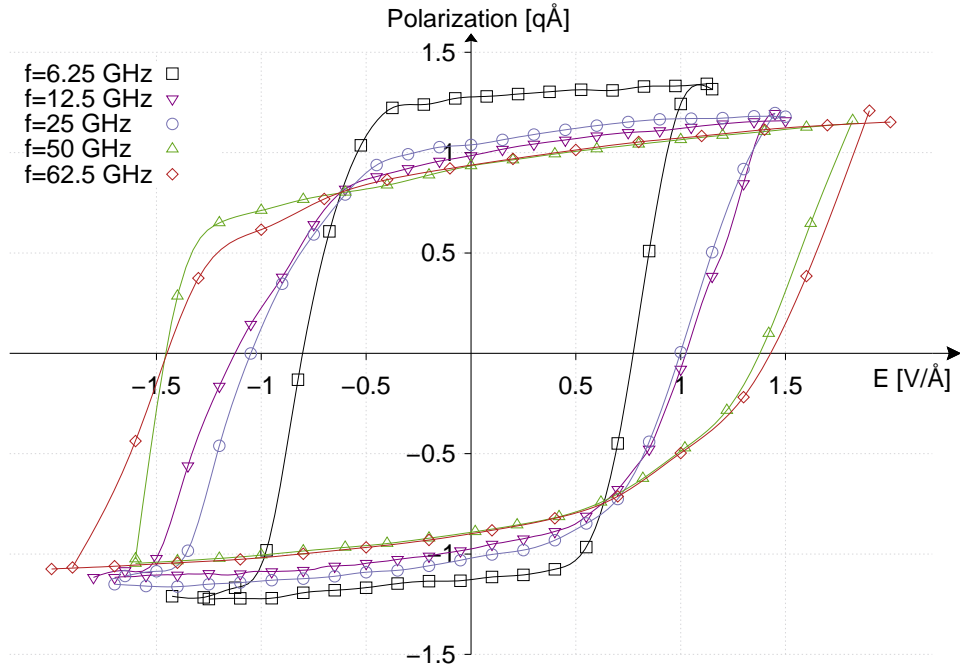


Figure 6.5 Hysteresis loop of the polarization of an ice monolayer confined between two graphene sheets for different frequencies of the applied electric field.

It is well known that hysteresis effects are related to the starting configuration and gives a time dependent output. Therefore we expect that by changing the rate (frequency) at which the electric field is varied we obtain different hysteresis loops. The electric field is varied linear in time between -2 V/Å and $+2 \text{ V/Å}$ with different rates “ f ”. In figure 6.5 we performed several additional simulations using different values of the frequency of the external field. For instance the frequency $f = 12.5 \text{ GHz}$ corresponds to the situation which was shown in more detail in Fig. 6.3. It is important to note that changing the frequency of the external field does not effect the morphology of the structures, it influences only the rate at which the changes take place. The system reaches its highest saturation and remnant polarization for the slowest input rate of 6.25 GHz . By increasing the frequency these values gradually decreases, and the critical field for which the system switches its polarization is increased. There are three parameters that characterises each loop: the field E_c at zero dipole moment, the remnant polarization P_r and the saturation polarization P_s which are listed in Table 6.1. From this table we see that there are different frequency ranges for which the polarization process are rather similar. In general we can conclude that the saturation polarization for higher frequencies lowers ($E_c \propto (1/f)$), and that the driving electric field must be increased to a larger value

before the system switches between polarized states. In Fig. 6.4(a) the local dipoles are shown for the polarized state (see inset (a) in Fig. 6.3 for the corresponding orientation of the water molecules). The local dipole moment of each molecule is compensated by molecules at the opposite vertex of the lattice. When applying an external field this symmetric arrangement is no longer preserved, and we find a new structure as shown in Fig. 6.4(b). Here we find columns of similar orientation in the lateral direction of the electric field, with the total dipole moment averaging out in the direction of the external field. To preserve the H-bonds in the rhombic lattice, the individual dipolar molecules never fully align themselves with the external field. Only when increasing the strength of the external field to $\pm 3 \text{ V/\AA}$, there is a transition to a triangular lattice where all the local dipoles point in the direction of the field.

$f [\text{GHz}]$	$P_s [q\text{\AA}]$	$P_r [q\text{\AA}]$	$E_c [V/\text{\AA}]$
6.25	1.28 ± 0.02	1.20 ± 0.02	0.79 ± 0.02
12.5	1.15 ± 0.03	0.98 ± 0.02	1.05 ± 0.06
25	1.17 ± 0.04	1.02 ± 0.02	1.03 ± 0.06
50	1.10 ± 0.02	0.91 ± 0.05	1.43 ± 0.02
62.5	1.12 ± 0.02	0.92 ± 0.05	1.47 ± 0.02

Table 6.1 Characteristic hysteresis parameters for different frequencies: Coercive field (E_c), remnant polarization (P_r), and saturation polarization (P_s).

3.4 Energetic considerations

For all studied h values, confined ice has the same energy threshold value for which it responds to the external field and passes from one metastable state to another. When increasing the rate of the external field, this barrier increases. The potential energy of the system is shown in Fig. 6.6(a). We find that the energy oscillates with the same frequency as the electric field and that for all given rates, a large jump in energy is visible around the field for which the system switches its polarization. For high frequency fields, the energy of the remnant state is closer to the initial configuration. The van der Waals energy is shown in Fig. 6.6(b). Here, the tension on the dipoles created by switching the polarity of the field is clearly visible. Notice the second and third minima in the energy (where $E \neq 0$) are larger than the first minimum (where $E = 0$). The vdW energy reaches a minimum when we reach a maximum alignment of the local dipoles, which is at the saturation point (end of domains (1,2,3) in

Fig. 6.6(b)). Comparing this result with structures found in 6.3 we see that here the H-bonds between neighbouring atoms is the strongest. When reaching the critical field, the H-bonds are weakened as the individual columns rotate towards a perpendicular alignment with the electric field. The eventual cascade towards a switched polarization is prolonged for higher frequencies as the transition lags behind the external field, and the vdW energy reaches larger values for these systems.

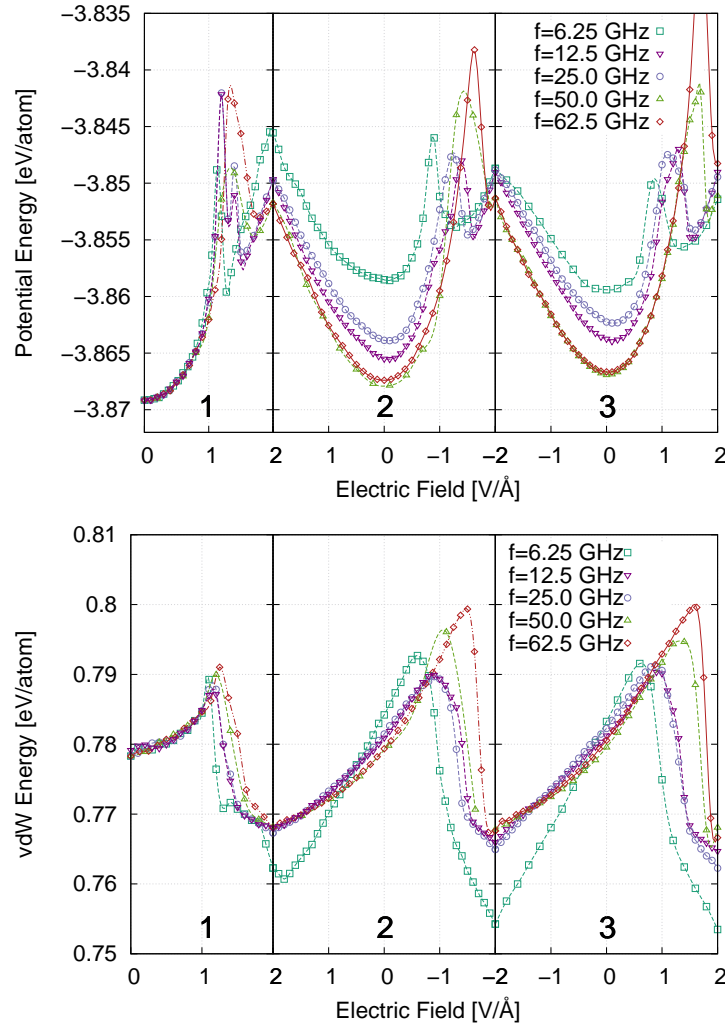


Figure 6.6 Potential (a) and van der Waals (b) energy as function of applied electric field for different frequencies of the electric field. Three domains in (a) and (b) refer to three different steps: (1) increasing the dipole starting from a zero field value, (2) lowering the external field up to $\simeq -1.5$ V/Å, and (3) increasing the external electric field up to $\simeq +1.5$ V/Å.

4 Discussion and conclusions

Ferroelectric materials are used in many areas of science and technology which are a special class of piezoelectrics showing a large piezoelectric response. Ferroelectricity of confined water is largely unknown because of the lack of experiments. The control of dipoles in water, its description and understanding of electromechanical (piezoelectric) and ferroelectric hysteresis helps to understand the fundamental properties of confined water and its fluidity [236]. Recently there have been several experimental attempts to produce confined monolayer ice and to study confined water in a hydrophobic channel [189]. Here theoretically we obtained the minimum energy configuration for confined ice and its irreversibility response to an in-plane electric field. We found that the minimum energy configuration is not a square lattice structure. An in-plane electric field rotates the H-bonds and makes monolayer ice polarized without losing the flatness of monolayer ice. However, by reversing the field the system reaches a higher energy state. The higher energy configuration mostly consists of two rows of dipoles whose moment cancel each other when the electric field is $\pm E_c$. Therefore, monolayer ice oscillates between two ordered phases with opposite polarity (Fig. 6.3(b-e)) when an alternating electric field is applied. Independent of the applied electric field all structures remain almost flat. This electromechanical coupling might be responsible for some unusual phenomena in confined ice.

In summary using reactive molecular dynamics, we studied systematically the response of monolayer ice to an external in-plane electric field. The structural change, the vdW and the H-bonding energy were calculated for such a monolayer of ice. We discovered electrical hysteresis in this system, where the net dipole moment of the system changes irreversibly with the electric field. During this process the system remains flat, oxygen atoms move slightly in-plane to form a rhombic-rhombic lattice instead of the original square-rhombic lattice. The microscopic details that we addressed here for the response of a two-dimensional ice lattice to an external electric field is helpful in understanding the response of other structures of ice to an external electric field. We believe that this finding will motivate experimentalists to realize the proposed effect and reveal many unexplored issues of confined ice.

Part IV

Appendices

APPENDIX A

Formal deviation of the Velocity Verlet algorithm

1 Discretisation of the Liouville operator

In Sec. 3 we introduced the numerical integration scheme of the Verlet algorithm in a heuristic way, using a Taylor expansion as a mean to generate the update procedure. In this Appendix, a more formal structure is presented in which we can show that the Verlet algorithm is symplectic, and is a solution of an approximation of the true Hamiltonian. The deviation that will be presented here is largely based on the the work of M.E. Tuckerman in [57]. In this Appendix we will use the canonical coordinate notation $\mathbf{x} = (\mathbf{q}(t), \mathbf{p}(t))$ for the set of positions and impulses at a time-step t .

Consider the time evolution of any function of the phase space vector $a(\mathbf{x})$. If $a(\mathbf{x})$ is evaluated along some trajectory \mathbf{x}_t , we can write down the time derivative of $a(\mathbf{x}_t)$ using the chain rule:

$$\frac{da}{dt} = \sum_{\alpha=1}^{3N} \left[\frac{\partial a}{\partial q_{\alpha}} \dot{q}_{\alpha} + \frac{\partial a}{\partial p_{\alpha}} \dot{p}_{\alpha} \right]. \quad (\text{A.1})$$

Using Hamilton's equations:

$$\dot{q}_{\alpha} = \frac{\partial \mathcal{H}}{\partial p_{\alpha}} \qquad \dot{p}_{\alpha} = -\frac{\partial \mathcal{H}}{\partial q_{\alpha}}, \quad (\text{A.2})$$

we can rewrite the time derivatives in Eq. (A.1) as

$$\begin{aligned}\frac{da}{dt} &= \sum_{\alpha=1}^{3N} \left[\frac{\partial a}{\partial q_{\alpha}} \frac{\partial \mathcal{H}}{\partial p_{\alpha}} - \frac{\partial a}{\partial p_{\alpha}} \frac{\partial \mathcal{H}}{\partial q_{\alpha}} \right] \\ &= \{a, \mathcal{H}\},\end{aligned}\tag{A.3}$$

using the Poisson bracket notation in the last line.

With this notation in place we can introduce an operator that acts on a phase space function a

$$iLa = \{a, \mathcal{H}\},\tag{A.4}$$

and formally solve the time evolution of $a(\mathbf{x})$

$$a(\mathbf{x}_t) = e^{iLt} a(\mathbf{x}_0).\tag{A.5}$$

The operator L is known as the *Liouville* operator. It can be written as a differential operator:

$$\sum_{\alpha=1}^{3N} \left[\frac{\partial \mathcal{H}}{\partial p_{\alpha}} \frac{\partial}{\partial q_{\alpha}} - \frac{\partial \mathcal{H}}{\partial q_{\alpha}} \frac{\partial}{\partial p_{\alpha}} \right].\tag{A.6}$$

In Eq. (A.5) the operator e^{iLt} takes the form of a classical propagator, which strongly resembles the quantum propagator $e^{-i\hat{H}t/\hbar}$ and is the reason why the i is formally added in Eq. (A.4).

Applying Eq. (A.4) to the phase space vector $a(\mathbf{x}) = \mathbf{x}$, we find a solution to Hamilton's equations:

$$\mathbf{x}_t = e^{iLt} \mathbf{x}_0\tag{A.7}$$

Eq. (A.7) is nothing more than a compact notation of our original problem, and does very little in actually solving the time evolution, as we cannot evaluate the action of the operator $\exp(iLt)$ on x_0 exactly. It does provide a useful starting point for developing approximate solutions to Hamilton's equations. We will use Eq. (A.7) to show that the Verlet algorithm that was introduced in Sec. 3 is a solution to an approximation of the true Hamiltonian of the system by looking at the evolution of the phase space of a one-dimensional Hamiltonian of the form:

$$\mathcal{H} = \frac{p^2}{2m} + U(x).\tag{A.8}$$

Let's revisit the definition of the Liouville operator in Eq. (A.6) which can be written as the sum of two contributions:

$$iL = iL_1 + iL_2.\tag{A.9}$$

For the Hamiltonian defined in Eq. (A.8):

$$\begin{aligned} iL_1 &= \frac{p}{m} \frac{\partial}{\partial x} \\ iL_2 &= F(x) \frac{\partial}{\partial p}. \end{aligned} \quad (\text{A.10})$$

The commutation relation between these two operators

$$[iL_1, iL_2] = iL_1 iL_2 - iL_2 iL_1, \quad (\text{A.11})$$

can be found by looking at its effect to any given function $\phi(x, p)$ of the phase space of Eq. (A.8).

The action of taking $iL_1 iL_2$ on a function $\phi(x, p)$ equals

$$\frac{p}{m} \frac{\partial}{\partial x} F(x) \frac{\partial}{\partial p} \phi(x, p) = \frac{p}{m} F(x) \frac{\partial^2 \phi}{\partial p \partial x} + \frac{p}{m} F'(x) \frac{\partial \phi}{\partial p}, \quad (\text{A.12})$$

and similarly for $iL_2 iL_1$

$$F(x) \frac{\partial}{\partial p} \frac{p}{m} \frac{\partial}{\partial x} \phi(x, p) = F(x) \frac{p}{m} \frac{\partial^2 \phi}{\partial p \partial x} + F(x) \frac{1}{m} \frac{\partial \phi}{\partial x}, \quad (\text{A.13})$$

so that

$$[iL_1, iL_2] = \frac{p}{m} F'(x) \frac{\partial}{\partial p} - \frac{F(x)}{m} \frac{\partial}{\partial x}. \quad (\text{A.14})$$

Because iL_1 and iL_2 do not commute, we can not easily separate the classical propagator $\exp(iLt)$ as $\exp(iL_1 t) \exp(iL_2 t)$. Which is unfortunate, as the individual operators $\exp(iL_1 t)$ and $\exp(iL_2 t)$ on the phase space vector can be evaluated exactly. It is almost possible to separate the two terms appearing in the propagator using an important theorem known as the *symmetric Trotter theorem* [237]:

$$e^{A+B} = \lim_{m \rightarrow \infty} \left(e^{B/2m} e^{A/m} e^{B/2m} \right)^m. \quad (\text{A.15})$$

for which a proof is given in Appx. 3. Applying the Trotter factorization to the classical propagator

$$e^{iLt} = e^{(iL_1 + iL_2)t} = \lim_{m \rightarrow \infty} \left(e^{iL_2 t/2m} e^{iL_1 t/m} e^{iL_2 t/2m} \right)^m, \quad (\text{A.16})$$

can be written down more suggestively by defining a time step $\Delta t = t/m$ which yields

$$e^{iLt} = \lim_{m \rightarrow \infty, \Delta t \rightarrow 0} \left(e^{iL_2 \Delta t/2} e^{iL_1 \Delta t} e^{iL_2 \Delta t/2} \right)^m. \quad (\text{A.17})$$

Eq. (A.17) indicates that the propagation can be solved exactly for a finite t if the number of time steps goes to infinity. This is not very practical, as we are interested in defining a numerical integrator. For a small (but finite) Δt , we can write

$$e^{iL\Delta t} \approx e^{iL_2\Delta t/2} e^{iL_1\Delta t} e^{iL_2\Delta t/2} + \mathcal{O}(\Delta t^3). \quad (\text{A.18})$$

Using this form, we can see how a single particle moves, by filling in the two contributions to the Liouville operator that was given by Eq. (A.10):

$$\exp(iL\Delta t) \approx \exp\left(\frac{\Delta t}{2}F(x)\frac{\partial}{\partial p}\right) \exp\left(\Delta t\frac{p}{m}\frac{\partial}{\partial x}\right) \exp\left(\frac{\Delta t}{2}F(x)\frac{\partial}{\partial p}\right). \quad (\text{A.19})$$

Which can now be used to solve the formal solution that was given in Eq. (A.7)

$$\begin{pmatrix} x(\Delta t) \\ p(\Delta t) \end{pmatrix} \approx \exp\left(\frac{\Delta t}{2}F(x)\frac{\partial}{\partial p}\right) \exp\left(\Delta t\frac{p}{m}\frac{\partial}{\partial x}\right) \exp\left(\frac{\Delta t}{2}F(x)\frac{\partial}{\partial p}\right) \begin{pmatrix} x \\ p \end{pmatrix} \quad (\text{A.20})$$

The last tool that is needed is how to apply these exponential operators. Let's see how the operator $\exp(c\partial/\partial x)$ acts on an arbitrary function $g(x)$:

$$\begin{aligned} \exp\left(c\frac{\partial}{\partial x}\right)g(x) &= \sum_{k=0}^{\infty} \frac{1}{k!} \left(c\frac{\partial}{\partial x}\right)^k g(x) \\ &= \sum_{k=0}^{\infty} \frac{1}{k!} c^k g^{(k)}(x), \end{aligned} \quad (\text{A.21})$$

which is the Taylor expansion of $g(x+c)$ about $c=0$. Now we can use this result

$$\exp\left(c\frac{\partial}{\partial x}\right)g(x) = g(x+c), \quad (\text{A.22})$$

to evaluate actions of the operators in Eq. (A.20). For the first operator we find that

$$\exp\left(\frac{\Delta t}{2}F(x)\frac{\partial}{\partial p}\right)\begin{pmatrix} x \\ p \end{pmatrix} = \begin{pmatrix} x \\ p + \frac{\Delta t}{2}F(x) \end{pmatrix}. \quad (\text{A.23})$$

The second operator acts on the x appearing in both components of the vector on the right side of Eq. A.23:

$$\exp\left(\Delta t\frac{p}{m}\frac{\partial}{\partial x}\right)\begin{pmatrix} x \\ p + \frac{\Delta t}{2}F(x) \end{pmatrix} = \begin{pmatrix} x + \Delta t\frac{p}{m} \\ p + \frac{\Delta t}{2}F(x + \Delta t\frac{p}{m}) \end{pmatrix}. \quad (\text{A.24})$$

Finally, the action of the third operator can be evaluated as:

$$\exp\left(\frac{\Delta t}{2}F(x)\frac{\partial}{\partial p}\right)\left(x + \Delta t\frac{p}{m}\right) = \quad (\text{A.25})$$

$$\quad (\text{A.26})$$

$$\left(x + \frac{\Delta t}{m}\left(p + \frac{\Delta t}{2}F(x)\right)\right) \quad (\text{A.27})$$

In which we can recognize the velocity Verlet algorithm. When writing p/m as v , we see that:

$$x(\Delta t) = x + \Delta t v + \frac{\Delta t^2}{2m}F(x), \quad (\text{A.28})$$

which is exactly the position update part of the Verlet algorithm. Velocities are updated as:

$$v(\Delta t) = v + \frac{\Delta t}{2m}[F(x) + F(x(\Delta t))] \quad (\text{A.29})$$

The above analysis demonstrates how we can retrieve the velocity Verlet algorithm using the Trotter factorization scheme. In the limit of $\Delta t \rightarrow 0$, classical mechanics is recovered. For any finite Δt , the classical Hamiltonian will be distorted by a factor $\mathcal{O}(\Delta t^3)$ (see Eq. (A.18)). For this *shadow Hamiltonian* the velocity Verlet algorithm is a symplectic, unitary, time-reversible propagation scheme that preserves important symmetries of classical mechanics.

2 Shadow Hamiltonian

In Appx. 1 the Trotter factorization scheme was used to express the classical propagator as the product of an operator corresponding $\frac{\partial}{\partial x}$ and $\frac{\partial}{\partial p}$ (see Eq. (A.18)). This factorization was only an approximation of the classical propagator. However, there is a formal relation that connects the two propagators:

$$\exp\left[iL_2\frac{\Delta t}{2}\right]\exp[iL_1\Delta t]\exp\left[iL_2\frac{\Delta t}{2}\right] = \exp\left[\Delta t\left(iL + \sum_{k=1}^{\infty}\Delta t^{2k}C_k\right)\right], \quad (\text{A.30})$$

known as the Baker-Campbell-Hausdorff formula [238]. The operators C_k appearing in the formula above are nested commutators of iL_1 and iL_2 . For example

$$C_1 = -\frac{1}{24}[iL_2 + 2iL_1, [iL_2, iL_1]] \quad (\text{A.31})$$

is the first term of the expansion and contains one nested operator, the second term contains two nested operators and so on. Using the *Jacobi identity* [239] it can be shown that the commutator $[iL_1, iL_2]$ corresponds to a new Liouville operator $-iL_3$ that is derived from the Hamiltonians $\mathcal{H}_1(x)$, $\mathcal{H}_2(x)$, which defined iL_1 and iL_2 respectively. The Jacobi identity states that for three functions $P(x), Q(x), R(x)$ on the phase space:

$$\{P(x), \{Q(x), R(x)\}\} + \{R(x), \{P(x), Q(x)\}\} + \{Q(x), \{R(x), P(x)\}\} = 0. \quad (\text{A.32})$$

Remember that iL_i was defined as $\{\dots, \mathcal{H}_i(x)\}$ in Eq. (A.4). Using this notation $[iL_1, iL_2]$ acting on an arbitrary phase function $F(x)$ can be written as

$$[iL_1, iL_2]F(x) = \{\{F(x), \mathcal{H}_2(x)\}, \mathcal{H}_1(x)\} - \{\{F(x), \mathcal{H}_1(x)\}, \mathcal{H}_2(x)\}. \quad (\text{A.33})$$

Using the Jacobi identity, the Poisson brackets can be rewritten by moving the functions around in a cyclic manner

$$\{\{F(x), \mathcal{H}_2(x)\}, \mathcal{H}_1(x)\} = -\{\{\mathcal{H}_1(x), F(x)\}, \mathcal{H}_2(x)\} - \{\{\mathcal{H}_2(x), \mathcal{H}_1(x)\}, F(x)\}. \quad (\text{A.34})$$

Substituting Eq. (A.34) in Eq. (A.33) yields,

$$[iL_1, iL_2]F(x) = -\{F(x), \{\mathcal{H}_1(x), \mathcal{H}_2(x)\}\} = -\{F(x), \mathcal{H}_3(x)\}. \quad (\text{A.35})$$

The C_1 term corresponds to an Hamiltonian $\tilde{\mathcal{H}}$ given by:

$$\tilde{\mathcal{H}} = \frac{1}{24} \{ \mathcal{H}_2 + 2\mathcal{H}_1, \{ \mathcal{H}_2, \mathcal{H}_1 \} \}. \quad (\text{A.36})$$

A similar analysis can be carried out for each of the C_k terms in Eq. (A.30). Each operator C_k corresponds to an Hamiltonian $\tilde{\mathcal{H}}_k(x)$ so that the factorized operator on the LHS of Eq. (A.30) that was used to define the velocity Verlet algorithm is generated by a Hamiltonian $\tilde{\mathcal{H}}$ of the form

$$\tilde{\mathcal{H}}(x; \Delta t) = \mathcal{H}(x) + \sum_{k=1}^{\infty} \Delta t^{2k} \tilde{\mathcal{H}}_k, \quad (\text{A.37})$$

which is exactly conserved. This is the shadow Hamiltonian that was further discussed in Sec. 3.2. It should now also be clear that $\tilde{\mathcal{H}}(x; \Delta t) \rightarrow \mathcal{H}$ as $\Delta t \rightarrow 0$.

3 Lie product formula

In Appx. 1, the exponential of the sum of two matrices A, B is rewritten in the following way:

$$e^{A+B} = \lim_{m \rightarrow \infty} \left(e^{B/2m} e^{A/m} e^{B/2m} \right)^m. \quad (\text{A.38})$$

This identity is referred to as the symmetric Trotter theorem or Strang splitting formula and holds in a more general context than what will be presented here [240, 241]. In this section, a proof is given for this theorem for A, B being $n \times n$ complex matrices ($M_n(\mathbb{C})$), which is known as the Lie product formula [242].

We will start off by defining the norm of a matrix by thinking of the set $M_n(\mathbb{C})$ of all $n \times n$ matrices as an extension of the vector space \mathbb{C}^n , i.e. \mathbb{C}^{n^2} . We define the norm of X as

$$\|X\| = \left(\sum_{k,l=1}^n |X_{kl}|^2 \right)^{\frac{1}{2}}, \quad (\text{A.39})$$

which is called the Hilbert-Schmidt norm [243].

Next, we need to introduce an algebraic expression that is needed later on: For all $n \times n$ matrices X with $\|X\| < \frac{1}{2}$,

$$\ln(I + X) = X + \mathcal{O}(\|X\|^2). \quad (\text{A.40})$$

Which can be made clear when writing down the power series of $\ln(I + X) - X$:

$$\ln(I + X) - X = \sum_{m=2}^{\infty} (-1)^{m+1} \frac{X^m}{m} = X^2 \sum_{m=2}^{\infty} (-1)^{m+1} \frac{X^{m-2}}{m}, \quad (\text{A.41})$$

so that

$$\|\ln(I+X) - X\| \leq \|X\|^2 \sum_{m=2}^{\infty} \frac{(\frac{1}{2})^{m-2}}{m}. \quad (\text{A.42})$$

Using this expression, we can show the Lie product relation in Eq. (A.38) by multiplying the power series of $e^{B/2m}$ and $e^{A/m}$:

$$e^{B/2m} e^{A/m} e^{B/2m} = I + \frac{A}{m} + \frac{B}{m} + \mathcal{O}\left(\frac{1}{m^2}\right). \quad (\text{A.43})$$

This expression can be rewritten using Eq. (A.40):

$$\ln\left(e^{B/2m} e^{A/m} e^{B/2m}\right) = \ln\left(I + \frac{A}{m} + \frac{B}{m} + \mathcal{O}\left(\frac{1}{m^2}\right)\right) \quad (\text{A.44})$$

$$= \frac{A}{m} + \frac{B}{m} + \mathcal{O}\left(\left\|\frac{A}{m} + \frac{B}{m} + \mathcal{O}\left(\frac{1}{m^2}\right)\right\|^2\right) \quad (\text{A.45})$$

$$= \frac{A}{m} + \frac{B}{m} + \mathcal{O}\left(\frac{1}{m^2}\right). \quad (\text{A.46})$$

Exponentiating the above equation then gives:

$$e^{B/2m} e^{A/m} e^{B/2m} = \exp\left[\frac{A}{m} + \frac{B}{m} + \mathcal{O}\left(\frac{1}{m^2}\right)\right], \quad (\text{A.47})$$

so that

$$\left(e^{B/2m} e^{A/m} e^{B/2m}\right)^m = \exp\left[A + B + \mathcal{O}\left(\frac{1}{m}\right)\right]. \quad (\text{A.48})$$

We can now conclude that:

$$\lim_{m \rightarrow \infty} \left(e^{B/2m} e^{A/m} e^{B/2m}\right)^m = e^{A+B}. \quad (\text{A.49})$$

Which is the Lie product formula.

References

- [1] D. Evans and H. Wennerström, *The Colloidal Domain: Where Physics, Chemistry, Biology, and Technology Meet*, vol. 2. Wiley, 1999.
- [2] H. Weller, “Colloidal semiconductor q-particles: Chemistry in the transition region between solid state and molecules,” *Angewandte Chemie International Edition in English*, vol. 32, no. 1, pp. 41–53, 1993.
- [3] C. P. Collier, T. Vossmeier, and J. Heath, “Nanocrystal superlattices,” *Annual Review of Physical Chemistry*, vol. 49, no. 1, pp. 371–404, 1998.
- [4] C. López, “Materials aspects of photonic crystals,” *Advanced Materials*, vol. 15, no. 20, pp. 1679–1704, 2003.
- [5] S. Chen, Z. Lin Wang, J. Ballato, S. H. Foulger, and D. L. Carroll, “Monopod, bipod, tripod, and tetrapod gold nanocrystals,” *Journal of the American Chemical Society*, vol. 125, no. 52, pp. 16186–16187, 2003.
- [6] C. J. Loweth, W. B. Caldwell, X. Peng, A. P. Alivisatos, and P. G. Schultz, “Dna-based assembly of gold nanocrystals,” *Angewandte Chemie International Edition*, vol. 38, no. 12, pp. 1808–1812, 1999.
- [7] P. M. Johnson, C. M. van Kats, and A. van Blaaderen, “Synthesis of colloidal silica dumbbells,” *Langmuir*, vol. 21, no. 24, pp. 11510–11517, 2005.
- [8] Y. Lu, H. Xiong, X. Jiang, Y. Xia, M. Prentiss, and G. M. Whitesides, “Asymmetric dimers can be formed by dewetting half-shells of gold deposited on the surfaces of spherical oxide colloids,” *Journal of the American Chemical Society*, vol. 125, no. 42, pp. 12724–12725, 2003.

- [9] V. N. Manoharan, M. T. Elsesser, and D. J. Pine, "Dense packing and symmetry in small clusters of microspheres," *Science*, vol. 301, no. 5632, pp. 483–487, 2003.
- [10] K.-S. Cho, D. V. Talapin, W. Gaschler, and C. B. Murray, "Designing pbse nanowires and nanorings through oriented attachment of nanoparticles," *Journal of the American Chemical Society*, vol. 127, no. 19, pp. 7140–7147, 2005.
- [11] Y. Sun and Y. Xia, "Shape-controlled synthesis of gold and silver nanoparticles," *Science*, vol. 298, no. 5601, pp. 2176–2179, 2002.
- [12] D. Dendukuri, D. C. Pregibon, J. Collins, T. A. Hatton, and P. S. Doyle, "Continuous-flow lithography for high-throughput microparticle synthesis," *Nature Materials*, vol. 5, pp. 365–369, 2006.
- [13] Y.-Y. Yu, S.-S. Chang, C.-L. Lee, and C. R. C. Wang, "Gold nanorods: Electrochemical synthesis and optical properties," *The Journal of Physical Chemistry B*, vol. 101, no. 34, pp. 6661–6664, 1997.
- [14] A. Mohraz and M. J. Solomon, "Direct visualization of colloidal rod assembly by confocal microscopy," *Langmuir*, vol. 21, no. 12, pp. 5298–5306, 2005.
- [15] A. M. Jackson, Y. Hu, P. J. Silva, and F. Stellacci, "From hololigand- to mixed ligand- monolayer-protected metal nanoparticles: A scanning tunneling microscopy investigation," *Journal of the American Chemical Society*, vol. 128, no. 34, pp. 11135–11149, 2006.
- [16] G. Zhang, D. Wang, and H. Möhwald, "Decoration of microspheres with gold nanodots—giving colloidal spheres valences," *Angewandte Chemie International Edition*, vol. 44, no. 47, pp. 7767–7770, 2005.
- [17] O. Cayre, V. N. Paunov, and O. D. Velev, "Fabrication of asymmetrically coated colloid particles by microcontact printing techniques," *J. Mater. Chem.*, vol. 13, pp. 2445–2450, 2003.
- [18] J. S. Lindsey, "Cheminform abstract: Self-assembly in synthetic routes to molecular devices. biological principles and chemical perspectives: A review," *ChemInform*, vol. 22, no. 38, 1991.
- [19] Q. Chen, S. C. Bae, and S. Granick, "Directed self-assembly of a colloidal kagome lattice," *Nature*, vol. 469, pp. 381–384, Jan 2011.
- [20] P. G. de Gennes, "Soft matter," *Rev. Mod. Phys.*, vol. 64, pp. 645–648, Jul 1992.
- [21] J. N. Israelachvili, *Intermolecular and surface forces*. Colloid Science, Academic Press, 2 ed., 1992.

-
- [22] A. Walther and A. H. E. Muller, "Janus particles," *Soft Matter*, vol. 4, pp. 663–668, 2008.
- [23] W. A. Braunecker and K. Matyjaszewski, "Controlled/living radical polymerization: Features, developments, and perspectives," *Progress in Polymer Science*, vol. 32, no. 1, pp. 93 – 146, 2007.
- [24] M. Lattuada and T. A. Hatton, "Synthesis, properties and applications of janus nanoparticles," *Nano Today*, vol. 6, no. 3, pp. 286 – 308, 2011.
- [25] C. Casagrande, P. Fabre, E. Raphaël, and M. Veyssié, "'janus beads': Realization and behaviour at water/oil interfaces," *EPL (Europhysics Letters)*, vol. 9, no. 3, p. 251, 1989.
- [26] A. Perro, S. Reculosa, S. Ravaine, E. Bourgeat-Lami, and E. Duguet, "Design and synthesis of janus micro- and nanoparticles," *J. Mater. Chem.*, vol. 15, pp. 3745–3760, 2005.
- [27] K.-H. Roh, D. C. Martin, and J. Lahann, "Biphasic janus particles with nanoscale anisotropy," *Nat Mater*, vol. 4, pp. 759–763, Oct 2005.
- [28] C. J. Behrend, J. N. Anker, and R. Kopelman, "Brownian modulated optical nanoprobe," *Applied Physics Letters*, vol. 84, no. 1, pp. 154–156, 2004.
- [29] L. Y. Wu, B. M. Ross, S. Hong, and L. P. Lee, "Bioinspired nanocorals with decoupled cellular targeting and sensing functionality," *Small*, vol. 6, no. 4, pp. 503–507, 2010.
- [30] T. Nisisako, T. Torii, T. Takahashi, and Y. Takizawa, "Synthesis of monodisperse bicolored janus particles with electrical anisotropy using a microfluidic co-flow system," *Advanced Materials*, vol. 18, no. 9, pp. 1152–1156, 2006.
- [31] E. Kay, D. Leigh, and F. Zerbetto, "Synthetic molecular motors and mechanical machines," *Angewandte Chemie International Edition*, vol. 46, no. 1-2, pp. 72–191, 2007.
- [32] H. Stone, A. Stroock, and A. Ajdari, "Engineering flows in small devices," *Annual Review of Fluid Mechanics*, vol. 36, no. 1, pp. 381–411, 2004.
- [33] J. R. Howse, R. A. L. Jones, A. J. Ryan, T. Gough, R. Vafabakhsh, and R. Golestanian, "Self-motile colloidal particles: From directed propulsion to random walk," *Phys. Rev. Lett.*, vol. 99, p. 048102, Jul 2007.
- [34] M. Terrones, A. R. Botello-Méndez, J. Campos-Delgado, F. López-Urías, Y. I. Vega-Cantú, F. J. Rodríguez-Macías, A. L. Elías, E. Muñoz-Sandoval, A. G. Cano-Márquez, J.-C. Charlier, and H. Terrones, "Graphene and graphite

- nanoribbons: Morphology, properties, synthesis, defects and applications,” *Nano Today*, vol. 5, no. 4, pp. 351 – 372, 2010.
- [35] K. S. Novoselov, A. K. Geim, S. V. Morozov, D. Jiang, Y. Zhang, S. V. Dubonos, I. V. Grigorieva, and A. A. Firsov, “Electric field effect in atomically thin carbon films,” *Science*, vol. 306, no. 5696, pp. 666–669, 2004.
- [36] A. H. Castro Neto, F. Guinea, N. M. R. Peres, K. S. Novoselov, and A. K. Geim, “The electronic properties of graphene,” *Rev. Mod. Phys.*, vol. 81, pp. 109–162, Jan 2009.
- [37] S. Das Sarma, S. Adam, E. H. Hwang, and E. Rossi, “Electronic transport in two-dimensional graphene,” *Rev. Mod. Phys.*, vol. 83, pp. 407–470, May 2011.
- [38] C. Lee, X. Wei, J. W. Kysar, and J. Hone, “Measurement of the elastic properties and intrinsic strength of monolayer graphene,” *Science*, vol. 321, no. 5887, pp. 385–388, 2008.
- [39] A. A. Balandin, “Thermal properties of graphene and nanostructured carbon materials,” *Nature Materials*, vol. 10, pp. 569–581, 2011.
- [40] A. Pakdel, Y. Bando, and D. Golberg, “Nano boron nitride flatland,” *Chem. Soc. Rev.*, vol. 43, pp. 934–959, 2014.
- [41] K. S. Novoselov, D. Jiang, F. Schedin, T. J. Booth, V. V. Khotkevich, S. V. Morozov, and A. K. Geim, “Two-dimensional atomic crystals,” *Proceedings of the National Academy of Sciences of the United States of America*, vol. 102, no. 30, pp. 10451–10453, 2005.
- [42] K. S. Novoselov, V. I. Fal’ko, L. Colombo, P. R. Gellert, M. G. Schwab, and K. Kim, “A roadmap for graphene,” *Nature*, vol. 490, no. 7419, pp. 192–200, 2012.
- [43] D. Rapaport, *The Art of Molecular Dynamics Simulation*, vol. 2. Cambridge University Press, 2004.
- [44] W. Kohn and L. J. Sham, “Self-consistent equations including exchange and correlation effects,” *Phys. Rev.*, vol. 140, pp. A1133–A1138, Nov 1965.
- [45] B. R. Brooks, R. E. Bruccoleri, B. D. Olafson, D. J. States, S. Swaminathan, and M. Karplus, “Charmm: A program for macromolecular energy, minimization, and dynamics calculations,” *Journal of Computational Chemistry*, vol. 4, no. 2, pp. 187–217, 1983.

-
- [46] N. Schmid, A. P. Eichenberger, A. Choutko, S. Riniker, M. Winger, A. E. Mark, and W. F. van Gunsteren, "Definition and testing of the GROMOS force-field versions 54A7 and 54B7," *European Biophysics Journal*, vol. 40, no. 7, pp. 843–856, 2011.
- [47] B. Hardy and A. Sarko, "Conformational analysis and molecular dynamics simulation of cellobiose and larger cellooligomers," *Journal of Computational Chemistry*, vol. 14, no. 7, pp. 831–847, 1993.
- [48] A. C. T. van Duin, S. Dasgupta, F. Lorant, and W. A. Goddard, "Reaxff a reactive force field for hydrocarbons," *The Journal of Physical Chemistry A*, vol. 105, no. 41, pp. 9396–9409, 2001.
- [49] P.-S. Laplace and A. I. Dale, *Philosophical Essay on Probabilities*, vol. 13. Springer New York, 1995.
- [50] L. Kelvin., *Baltimore Lectures on Molecular Dynamics and the Wave Theory of Light*. CUP, 1904.
- [51] B. J. Alder and T. E. Wainwright, "Phase transition for a hard sphere system," *The Journal of Chemical Physics*, vol. 27, no. 5, pp. 1208–1209, 1957.
- [52] J. B. Gibson, A. N. Goland, M. Milgram, and G. H. Vineyard, "Dynamics of radiation damage," *Phys. Rev.*, vol. 120, pp. 1229–1253, Nov 1960.
- [53] A. Rahman, "Correlations in the motion of atoms in liquid argon," *Phys. Rev.*, vol. 136, pp. A405–A411, Oct 1964.
- [54] J. M. Haile, *Molecular dynamics simulation : elementary methods*. Wiley, 1992.
- [55] A. R. Leach, *Molecular modelling : principles and applications*. Prentice Hall, 2nd ed ed., 2001.
- [56] D. J. T. M. P. Allen, *Computer simulation of liquids*. Oxford University Press, USA, 1989.
- [57] M. E. Tuckerman, *Statistical Mechanics: Theory and Molecular Simulation*. Oxford Graduate Texts, OUP, 2010.
- [58] A. Einstein, "Investigations on the theory of the Brownian movement," *Annalen der Physik*, vol. 19, 1905.
- [59] B. L. Holian, A. F. Voter, and R. Ravelo, "Thermostatted molecular dynamics: How to avoid the toda demon hidden in nosé-hoover dynamics," *Phys. Rev. E*, vol. 52, pp. 2338–2347, Sep 1995.

- [60] D. Ruelle, *Chaotic evolution and strange attractors*. Lezioni Lincee, Cambridge University Press, 1 ed., 1989.
- [61] R. Edwards, I. Horváth, and A. Kennedy, “Instabilities and non-reversibility of molecular dynamics trajectories,” *Nuclear Physics B*, vol. 484, no. 1–2, pp. 375 – 399, 1997.
- [62] R. Seifried, *Dynamics of Underactuated Multibody Systems: Modeling, Control and Optimal Design*. Solid Mechanics and Its Applications 205, Springer International Publishing, 1 ed., 2014.
- [63] L. Verlet, “Computer experiments on classical fluids. I. thermodynamical properties of lennard-jones molecules,” *Phys. Rev.*, vol. 159, pp. 98–103, Jul 1967.
- [64] C. W. Gear, *Numerical Initial Value Problems in Ordinary Differential Equations*. Upper Saddle River, NJ, USA: Prentice Hall PTR, 1971.
- [65] N. I., *Philosophiae Naturalis Principia Mathematica*. EEBO Editions, ProQuest, 1687.
- [66] E. Hairer, C. Lubich, and G. Wanner, “Geometric numerical integration illustrated by the Störmer/Verlet method,” *Acta Numerica*, vol. 12, pp. 399–450, 2003.
- [67] J. Gans and D. Shalloway, “Shadow mass and the relationship between velocity and momentum in symplectic numerical integration,” *Phys. Rev. E*, vol. 61, pp. 4587–4592, Apr 2000.
- [68] S. Toxvaerd, “Hamiltonians for discrete dynamics,” *Phys. Rev. E*, vol. 50, pp. 2271–2274, Sep 1994.
- [69] R. D. Skeel and D. J. Hardy, “Practical construction of modified hamiltonians,” *SIAM J. Sci. Comput*, vol. 23, pp. 1172–1188, 2001.
- [70] J. A. Izaguirre and S. S. Hampton, “Shadow hybrid monte carlo: an efficient propagator in phase space of macromolecules,” *Journal of Computational Physics*, vol. 200, no. 2, pp. 581 – 604, 2004.
- [71] S. Toxvaerd, O. J. Heilmann, and J. C. Dyre, “Energy conservation in molecular dynamics simulations of classical systems,” *The Journal of Chemical Physics*, vol. 136, no. 22, 2012.
- [72] C. Runge, “Ueber die numerische auflösung von differentialgleichungen,” *Mathematische Annalen*, vol. 46, no. 2, pp. 167–178, 1895.

-
- [73] W. Kutta, "Beitrag zur naherungsweise integration von differentialgleichungen," *Zit. Math. Physik*, vol. 46, pp. 435–453, 1901.
- [74] J. C. Butcher, *Numerical Methods for Ordinary Differential Equations*. J. Wiley, 2nd ed., 2003.
- [75] A. Odell, A. Delin, B. Johansson, N. Bock, M. Challacombe, and A. M. N. Niklasson, "Higher-order symplectic integration in born–oppenheimer molecular dynamics," *The Journal of Chemical Physics*, vol. 131, no. 24, 2009.
- [76] D. I. Okunbor, "Energy conserving, liouville, and symplectic integrators," *J. Comput. Phys.*, vol. 120, pp. 375–378, Sept. 1995.
- [77] G. J. Martyna and M. E. Tuckerman, "Symplectic reversible integrators: Predictor–corrector methods," *The Journal of Chemical Physics*, vol. 102, no. 20, pp. 8071–8077, 1995.
- [78] D. Frenkel and B. Smit, *Understanding Molecular Simulation, Second Edition: From Algorithms to Applications*. Academic Press, second edition ed., 2001.
- [79] A. D. Buckingham, *Intermolecular forces*, pp. 1–16. Dordrecht: Springer Netherlands, 1993.
- [80] J.-P. Hansen and I. R. McDonald, *Theory of Simple Liquids (Third Edition)*. Academic Press, third edition ed., 2006.
- [81] Y. Fily and M. C. Marchetti, "Athermal phase separation of self-propelled particles with no alignment," *Phys. Rev. Lett.*, vol. 108, p. 235702, Jun 2012.
- [82] W. Kauzmann, "Some factors in the interpretation of protein denaturation," *Adv. Protein. Chem.*, vol. 14, pp. 1–63, 1959.
- [83] J. H. Hildebrand, "A criticism of the term "hydrophobic bond"," *The Journal of Physical Chemistry*, vol. 72, no. 5, pp. 1841–1842, 1968.
- [84] C. Tanford, "Contribution of hydrophobic interactions to the stability of the globular conformation of proteins," *Journal of the American Chemical Society*, vol. 84, no. 22, pp. 4240–4247, 1962.
- [85] D. M. Crothers and D. I. Ratner, "Thermodynamic studies of a model system for hydrophobic bonding," *Biochemistry*, vol. 7, no. 5, pp. 1823–1827, 1968.
- [86] E. E. Meyer, K. J. Rosenberg, and J. Israelachvili, "Recent progress in understanding hydrophobic interactions," *Proceedings of the National Academy of Sciences*, vol. 103, no. 43, pp. 15739–15746, 2006.

- [87] H. Hamaker, “The london—van der waals attraction between spherical particles,” *Physica*, vol. 4, no. 10, pp. 1058 – 1072, 1937.
- [88] F. L. Leite, C. C. Bueno, A. L. Da Róz, E. C. Ziemath, and O. N. Oliveira, “Theoretical models for surface forces and adhesion and their measurement using atomic force microscopy,” *International Journal of Molecular Sciences*, vol. 13, no. 10, p. 12773, 2012.
- [89] L. F. Rojas-Ochoa, R. Castañeda Priego, V. Lobaskin, A. Stradner, F. Scheffold, and P. Schurtenberger, “Density dependent interactions and structure of charged colloidal dispersions in the weak screening regime,” *Phys. Rev. Lett.*, vol. 100, p. 178304, May 2008.
- [90] J. T. G. O. E. J. W. Verwey, “Theory of the stability of lyophobic colloids,” *Nature*, vol. 162, pp. 315 – 316, 1948.
- [91] A. Ashkin, “Forces of a single-beam gradient laser trap on a dielectric sphere in the ray optics regime,” *Biophysical Journal*, vol. 61, no. 2, pp. 569 – 582, 1992.
- [92] J. E. Molloy and M. J. Padgett, “Lights, action: Optical tweezers,” *Contemporary Physics*, vol. 43, no. 4, pp. 241–258, 2002.
- [93] M. Jenkins and S. Egelhaaf, “Colloidal suspensions in modulated light fields,” *Journal of Physics: Condensed Matter*, vol. 20, no. 40, p. 404220, 2008.
- [94] J. D. Jackson, *Classical electrodynamics*. Wiley, 3rd ed ed., 1999.
- [95] A. Ashkin, “Acceleration and trapping of particles by radiation pressure,” *Phys. Rev. Lett.*, vol. 24, pp. 156–159, Jan 1970.
- [96] A. Ashkin, J. M. Dziedzic, J. E. Bjorkholm, and S. Chu, “Observation of a single-beam gradient force optical trap for dielectric particles,” *Opt. Lett.*, vol. 11, pp. 288–290, May 1986.
- [97] M. P. S. (Eds.), *Laser Tweezers in Cell Biology*, vol. 55 of *Methods in Cell Biology*. Academic Press, 1 ed., 1997.
- [98] W. Irvine, M. Bowick, and P. Chaikin, “Fractionalization of interstitials in curved colloidal crystals,” *Nature Materials*, vol. 11, pp. 948–951, 2012.
- [99] Maret-Group, “Colloids and Optical Tweezers,” 2002. [Online; accessed 04-June-2016].
- [100] A. Nych, M. Ognysta, M. Skarabot, M. Ravník, S. Zumer, and I. Musevic, “Assembly and control of 3d nematic dipolar colloidal crystals,” *Nature Communications*, vol. 4, no. 1489, 2013.

-
- [101] D. Chandler, "Equilibrium theory of polyatomic fluids," *Studies in Statistical Mechanics*, vol. 8, pp. 275–340, 1982.
- [102] K. Burke, J. Werschnik, and E. K. U. Gross, "Time-dependent density functional theory: Past, present, and future," *The Journal of Chemical Physics*, vol. 123, no. 6, 2005.
- [103] Y. Duan, C. Wu, S. Chowdhury, M. C. Lee, G. Xiong, W. Zhang, R. Yang, P. Cieplak, R. Luo, T. Lee, J. Caldwell, J. Wang, and P. Kollman, "A point-charge force field for molecular mechanics simulations of proteins based on condensed-phase quantum mechanical calculations," *Journal of Computational Chemistry*, vol. 24, no. 16, pp. 1999–2012, 2003.
- [104] W. L. Jorgensen, J. Chandrasekhar, J. D. Madura, R. W. Impey, and M. L. Klein, "Comparison of simple potential functions for simulating liquid water," *The Journal of Chemical Physics*, vol. 79, no. 2, pp. 926–935, 1983.
- [105] M. Mollhoff and U. Sternberg, "Molecular mechanics with fluctuating atomic charges - a new force field with a semi-empirical charge calculation," *Journal of Molecular Modeling*, vol. 7, no. 4, pp. 90–1002, 2001.
- [106] W. J. Mortier, S. K. Ghosh, and S. Shankar, "Electronegativity-equalization method for the calculation of atomic charges in molecules," *Journal of the American Chemical Society*, vol. 108, no. 15, pp. 4315–4320, 1986.
- [107] S. Plimpton, "Fast parallel algorithms for short-range molecular dynamics," *Journal of Computational Physics*, vol. 117, no. 1, pp. 1 – 19, 1995.
- [108] D. Vonlanthen, A. Mishchenko, M. Elbing, M. Neuburger, T. Wandlowski, and M. Mayor, "Chemically controlled conductivity: Torsion-angle dependence in a single-molecule biphenyldithiol junction," *Angewandte Chemie International Edition*, vol. 48, no. 47, pp. 8886–8890, 2009.
- [109] J. M. Buehler, A. Hartmaier, H. Gao, A. M. Duchaineau, and F. F. Abraham, "The dynamical complexity of work-hardening: a large-scale molecular dynamics simulation," *Acta Mechanica Sinica*, vol. 21, no. 2, pp. 103–111, 2005.
- [110] P. Schofield, "Computer simulation studies of the liquid state," *Computer Physics Communications*, vol. 5, no. 1, pp. 17 – 23, 1973.
- [111] L. Woodcock, "Isothermal molecular dynamics calculations for liquid salts," *Chemical Physics Letters*, vol. 10, no. 3, pp. 257–261, 1971.
- [112] H. J. C. Berendsen, J. P. M. Postma, W. F. van Gunsteren, A. DiNola, and J. R. Haak, "Molecular dynamics with coupling to an external bath," *The Journal of Chemical Physics*, vol. 81, no. 8, pp. 3684–3690, 1984.

- [113] W. G. Hoover, “Canonical dynamics: Equilibrium phase-space distributions,” *Phys. Rev. A*, vol. 31, pp. 1695–1697, Mar 1985.
- [114] S. Nosé, “A unified formulation of the constant temperature molecular dynamics methods,” *The Journal of Chemical Physics*, vol. 81, no. 1, pp. 511–519, 1984.
- [115] Z. Lu and Y. Yin, “Colloidal nanoparticle clusters: functional materials by design,” *Chem. Soc. Rev.*, vol. 41, pp. 6874–6887, 2012.
- [116] M. Sobrino Fernández, V. R. Misko, and F. M. Peeters, “Self-assembly of janus particles confined in a channel,” *Phys. Rev. E*, vol. 89, p. 022306, Feb 2014.
- [117] R. J. Macfarlane, B. Lee, M. R. Jones, N. Harris, G. C. Schatz, and C. A. Mirkin, “Nanoparticle superlattice engineering with dna,” *Science*, vol. 334, no. 6053, pp. 204–208, 2011.
- [118] A. B. Pawar and I. Kretzschmar, “Patchy particles by glancing angle deposition,” *Langmuir*, vol. 24, no. 2, pp. 355–358, 2008.
- [119] S. Sacanna, L. Rossi, and D. J. Pine, “Magnetic click colloidal assembly,” *Journal of the American Chemical Society*, vol. 134, no. 14, pp. 6112–6115, 2012.
- [120] S. Sacanna and D. J. Pine, “Shape-anisotropic colloids: Building blocks for complex assemblies,” *Current Opinion in Colloid & Interface Science*, vol. 16, no. 2, pp. 96 – 105, 2011.
- [121] K. P. Yuet, D. K. Hwang, R. Haghgooie, and P. S. Doyle, “Multifunctional superparamagnetic janus particles,” *Langmuir*, vol. 26, no. 6, pp. 4281–4287, 2010.
- [122] G. Volpe, I. Buttinoni, D. Vogt, H.-J. Kummerer, and C. Bechinger, “Microswimmers in patterned environments,” *Soft Matter*, vol. 7, pp. 8810–8815, 2011.
- [123] L. Baraban, R. Streubel, D. Makarov, L. Han, D. Karnaushenko, O. G. Schmidt, and G. Cuniberti, “Fuel-free locomotion of janus motors: Magnetically induced thermophoresis,” *ACS Nano*, vol. 7, no. 2, pp. 1360–1367, 2013.
- [124] M. J. Solomon, “Directions for targeted self-assembly of anisotropic colloids from statistical thermodynamics,” *Current Opinion in Colloid & Interface Science*, vol. 16, no. 2, pp. 158 – 167, 2011.

-
- [125] S. C. Glotzer and M. J. Solomon, "Anisotropy of building blocks and their assembly into complex structures," *Nature Materials*, vol. 6, no. 8, pp. 557–62, 2007.
- [126] G. Doppelbauer, E. Bianchi, and G. Kahl, "Self-assembly scenarios of patchy colloidal particles in two dimensions," *Journal of Physics: Condensed Matter*, vol. 22, no. 10, p. 104105, 2010.
- [127] Y. Xiang, S. Lu, and S. P. Jiang, "Layer-by-layer self-assembly in the development of electrochemical energy conversion and storage devices from fuel cells to supercapacitors," *Chemical Society Reviews*, vol. 41, pp. 7291–7321, 2012.
- [128] J. Li, C. Fan, H. Pei, J. Shi, and Q. Huang, "Smart drug delivery nanocarriers with self-assembled dna nanostructures," *Advanced Materials*, vol. 25, no. 32, pp. 4386–4396, 2013.
- [129] M. J. Campolongo, S. J. Tan, J. Xu, and D. Luo, "DNA nanomedicine: Engineering DNA as a polymer for therapeutic and diagnostic applications," *Advanced Drug Delivery Reviews*, vol. 62, no. 6, pp. 606 – 616, 2010.
- [130] M. A. Bucaro, P. R. Kolodner, J. A. Taylor, A. Sidorenko, J. Aizenberg, and T. N. Krupenkin, "Tunable liquid optics: Electrowetting-controlled liquid mirrors based on self-assembled janus tiles," *Langmuir*, vol. 25, no. 6, pp. 3876–3879, 2009.
- [131] W. Yang, V. R. Misko, K. Nelissen, M. Kong, and F. M. Peeters, "Using self-driven microswimmers for particle separation," *Soft Matter*, vol. 8, pp. 5175–5179, 2012.
- [132] S. Jain and F. S. Bates, "On the origins of morphological complexity in block copolymer surfactants," *Science*, vol. 300, no. 5618, pp. 460–464, 2003.
- [133] Z. Mao, H. Xu, and D. Wang, "Molecular mimetic self-assembly of colloidal particles," *Advanced Functional Materials*, vol. 20, no. 7, pp. 1053–1074, 2010.
- [134] D. E. Tambe and M. M. Sharma, "The effect of colloidal particles on fluid-fluid interfacial properties and emulsion stability," *Advances in Colloid and Interface Science*, vol. 52, pp. 1 – 63, 1994.
- [135] B. P. Binks, "Particles as surfactants—similarities and differences," *Current Opinion in Colloid & Interface Science*, vol. 7, no. 1–2, pp. 21 – 41, 2002.
- [136] B. P. Binks and J. A. Rodrigues, "Inversion of emulsions stabilized solely by ionizable nanoparticles," *Angewandte Chemie International Edition*, vol. 44, no. 3, pp. 441–444, 2005.

- [137] T. S. Horozov and B. P. Binks, "Particle-stabilized emulsions: A bilayer or a bridging monolayer?," *Angewandte Chemie International Edition*, vol. 45, no. 5, pp. 773–776, 2006.
- [138] A. D. Dinsmore, M. F. Hsu, M. G. Nikolaides, M. Marquez, A. R. Bausch, and D. A. Weitz, "Colloidosomes: Selectively permeable capsules composed of colloidal particles," *Science*, vol. 298, no. 5595, pp. 1006–1009, 2002.
- [139] L. Hong, A. Cacciuto, E. Luijten, and S. Granick, "Clusters of amphiphilic colloidal spheres," *Langmuir*, vol. 24, no. 3, pp. 621–625, 2008.
- [140] F. Sciortino, A. Giacometti, and G. Pastore, "Phase diagram of janus particles," *Phys. Rev. Lett.*, vol. 103, p. 237801, Nov 2009.
- [141] G. Rosenthal, K. E. Gubbins, and S. H. L. Klapp, "Self-assembly of model amphiphilic janus particles," *The Journal of Chemical Physics*, vol. 136, no. 17, p. 174901, 2012.
- [142] B. M. Rosen, C. J. Wilson, D. A. Wilson, M. Peterca, M. R. Imam, and V. Percec, "Dendron-mediated self-assembly, disassembly, and self-organization of complex systems," *Chemical Reviews*, vol. 109, no. 11, pp. 6275–6540, 2009.
- [143] A.-M. Caminade, R. Laurent, B. Delavaux-Nicot, and J.-P. Majoral, "'janus' dendrimers: syntheses and properties," *New J. Chem.*, vol. 36, pp. 217–226, 2012.
- [144] N. Kern and D. Frenkel, "Fluid–fluid coexistence in colloidal systems with short-ranged strongly directional attraction," *The Journal of Chemical Physics*, vol. 118, no. 21, pp. 9882–9889, 2003.
- [145] F. Sciortino, A. Giacometti, and G. Pastore, "A numerical study of one-patch colloidal particles: from square-well to janus," *Phys. Chem. Chem. Phys.*, vol. 12, pp. 11869–11877, 2010.
- [146] A. G. Maestre, Miguel, R. Fantoni, A. Giacometti, and A. Santos, "Janus fluid with fixed patch orientations: Theory and simulations," *The Journal of Chemical Physics*, vol. 138, no. 9, 2013.
- [147] R. Fantoni, D. Gazzillo, A. Giacometti, M. A. Miller, and G. Pastore, "Patchy sticky hard spheres: Analytical study and monte carlo simulations," *The Journal of Chemical Physics*, vol. 127, no. 23, 2007.
- [148] A. Giacometti, F. Lado, J. Largo, G. Pastore, and F. Sciortino, "Phase diagram and structural properties of a simple model for one-patch particles," *The Journal of Chemical Physics*, vol. 131, no. 17, 2009.

-
- [149] A. Giacometti, F. Lado, J. Largo, G. Pastore, and F. Sciortino, “Effects of patch size and number within a simple model of patchy colloids,” *The Journal of Chemical Physics*, vol. 132, no. 17, 2010.
- [150] P. K. Ghosh, V. R. Misko, F. Marchesoni, and F. Nori, “Self-propelled janus particles in a ratchet: Numerical simulations,” *Phys. Rev. Lett.*, vol. 110, p. 268301, Jun 2013.
- [151] B. V. Derjaguin and L. Landau, “Theory of the stability of strongly charged lyophobic sols and of the adhesion of strongly charged particles in solutions of electrolytes,” *Acta Physico Chimica URSS*, vol. 14, pp. 633–662, 1941.
- [152] C. G. Gray and K. E. Gubbins, “Theory of molecular fluids. volume 1: Fundamentals,” *International Journal of Quantum Chemistry*, vol. 38, no. 3, pp. 497–497, 1990.
- [153] A. Boerdijk, “Some remarks concerning close-packing of equal spheres,” *Philips Research Reports*, vol. 7, pp. 303–313, 1952.
- [154] H. S. M. Coxeter, *Regular complex polytopes*. Cambridge University Press London 1974, 1974.
- [155] J. Sadoc and N. Rivier, “Boerdijk-coxeter helix and biological helices,” *The European Physical Journal B*, vol. 12, no. 2, pp. 309–318, 1999.
- [156] S. N. Fejer, D. Chakrabarti, H. Kusumaatmaja, and D. J. Wales, “Design principles for bernal spirals and helices with tunable pitch,” *Nanoscale*, vol. 6, pp. 9448–9456, 2014.
- [157] E. I. Shakhnovich, “Theoretical studies of protein-folding thermodynamics and kinetics,” *Current Opinion in Structural Biology*, vol. 7, no. 1, p. 29–40, 1997.
- [158] J. D. Watson and F. H. C. Crick, “Molecular structure of nucleic acids,” *Nature (London)*, vol. 171, pp. 737–738, 1953.
- [159] M. Sobrino Fernández, V. R. Misko, and F. M. Peeters, “Self-assembly of janus particles into helices with tunable pitch,” *Phys. Rev. E*, vol. 92, p. 042309, Oct 2015.
- [160] U. Gasser, “Crystallization in three- and two-dimensional colloidal suspensions,” *Journal of Physics: Condensed Matter*, vol. 21, no. 20, p. 203101, 2009.
- [161] A. Cacciuto, S. Auer, and D. Frenkel, “Onset of heterogeneous crystal nucleation in colloidal suspensions,” *Nature*, vol. 428, pp. 404–406, 2004.

- [162] B. Yoon, P. Koskinen, B. Huber, O. Kostko, B. von Issendorff, H. Häkkinen, M. Moseler, and U. Landman, "Size-dependent structural evolution and chemical reactivity of gold clusters," *ChemPhysChem*, vol. 8, no. 1, pp. 157–161, 2007.
- [163] T. P. Knowles, A. W. Fitzpatrick, S. Meehan, H. R. Mott, M. Vendruscolo, C. M. Dobson, and M. E. Welland, "Role of intermolecular forces in defining material properties of protein nanofibrils," *Science*, vol. 318, no. 5858, pp. 1900–1903, 2007.
- [164] R. O. Erickson, "Tubular packing of spheres in biological fine structure," *Science*, vol. 181, no. 4101, pp. 705–716, 1973.
- [165] J. Groenewold and W. K. Kegel, "Anomalous large equilibrium clusters of colloids," *The Journal of Physical Chemistry B*, vol. 105, no. 47, pp. 11702–11709, 2001.
- [166] F. Sciortino, P. Tartaglia, and E. Zaccarelli, "One-dimensional cluster growth and branching gels in colloidal systems with short-range depletion attraction and screened electrostatic repulsion," *The Journal of Physical Chemistry B*, vol. 109, no. 46, pp. 21942–21953, 2005.
- [167] R. Podgornik, "Statistical thermodynamics of surfaces, interfaces, and membranes," *Journal of Statistical Physics*, vol. 78, no. 3, pp. 1175–1177, 1995.
- [168] H. Cui, T. Muraoka, A. G. Cheetham, and S. I. Stupp, "Self-assembly of giant peptide nanobelts," *Nano Letters*, vol. 9, no. 3, pp. 945–951, 2009.
- [169] R. Aurora, T. Creamer, R. Srinivasan, and G. Rose, "Local interactions in protein folding: Lessons from the α helix," *Journal of Biological Chemistry*, vol. 272, no. 3, pp. 1413–1416, 1997.
- [170] Y. Yu, "Coiled-coils: stability, specificity, and drug delivery potential," *Advanced Drug Delivery Reviews*, vol. 54, no. 8, pp. 1113 – 1129, 2002.
- [171] E. T. Pashuck and S. I. Stupp, "Direct observation of morphological transformation from twisted ribbons into helical ribbons," *Journal of the American Chemical Society*, vol. 132, no. 26, pp. 8819–8821, 2010.
- [172] M. J. Webber, J. Tongers, M.-A. Renault, J. G. Roncalli, D. W. Losordo, and S. I. Stupp, "Development of bioactive peptide amphiphiles for therapeutic cell delivery," *Acta Biomaterialia*, vol. 6, no. 1, pp. 3 – 11, 2010.
- [173] K. L. Niece, C. Czeisler, V. Sahni, V. Tysseling-Mattiace, E. T. Pashuck, J. A. Kessler, and S. I. Stupp, "Modification of gelation kinetics in bioactive peptide amphiphiles," *Biomaterials*, vol. 29, no. 34, pp. 4501 – 4509, 2008.

- [174] C. Chen, F. Pan, S. Zhang, J. Hu, M. Cao, J. Wang, H. Xu, X. Zhao, and J. R. Lu, "Antibacterial activities of short designer peptides: a link between propensity for nanostructuring and capacity for membrane destabilization," *Biomacromolecules*, vol. 11, no. 2, pp. 402–411, 2010.
- [175] R. N. Mitra, A. Shome, P. Paul, and P. K. Das, "Antimicrobial activity, biocompatibility and hydrogelation ability of dipeptide-based amphiphiles," *Org. Biomol. Chem.*, vol. 7, pp. 94–102, 2009.
- [176] Q. Chen, J. K. Whitmer, S. Jiang, S. C. Bae, E. Luijten, and S. Granick, "Supracolloidal reaction kinetics of janus spheres," *Science*, vol. 331, no. 6014, pp. 199–202, 2011.
- [177] G. J., *Colloids and Interfaces with Surfactants and Polymers*. Wiley, 2ed ed., 2009.
- [178] D. Chakrabarti, S. N. Fejer, and D. J. Wales, "Rational design of helical architectures," *Proceedings of the National Academy of Sciences*, vol. 106, no. 48, pp. 20164–20167, 2009.
- [179] D. Zerrouki, J. Baudry, D. Pine, P. Chaikin, and J. Bibette, "Chiral colloidal clusters," *Nature (London)*, vol. 455, no. 7211, pp. 380–382, 2008.
- [180] S. N. Fejer and D. J. Wales, "Helix self-assembly from anisotropic molecules," *Phys. Rev. Lett.*, vol. 99, p. 086106, Aug 2007.
- [181] R. Gray, "Tetrahelix data." <http://www.rwgrayprojects.com/rbfnodes/helix/helix01.html>, 2013. [Online; accessed 28-June-2016].
- [182] R. Zangi and A. E. Mark, "Monolayer ice," *Phys. Rev. Lett.*, vol. 91, p. 025502, Jul 2003.
- [183] R. Zangi and A. E. Mark, "Electrofreezing of confined water," *The Journal of Chemical Physics*, vol. 120, no. 15, pp. 7123–7130, 2004.
- [184] J. Bai, C. A. Angell, and X. C. Zeng, "Guest-free monolayer clathrate and its coexistence with two-dimensional high-density ice," *Proceedings of the National Academy of Sciences*, vol. 107, no. 13, pp. 5718–5722, 2010.
- [185] W.-H. Zhao, L. Wang, J. Bai, L.-F. Yuan, J. Yang, and X. C. Zeng, "Highly confined water: Two-dimensional ice, amorphous ice, and clathrate hydrates," *Accounts of Chemical Research*, vol. 47, no. 8, pp. 2505–2513, 2014.
- [186] F. Corsetti, P. Matthews, and E. Artacho, "Structural and configurational properties of nanoconfined monolayer ice from first principles," *Scientific Reports*, vol. 6, 2016.

- [187] C. Vega, C. McBride, E. Sanz, and J. L. F. Abascal, “Radial distribution functions and densities for the spc/e, TIP4P and TIP5P models for liquid water and ices Ih, Ic, II, III, IV, V, VI, VII, VIII, IX, XI and XII,” *Phys. Chem. Chem. Phys.*, vol. 7, pp. 1450–1456, 2005.
- [188] M. Ghosh, L. Pradipkanti, V. Rai, D. K. Satapathy, P. Vayalamkuzhi, and M. Jaiswal, “Confined water layers in graphene oxide probed with spectroscopic ellipsometry,” *Applied Physics Letters*, vol. 106, no. 24, 2015.
- [189] G. Algara-Siller, O. Lehtinen, F. C. Wang, R. R. Nair, U. Kaiser, H. A. Wu, A. K. Geim, and I. V. Grigorieva, “Square ice in graphene nanocapillaries,” *Nature*, vol. 519, no. 24, pp. 443–445, 2015.
- [190] T. Björkman, A. Gulans, A. V. Krasheninnikov, and R. M. Nieminen, “van der waals bonding in layered compounds from advanced density-functional first-principles calculations,” *Phys. Rev. Lett.*, vol. 108, p. 235502, Jun 2012.
- [191] S. P. Koenig, N. G. Boddeti, M. L. Dunn, and J. S. Bunch, “Ultrastrong adhesion of graphene membranes,” *Nat Nano*, vol. 6, pp. 543–546, 2011.
- [192] M. Sobrino Fernández, M. Neek-Amal, and F. M. Peeters, “Aa-stacked bilayer square ice between graphene layers,” *Phys. Rev. B*, vol. 92, p. 245428, Dec 2015.
- [193] Cmglee, “Phase diagram of water,” 2016. [Online; accessed 28-June-2016].
- [194] B. Best, “Lessons for cryonics from metallurgy and ceramics.” <http://www.benbest.com/cryonics/lessons.html>, 2016. [Online; accessed 26-June-2016].
- [195] J. D. Bernal and R. H. Fowler, “A theory of water and ionic solution, with particular reference to hydrogen and hydroxyl ions,” *The Journal of Chemical Physics*, vol. 1, no. 8, pp. 515–548, 1933.
- [196] L. Pauling, “The structure and entropy of ice and of other crystals with some randomness of atomic arrangement,” *Journal of the American Chemical Society*, vol. 57, no. 12, pp. 2680–2684, 1935.
- [197] A. B. Ryzhkov and P. A. Ariya, “The importance of water clusters (H₂O)_n (n = 2, . . . , 4) in the reaction of criegee intermediate with water in the atmosphere,” *Chemical Physics Letters*, vol. 419, no. 4–6, pp. 479 – 485, 2006.
- [198] N. Bjerrum, “Structure and properties of ice,” *Science*, vol. 115, no. 2989, pp. 385–390, 1952.
- [199] K. S. Pitzer and J. Polissar, “The order-disorder problem for ice,” *The Journal of Physical Chemistry*, vol. 60, no. 8, pp. 1140–1142, 1956.

- [200] S. Maheshwary, N. Patel, N. Sathyamurthy, A. D. Kulkarni, and S. R. Gadre, "Structure and stability of water clusters (H₂O)_n, n = 8-20: An ab initio investigation," *The Journal of Physical Chemistry A*, vol. 105, no. 46, pp. 10525–10537, 2001.
- [201] M. Luna, J. Colchero, and A. M. Baró, "Study of water droplets and films on graphite by noncontact scanning force microscopy," *The Journal of Physical Chemistry B*, vol. 103, no. 44, pp. 9576–9581, 1999.
- [202] E. Voloshina, D. Usvyat, M. Schutz, Y. Dedkov, and B. Paulus, "On the physisorption of water on graphene: a CCSD(T) study," *Phys. Chem. Chem. Phys.*, vol. 13, pp. 12041–12047, 2011.
- [203] D. Feller and K. D. Jordan, "Estimating the strength of the water/single-layer graphite interaction," *The Journal of Physical Chemistry A*, vol. 104, no. 44, pp. 9971–9975, 2000.
- [204] S. Xu, S. Irle, D. G. Musaev, and M. C. Lin, "Water clusters on graphite: Methodology for quantum chemical a priori prediction of reaction rate constants," *The Journal of Physical Chemistry A*, vol. 109, no. 42, pp. 9563–9572, 2005.
- [205] D. J. P. and V. Buch, *Water in Confining Geometries*. Springer Series in Cluster Physics, Springer-Verlag Berlin Heidelberg, 1 ed., 2003.
- [206] B. S. González, J. Hernández-Rojas, J. Bretón, and J. M. Gomez Llorente, "Global potential energy minima of (H₂O)_n clusters on graphite," *The Journal of Physical Chemistry C*, vol. 111, no. 40, pp. 14862–14869, 2007.
- [207] C. Luo, W. Fa, J. Zhou, J. Dong, and X. C. Zeng, "Ferroelectric ordering in ice nanotubes confined in carbon nanotubes," *Nano Letters*, vol. 8, no. 9, pp. 2607–2612, 2008.
- [208] J. Shiomi, T. Kimura, and S. Maruyama, "Molecular dynamics of ice-nanotube formation inside carbon nanotubes," *The Journal of Physical Chemistry C*, vol. 111, no. 33, pp. 12188–12193, 2007.
- [209] J. Köfinger, G. Hummer, and C. Dellago, "Macroscopically ordered water in nanopores," *Proceedings of the National Academy of Sciences*, vol. 105, no. 36, pp. 13218–13222, 2008.
- [210] M. M. C. David L. Nelson, *Lehninger Principles of Biochemistry*. W. H. Freeman, 5th ed., 2008.
- [211] W. Zhou, K. Yin, C. Wang, Y. Zhang, T. Xu, A. Borisevich, L. Sun, J. C. Idrobo, M. F. Chisholm, S. T. Pantelides, R. F. Klie, and A. R. Lupini, "The observation of square ice in graphene questioned," *Nature*, vol. 528, Dec 2015.

- [212] A. C. van Duin and J. S. Sinninghe Damsté, “Computational chemical investigation into isorenieratene cyclisation,” *Organic Geochemistry*, vol. 34, no. 4, pp. 515 – 526, 2003.
- [213] K. Chenoweth, A. C. T. van Duin, and W. A. Goddard, “Reaxff reactive force field for molecular dynamics simulations of hydrocarbon oxidation,” *The Journal of Physical Chemistry A*, vol. 112, no. 5, pp. 1040–1053, 2008.
- [214] J. L. F. Abascal and C. Vega, “A general purpose model for the condensed phases of water: TIP4P/2005,” *The Journal of Chemical Physics*, vol. 123, no. 23, 2005.
- [215] M. Chaplin, “Water’s hydrogen bond strength,” *arXiv*, vol. 0706.1355, 2007.
- [216] W.-H. Zhao, J. Bai, L.-F. Yuan, J. Yang, and X. C. Zeng, “Ferroelectric hexagonal and rhombic monolayer ice phases,” *Chem. Sci.*, vol. 5, pp. 1757–1764, 2014.
- [217] C. Y. Won and N. R. Aluru, “Water permeation through a subnanometer boron nitride nanotube,” *Journal of the American Chemical Society*, vol. 129, no. 10, pp. 2748–2749, 2007.
- [218] M. J. Iedema, M. J. Dresser, D. L. Doering, J. B. Rowland, W. P. Hess, A. A. Tsekouras, and J. P. Cowin, “Ferroelectricity in water ice,” *The Journal of Physical Chemistry B*, vol. 102, no. 46, pp. 9203–9214, 1998.
- [219] X. Su, L. Lianos, Y. R. Shen, and G. A. Somorjai, “Surface-induced ferroelectric ice on pt(111),” *Phys. Rev. Lett.*, vol. 80, no. 7, pp. 1533–1536, 1998.
- [220] S. M. Jackson, V. M. Nield, R. W. Whitworth, M. Oguro, and C. Wilson, “Single-crystal neutron diffraction studies of the structure of ice xi,” *The Journal of Physical Chemistry B*, vol. 101, no. 32, pp. 6142–6145, 1997.
- [221] G. Malenkov, “Liquid water and ices: understanding the structure and physical properties,” *Journal of Physics: Condensed Matter*, vol. 21, no. 28, p. 283101, 2009.
- [222] T. Kaneko, J. Bai, K. Yasuoka, A. Mitsutake, and X. C. Zeng, “Liquid-solid and solid-solid phase transition of monolayer water: High-density rhombic monolayer ice,” *The Journal of Chemical Physics*, vol. 140, no. 18, 2014.
- [223] P. Kumar, S. V. Buldyrev, F. W. Starr, N. Giovambattista, and H. E. Stanley, “Thermodynamics, structure, and dynamics of water confined between hydrophobic plates,” *Phys. Rev. E*, vol. 72, p. 051503, Nov 2005.

-
- [224] A. M. Saitta, F. Saija, and P. V. Giaquinta, “*Ab Initio* molecular dynamics study of dissociation of water under an electric field,” *Phys. Rev. Lett.*, vol. 108, p. 207801, May 2012.
- [225] I. Danielewicz-Ferchmin and A. Ferchmin, “Note of freezing of water nanolayers under electric fields,” *Acta Physicae Superficerum*, vol. VII, pp. 77–85, 2006.
- [226] M. Sobrino Fernández, F. M. Peeters, and M. Neek-Amal, “Electric-field-induced structural changes in water confined between two graphene layers,” *Phys. Rev. B*, vol. 94, p. 045436, Jul 2016.
- [227] V. F. Petrenko and R. W. Whitworth, *Physics of Ice*. Oxford University Press, 2002.
- [228] B. A. Bauer, G. L. Warren, and S. Patel, “Incorporating phase-dependent polarizability in nonadditive electrostatic models for molecular dynamics simulations of the aqueous liquid-vapor interface,” *Journal of Chemical Theory and Computation*, vol. 5, no. 2, pp. 359–373, 2009.
- [229] G. Sutmann, “Structure formation and dynamics of water in strong external electric fields,” *Journal of Electroanalytical Chemistry*, vol. 450, no. 2, pp. 289–302, 1998.
- [230] X. Hu, N. Elghobashi-Meinhardt, D. Gembris, and J. C. Smith, “Response of water to electric fields at temperatures below the glass transition: A molecular dynamics analysis,” *The Journal of Chemical Physics*, vol. 135, no. 13, 2011.
- [231] H. Qiu and W. Guo, “Electromelting of confined monolayer ice,” *Phys. Rev. Lett.*, vol. 110, p. 195701, May 2013.
- [232] G. Kresse and J. Furthmüller, “Efficient iterative schemes for *ab initio* total-energy calculations using a plane-wave basis set,” *Phys. Rev. B*, vol. 54, pp. 11169–11186, Oct 1996.
- [233] S. V. Zybin, W. A. Goddard, P. Xu, A. C. T. van Duin, and A. P. Thompson, “Physical mechanism of anisotropic sensitivity in pentaerythritol tetranitrate from compressive-shear reaction dynamics simulations,” *Applied Physics Letters*, vol. 96, no. 8, 2010.
- [234] D. Ehre, E. Lavert, M. Lahav, and I. Lubomirsky, “Water freezes differently on positively and negatively charged surfaces of pyroelectric materials,” *Science*, vol. 327, no. 5966, pp. 672–675, 2010.
- [235] I. M. Svishchev and P. G. Kusalik, “Electrofreezing of liquid water: A microscopic perspective,” *Journal of the American Chemical Society*, vol. 118, no. 3, pp. 649–654, 1996.

- [236] M. Neek-Amal, F. M. Peeters, I. V. Grigorieva, and A. K. Geim, “Commensurability effects in viscosity of nanoconfined water,” *ACS Nano*, vol. 10, no. 3, pp. 3685–3692, 2016.
- [237] E. Szemerédi and W. T. Trotter, “Extremal problems in discrete geometry,” *Combinatorica*, vol. 3, no. 3, pp. 381–392, 1983.
- [238] R. Gilmore, “Baker-campbell-hausdorff formulas,” *Journal of Mathematical Physics*, vol. 15, no. 12, pp. 2090–2092, 1974.
- [239] P. M. Lavrov, O. V. Radchenko, and I. V. Tyutin, “Jacobi-type identities in algebras and superalgebras,” *Theoretical and Mathematical Physics*, vol. 179, no. 2, pp. 550–558, 2014.
- [240] G. Strang, “On the construction and comparison of difference schemes,” *SIAM Journal on Numerical Analysis*, vol. 5, no. 3, pp. 506–517, 1968.
- [241] S. B. Reed M, *Functional Analysis. Methods of Modern Mathematical Physics Volume 1*, Academic Press, revised and enlarged ed., 1980.
- [242] B. C. Hall, *Lie groups, Lie algebras, and representations : an elementary introduction*. Graduate texts in mathematics 222, Springer, 2ed. ed., 2015.
- [243] C. R. J. Roger A. Horn, *Matrix Analysis*. Cambridge University Press, 1990.

Concluding remarks and outlook

In this thesis, we focused on questions concerning the effect of confinement on the ability of individual constituents to form large scale aggregates. In order to fulfil this objective, large scale molecular dynamics simulations were performed using the versatile simulator LAMMPS.

Our first topic of interest were colloidal systems consisting of Janus particles, characterized as particles with a different chemical composition on its hemispheres. In Chapter 3 a two-dimensional model of Janus disks consisting of a hydrophobic and charged semicircle was considered. When placed in a solution, the hydrophobic sides will be attracted towards one another while the charged sides give rise to a repulsive contribution to the interparticle potential. The electrostatic repulsion between colloids in solution took the form of a screened-Coulomb potential given by DLVO theory. This two-dimensional system of Janus disks was confined to a channel, in order to study the aggregation of these particles into membranes. For a solvent where the Debye-Hückel screening length was smaller than the particle size, the Janus nature of the colloids became profound and a wide range of different morphologies were found, varying in shape and orientational order. These distinctive features were used to label each state, and construct a phase diagram.

The two dimensional model of Janus disks was expanded to incorporate three-dimensional Janus spheres which were confined in a three-dimensional channel. The basic Janus pair-dynamics of shielding the hydrophobic patch from the liquid while maximizing the distance between charged hemispheres gave rise to a rich variety of clusters, which were identified according to the arrangement of the particles in a single base. We showed the formation of helices consisting of single, double,

triple, and quadruple chains. A striking property of these chains was that their helicity could be altered depending on the ionic concentration of the environment. Special attention was given to the formation of Boerdijk-Coxeter helices, which reinforces the importance of kinetic selection in the formation of large clusters. Inorganic NPs are undoubtedly a key component in future materials and biological agents. The relatively large control over their surface functionality is in contrast with their molecular counterparts. We showed that inorganic Janus particles can mimic peptide amphiphiles in regard to their ability to form membranes and helices with a tunable pitch, depending on the environment they are placed in. Further progress would require to enhance the surface capabilities of JPs toward programmable materials, in which nanoparticles encoded with specific and responsive interactions self-assemble into defined structures that can undergo large structural changes on-demand due to a simple trigger.

We also investigated, by means of computer simulation techniques, the effects of hydrophobic confinement on water. In order to mimic recent experimental work, two graphene layers were used in order to place water under extreme confinement where the interlayer distance between the graphene layers was a few Å. We observed that when water is placed in hydrophobic pores, the hydrogen-bond network is forced to terminate at these surfaces, causing the properties of water to be altered. In the presence of a later pressure of about 1 GPa flat layers of ice are recovered, for which the hydrogen-bond network lies parallel to the graphene sheets. In order to test if the found phase should be present inside hydrophobic nano-channels independent of their exact atomic nature, water was placed between hexagonal boron nitride layers. The same flat ice structure found, albeit at a different interlayer distance of the sheets. By increasing the distance between the graphene sheets, non-polar ice consisting of multiple flat layers was recovered. Bilayer ice was found with a square lattice structure in each plane, but where the interlayer configuration was between AA and AB stacked. Furthermore, we predicted that an odd (even) number of ice layers are stacks of monolayer (bilayer) ice.

Finally, we focused our attention on the effects of an external in-plane electric field on the rhombic-square monolayer of confined ice. We found that an in-plane electric field rotated the H-bonds and caused the monolayer ice to polarize without having lost the flatness of the network. During polarization, oxygen atoms moved slightly in-plane and formed a rhombic-rhombic lattice. Reversing the electric field did not restore the system to the non-polar state, instead a residual dipole moment remained in the system. The structural properties of water layers inside nanometre pores is important in the design of materials for filtration and separation techniques. Water confined in carbon nanotubes has been the subject of extensive studies as the molecularly smooth hydrophobic graphitic walls, and nanoscale diameter of a CNT gives rise to ultra-efficient water transport through these molecular pipes. In practical realisations however, they suffer from some major drawbacks.

Large grids of carefully placed CNTs must be made, in order to have a macroscopic water flow. The diameter of these CNTs must be small enough to hinder ions from entering the tube, and even for the smallest CNTs ions may partially enter the channels creating blockades that completely block the flow of water. Recent work has suggested that two-dimensional capillaries formed by closely spaced graphene layers can be completely impermeable to liquids, vapours, and gases (including helium), but allow for the unimpeded permeation of water. The formation of a flat water monolayer between these layers results in exceedingly fast diffusion that is 2-3 magnitudes faster than the self-diffusion of water molecules in liquid water. For this reasons, we believe that graphene could serve as an excellent candidate in the construction of compact, energy efficient water desalination devices.

Mario Sobrino Fernández

Curriculum vitae

Education

- 2012–2016 **PhD degree in Physics**, *University of Antwerp*.
 2010–2012 **Master degree in Physics**, *University of Antwerp*.
 2007–2010 **Bachelor degree in Physics**, *University of Antwerp*.

Master thesis

- title *Stochastic processes: solution methods based on a no-growth model and the determination of stopping times in radioactive decay*.
 supervisor Jacques Tempere

Publications

- Self-assembly of Janus particles confined in a channel, **M. Sobrino Fernández**, V. R. Misko, and F. M. Peeters, *Physical Review E*, 2014, 89, 022306.
- Self-assembly of Janus particles into helices with tunable pitch, **M. Sobrino Fernández**, V. R. Misko, and F. M. Peeters, *Physical Review E*, 2015, 92, 042309.
- AA-stacked bilayer square ice between graphene layers, **M. Sobrino Fernández**, M. Neek-Amal, and F. M. Peeters, *Physical Review B*, 2015, 92, 245428.
- Electric-field-induced structural changes in water confined between two graphene layers, **M. Sobrino Fernández**, F. M. Peeters, and M. Neek-Amal, *Physical Review B*, 2016, 94, 045436.
- Reversible structural transition in nanoconfined ice, V. Satarifard, M. Mousaei, **M. Sobrino Fernández**, J. Dix, J. Beheshtian, P. Carbone, F. M. Peeters, and M. Neek-Amal, under review.

Talks and Poster sessions

- 2013 Poster: *Soft Matter Meeting*, Self-assembly of Janus particles confined in a parabolic potential. Sapienza, Rome, Italy
- 2013 Poster: *I2CAM - FARPJ School*, Self-assembly of Janus particles confined in a parabolic potential. Centro Brasileiro de Pesquisas Físicas, Rio de Janeiro, Brasil
- 2015 Talk: *CMT seminars*, Numerical simulations of particle suspensions via a discretized Boltzmann equation. University of Antwerp.

Groenenborgerlaan 171 – B-2020 Antwerp – Belgium

☎ +32 32653539 • ☎ +32 32653542

✉ mario.sobrinofernandez@uantwerpen.be

Condensed Matter Theory Group

2016 Talk: *CMT seminars*, Square ice between graphene layers. University of Antwerp.

Academic experience

Tutor

2013-2014 Teaching assistant: Mathematical methods III.

2015-2016 Computer practicum: Maple, Matlab and \LaTeX .

Additional Courses

2014 Leadership & Teamwork, Antwerp Doctoral School, UAntwerp.

2015 Application Techniques, Antwerp Doctoral School, UAntwerp.

2013-2015 Language Courses Spanish, Language Center Linguapolis, UAntwerp.

Technical Skills

Scientific software LAMMPS, Matlab, Mathematica, \LaTeX .

Programming Languages Fortran, C++, Python.

